MEASUREMENT OF HEAT TRANSFER ENHANCEMENT AND PRESSURE DROP FOR TURBULENCE ENHANCING INSERTS IN LIQUID-TO-AIR MEMBRANE ENERGY EXCHANGERS (LAMEEs)

A Thesis Submitted to the College of

Graduate Studies and Research

In Partial Fulfillment of the Requirements

For the Degree of Master of Science

In the Department of Mechanical Engineering

University of Saskatchewan

Saskatoon

by

Ashkan Oghabi

© Copyright Ashkan Oghabi, April, 2014. All rights reserved.

PERMISSION TO USE

In presenting this thesis in partial fulfilment of the requirements for a Postgraduate degree from the University of Saskatchewan, I agree that the Libraries of this University may make it freely available for inspection. I further agree that permission for copying of this thesis in any manner, in whole or in part, for scholarly purposes may be granted by the professor or professors who supervised my thesis work or, in their absence, by the Head of the Department or the Dean of the College in which my thesis work was done. It is understood that any copying or publication or use of this thesis or parts thereof for financial gain shall not be allowed without my written permission. It is also understood that due recognition shall be given to me and to the University of Saskatchewan in any scholarly use which may be made of any material in my thesis.

A version of results in chapters 4, 5, and 7 is published in ASME Heat Transfer Conference and Applied Thermal Engineering. Results in chapters 4, 5 and 6 will be submitted for publication.

Requests for permission to copy or to make other use of material in this thesis in whole or part should be addressed to:

Head of the Department of Mechanical Engineering

University of Saskatchewan

Saskatoon, Saskatchewan, S7N 5A9

ABSTRACT

The fluid flow channels of modern heat exchangers are often equipped with different flow disturbance elements which enhance the convective heat transfer coefficient in each channel. These structural or surface roughness elements induce enhanced flow mixing and convective heat transfer at low Reynolds numbers ($500 < Re < 2200$) by fluid mixing near the channel walls and increasing the surface area. These elements, however, are accompanied by higher pressure drops in comparison to hollow smooth channels (without inserts).

The Run-Around Membrane Energy Exchanger (RAMEE) system is an air-to-air energy recovery system comprised of two remote liquid-to-air membrane energy exchangers (LAMEEs) coupled by a pumped liquid desiccant loop. LAMEEs use semi-permeable membranes that are permeable to water vapor, but impermeable to liquid water. The membranes separate the liquid desiccant from the air flow channels, while still allowing both heat and water vapor transfer. The air channels are equipped with turbulence enhancing inserts which serve dual purposes: (a) to support the adjacent flexible membranes, and (b) to enhance the convective heat and mass transfer.

This research experimentally investigates the increase in the air pressure drop and average convective heat transfer coefficient after an air-side insert is installed in a Small-scale wind tunnel for exchanger insert testing (WEIT) facility that is designed to simulate the air channels of a LAMEE and to measure all the properties required to determine the flow friction factor and Nusselt number. Experiments are conducted in the test section under steady state conditions at Reynolds numbers between 900 and 2200 for a channel with and without inserts. The 500-mm-long test section has a rectangular cross section (5 mm wide and 152.4 mm high) and is designed to maintain a specified constant heat flux on each side wall. The flow is laminar

and hydrodynamically fully developed at the entrance of the test section and, within the test section, thermal development occurs.

Nine different insert panels are tested. Each insert is comprised of several plastic rib spacers, each aligned parallel to the stream-wise direction, and several cross-bars aligned normal to the flow direction. The plastic rib spacers are placed either 30 mm, 20 mm or 10 mm apart, and the distance between the cylindrical bars is either 30 mm, 45 mm, 60 mm or 90 mm. The measured convective heat transfer coefficient and the friction factor have uncertainties that are less than ±7% and ±11%, respectively.

It is found that the Nusselt number and friction factor are dependent on the insert geometry and the Reynolds number. An empirical correlation is developed for the inserts to predict Nusselt number and friction factor within an air channel of a LAMEE. The correlations are able to determine the Nusselt number and the friction factor within ±9% and ±20% of the experimental data. Results show the flow insert bar spacing is the most important factor in determining the convective heat transfer improvement.

As an application of the experimental data in this thesis, the experimental and the numerical results from a LAMEE which has an insert in each airflow channel are presented. The results show that the insert within the air channel of the LAMEE is able to improve the total effectiveness of the LAMEE by 4% to 15% depending on the insert geometry and air flow Reynolds number and operating inlet conditions for the exchanger.

ACKNOWLEDGEMENTS

Foremost, I would like to acknowledge my supervisors, Profs. C.J. Simonson and R.W. Besant for their guidance and inspiration throughout the entire research process.

Special thanks to my committee members, Prof. David Sumner and Prof. Donald J. Bergstrom, for their recommendations and suggestions.

Most importantly, I would like to express my deepest appreciation to my parents, brother, and aunt, for their love and support.

I would like to thank to my friends Houman Kamali, Davood G. Moghaddam, Reza Aminzadeh, Ahad Armin, Nazanin Samadi for their supports and encouragements.

I also would like to acknowledge financial support from the Natural Science and Engineering Research Council of Canada (NSERC) and Venmar CES Inc; Saskatoon.

DEDICATION

I dedicate this work to my beloved parents for their gracious support.

TABLE OF CONTENTS

PERMISSION TO USE i

ABSTRACT ii

ACKNOWLEDGEMENTS iv

DEDICATION v

TABLE OF CONTENTS vi

LIST OF TABLES ix

LIST OF FIGURES x

NOMENCLATURE xiii

1. INTRODUCTION 1
   1.1. Introduction 1
   1.2. Heat transfer enhancement 1
      1.2.1. Practical problem 3
      1.2.2. Literature review 4
   1.3. Motivation and research objectives 9
   1.4. Thesis overview 12

2. EXPERIMENTAL FACILITY AND INSTRUMENTATION 13
   2.1. Introduction 13
   2.2. Turbulence enhancing inserts 13
   2.3. Apparatus and procedure 16
      2.3.1. Airflow network 17
      2.3.2. Test section 18
      2.3.3. Data acquisition 22
   2.4. Measurements and instruments calibration 23
      2.4.1. Temperature sensors 23
      2.4.2. Pressure transducer 24
      2.4.3. Orifice plate 26

2.5. Commissioning of WEIT facility 27
2.5.1. Mass balance procedure 27
2.5.2. Fully developed flow at entrance to the test section 29
3. DATA ANALYSIS METHOD 34
3.1. Introduction 34
3.1. Entrance effects 34
3.2. Dimensionless variables and properties 35
3.2.1. Reynolds number (Re) 35
3.2.2. Friction factor (f_D) 36
3.2.3. Nusselt number (Nu) 37
3.3. The bias and precision uncertainty of calculated parameters 40
3.3.1. Reynolds number 40
3.3.2. Friction factor 41
3.3.3. Nusselt number 41
3.4. Mass and energy balances 42
3.5. Experimental data comparison between channel with inserts and hollow channels 44
3.5.1. Pumping power (P_{pump}) 44
3.5.2. Correlation for hollow channel 45
4. VALIDATION OF EXPERIMENTAL DATA 48
4.1. Introduction 48
4.2. Experimental validation 48
4.2.1. Hollow channel 49
4.2.2. Channel with inserts 51
4.3. Effect of heat flux on Nu 53
4.4. Repeatability 54
5. MEASURED NUSSELT NUMBERS AND FRICTION FACTORS 57
5.1. Introduction 57
5.2. Nusselt number (Nu) and Darcy friction factor (f_D) 57
5.3. Enhancement in heat transfer 64
6. EMPIRICAL CORRELATIONS 71
6.1. Introduction 71
6.2. Nusselt number correlation 72

6.3. Darcy friction factor correlation 78

7. APLICATION OF TURBULENCE ENHANCING INSERTS IN A LAMEE 87

7.1. Introduction 87

7.2. LAMEE properties 87

7.3. Single-panel energy exchanger test (SPEET) facility 89

7.4. Performance evaluation of a LAMEE 90

7.4.1. Effectiveness 90

7.4.2. *NTU* and Cr^* 91

7.5. Numerical model 92

7.6. Comparison of the numerical and experimental the single-panel LAMEE effectiveness 94

8. CONCLUSIONS AND FUTURE WORK 97

8.1. Summary and conclusions 97

8.2. Contribution 99

8.3. Future work 100

REFERENCES 101

APPENDIX A 104

EXPERIMENTAL DATA 104

A.1. Energy balance 104

A.2. Nusselt number and friction factor for inserts 106

A.3. Comparison of *Nu* for channels with the inserts and the hollow channel where both have a same pumping power 108

A.4. Comparison between the predicted and the experimental value of *Nu* 110

A.5. Comparison between the predicted and the experimental value of f_D 112

APPENDIX B 114

PARAMETER ESTIMATION CODE 114

B.1. Friction factor correlation 114

B.2. Nusselt number correlation 117

LIST OF TABLES

Table 2-1 Spacing between the cylindrical cross-bars (B) and the plastic ribs (R) of the turbulence enhancing inserts. **15**

Table 3-1 Thermal entry length for the experiments conducted in the hollow channel **35**

Table 4-1 Experimental data for the hollow channel **49**
Table 4-2 *Nu* for B30R20 with three different heat fluxes on the side walls **53**
Table 4-3 Repeatability of the experimental data of B60R20 ..... **55**

Table 6-1 Coefficients in empirical correlation $Nu = a_1 * \mathrm{Re} + b_1$ for constant cylindrical bars intervals **72**

Table 6-2 Determination of coefficient of $Nu = A(\frac{W}{\mathrm{H}})^B \mathrm{Re} + C$ **74**

Table 6-3 Coefficient of $f_D = a_2 \exp(\frac{b_2}{\mathrm{Re}})$ for different cylindrical bars intervals **79**

Table 6-4 Coefficient of b_2 based on the average a_2 in correlation of $f_D = a_2 \exp(\frac{b_2}{\mathrm{Re}})$ **80**

Table 6-5 Determination of coefficient of $f_D = A_1 exp(\frac{B_1 \frac{W}{\mathrm{H}} + C_1}{\mathrm{Re}})$ **81**

Table 7-1 The small-scale single-panel LAMEE specification [31] **88**
Table 7-2 Measured air and solution inlet and outlet conditions for the small-scale LAMEE at *NTU* = 3 and different *Cr** with LiCl salt solution under different operating conditions [31] **92**

Table A-1 Energy balance results for heat transfer tests **104**
Table A-2 Experimental data for inserts **106**
Table A-3 Equivalent Reynolds number and Nusselt number within the hollow channel **108**
Table A-4 Comparison between the empirical and the experimental average Nusselt number for inserts **110**
Table A-5 Comparison between the empirical and the experimental f_D for inserts **112**

LIST OF FIGURES

Figure 1-1 References on heat transfer augmentation vs. year of publication [4] **2**
Figure 1-2 Symmetric plan of the channel with vortex generators and geometrical parameters (l = 1.2H, h = 0.6H, s = 3.75H, B = 4H) [11] **6**
Figure 1-3 Isometric view of the test section without the upper wall [14] **7**
Figure 1-4 Schematic of the turbulence enhancing insert in a LAMEE **10**
Figure 1-5 Approximation effect of cylindrical bars on the flow [19] **11**

Figure 2-1 (a) Isometric and (b) front view of an insert **14**
Figure 2-2 Top view and dimension of the plastic ribs (Dimensions in mm)..... **15**
Figure 2-3 (a) Experimental facility (b) Schematic diagram of WEIT facility (Top view) **17**
Figure 2-4 Detailed view of the test section and the extension channel **18**
Figure 2-5 Side wall of the test section with pressure tubes **19**
Figure 2-6 Isometric (a) and side (b) views of the rectangular test section showing the coordinate system, dimensions, insulation and location of the thermocouple near the heater element. **20**
Figure 2-7 Front view of the side wall showing the locaton of the thermocouple between the side walls and the insulation **21**
Figure 2-8 Thermocouple location for wall temperature measurements along the test plate (all dimensions are in mm). **22**
Figure 2-9 LabView graphical user interface..... **23**
Figure 2-10 Calibration curve for (a) DP15-20 (orifice plate transducer), (b) DP103 (test section pressure transducer) **25**
Figure 2-11 Calibration data for 12.5 mm orifice plate **26**
Figure 2-12 Total pressure probe with diameter of 0.3 mm **28**
Figure 2-13 Velmex bislide positiong system..... **29**
Figure 2-14 Laminar velocity profile at X=-10 mm. The 95% uncertainties in velocity measurements are shown with error bars. **30**
Figure 2-15 Static pressure drop along the developing channel and the test section without inserts (X/L= 0 corresponds to the inlet of the test section) **32**

Figure 3-1 Conduction loss from the test section measured at the center line of the test section at Re = 918 (Q_{air}/A = 346 W/m^2)..... **39**
Figure 3-2 Energy balance of the test section for the hollow channel (without an turbulence enhancing insert) at different Reynolds numbers **44**

Figure 4-1 Comparison between the experimental and the theoretical value of the friction factor times Re for the hollow channel. The error bars represent the 95% uncertainty bounds for the experimental data. **50**

Figure 4-2 Comparison between the experimental and the theoretical *Nu* for the hollow channel. The error bars represent the 95% uncertainty bounds for the experimental data.....**51**
Figure 4-3 Top view of the test section available in the literature [6]. **52**
Figure 4-4 Comparison of *Nu* measured in the WEIT facility with *Nu* measured by Vujisic [6]. The tests are for the case of constant heat flux on one wall only.....**53**
Figure 4-5 *Nu* for B30R20 at Re = 2150 with three different heat fluxes on side walls **54**
Figure 4-6 Repeatability of the Measured *Nu* for B60R20 .....**56**

Figure 5-1 (a) The experiemntal Nusselt number and (b) Darcy Friction factor for B30R20 and B30R30.....**58**
Figure 5-2 (a) The experimental Nusselt number and (b) Darcy Friction factor for B45R20 and B45R30 .....**60**
Figure 5-3 (a) The experimental Nusselt number and (b) Darcy Friction factor for B60R20 and B60R30 .....**61**
Figure 5-4 (a) The experimental Nusselt number and (b) Darcy Friction factor for B90R10, B90R20, and B90R30.....**62**
Figure 5-5 Effect of the Cylindrical bars spacing on (a) Nusselt number and (b) Darcy friction factor **64**
Figure 5-6 Comparison between the channel with inserts and the hollow channel (a) Nu_{Re}^{*}, (b) f^{*}. **66**
Figure 5-7 Heat transfer enhancement for (a) B30R20 and B30R30, (b) B45R20 and B45R30, (c) B60R20 and B60R30, and (d) B90R10, B90R20, and B90R30.....**70**

Figure 6-1 Relation of coefficient a_1 and b_1 with *W*/H. **73**
Figure 6-3 Difference between the empirical and experimental Nusselt number (data from Appendix A.4). **78**
Figure 6-4 Relation between coefficient b_2 and (*W*/H). **81**
Figure 6-5 Comparison between empirical and experimental f_D for (a) B30R20 and B30R30, (b) B45R20 and B45R30, (c) B60R20 and B60R30, and (d) B90R10, B90R20, and B90R30 (using data in Table 6-5). **84**
Figure 6-6 Difference between empirical and experimental f_D (data from Appendix A.5)……..**85**

Figure 7-1 The small-scale single-panel LAMEE a) air and solution configuration, and b) cross section view [31].....**88**
Figure 7-2 Schematic view of the SPEET facility and measurement instruments [31].....**90**
Figure 7-3 Effect of the enhanced Nusselt number on the effectiveness of the single-panel LAMEE at *NTU*=3 and Cr^{*}=5 and the inlet condition is the same as Table 7-2 [31] **93**
Figure 7-4 Comparison of the numerical and experimental steady state effectiveness of the single-panel LAMEE at different Cr^{*} and *NTU* of 3.8 [31]. **96**

NOMENCLATURE

ACRONYMS

NTU	Number of heat transfer units
SPEET	Single-panel energy exchanger test
WEIT	Small-scale wind tunnel for exchanger insert testing

ENGLISH SYMBOLS

A	Cross section area of the channel [m^2]
A	Surface area of the side walls [m^2]
A_c	Wetted area [m^2]
B	Bias uncertainty of parameter
Cr^*	heat capacity ratio
$C_{p,air}$	Specific heat capacity of the air at constant pressure [J/kg·K]
D	Diameter of cylindrical bars [mm]
D_h	Hydraulic diameter [m]
D_{va}	Diffusivity coefficient of vapor into air [m^2/s]
f^*	Friction factor ratio of channel with inserts and hollow channel at same Re
f_D	Darcy friction factor
H	Spacing between cylindrical bars [mm]
H^*	Operating factor
h	Convective heat transfer coefficient [W/m^2·K]
h_{ave}	Average convective heat transfer coefficient [W/m^2·K]
h_{fg}	Enthalpy of phase change [J/kg]
h_m	Convective mass transfer coefficient [kg/m^2·s]
I	Current supplied to the heater [A]
K	Thermal conductivity [W/m·K]
L	Length of test section [mm]
Le	Ratio of the thermal and mass diffusivities
$\dot{m}$	Mass flow rate of air [g/s]
Nu	Global Nusselt number

$\overline{Nu}_{\text{eq,hollow}}$	Average Nusselt number for the developing flow in a hollow channel
Nu_P^*	Ratio of *Nu* for channel with inserts and the hollow channel at same pumping power
Nu_{Re}^*	Ratio of *Nu* for channel with inserts and the hollow channel at same Re
P	Pressure [Pa]
P	Perimeter [m]
P	precision uncertainty of parameter
ΔP	Differential pressure [Pa]
P_{pump}	Pumping power [W]
Pr	Prandtl number
dP/dx	Pressure gradient along the test section [Pa/m]
Q	Heat transfer rate [W]
Q_{air}	heat transfer rate from the heaters to the air calculated based on equation (3-10) [W] or [W/m^2] when normalized by area (Q_{air}/A)
Q_{heater}	Corrected heat transfer rate from the heaters to the air (corrected for the heat loss to the surroundings) according to equation (3-15) [W]
Q''_{loss}	Conduction heat flux from the test section to the surroundings calculated from equation (3-11) [W/m^2]
Re	Reynolds number
Sh	Sherwood number
T	Temperature [°C or K]
ΔT_{lm}	Log mean temperature difference [K]
t	insulation thickness [mm]
t	student's t value at a 95% confidence level
U	Overall heat transfer coefficient [W/m^2·K]
U_{T}	Total uncertainty
V	Spacing between plastic ribs [mm]
V	Voltage [V]
V_{ave}	Average velocity of the air [m/s]
V_x	Local velocity of air along the channel [m/s]

W	Width of the channel or plastic ribs width [mm]
W	Humidity ratio
X	Cartesian coordinate direction [mm]
$x_{\mathrm{fd,t}}$	Thermal fully developed length [mm]
Y	Cartesian coordinate direction [mm]
Z	Cartesian coordinate direction [mm]

GREEK SYMBOLS

δ	Membrane thickness [m]
ε	Effectiveness
μ_{f}	Viscosity of the dry air [N·S/m^2]
ρ	Density of air [kg/m^3]
σ	Variance of a parameter

SUBSCRIPTS

air	Property of air
exp	Experimental
in	Inlet of the test section
insul	Insulation
lam	laminar
lat	Latent
out	Outlet of the test section
P	Pumping power
Re	Reynolds number
sen	Sensible
solution	Property of solution
static	Static
Surf	Wall surface
tot	Total
turb	Turbulent

CHAPTER 1
INTRODUCTION

1.1. Introduction

Research in this thesis focuses on air-channel convective heat transfer enhancement for membrane energy exchangers. In this work, the heat transfer coefficient is determined using the measured data obtained from a test section of a small-scale wind tunnel for exchangers insert testing (WEIT). The heat transfer coefficient is measured within a rectangular channel in the WEIT facility during steady-state test conditions with constant air flow and heat flux on the side walls of the channel. The results show that the channel insert panels increase the convective heat transfer coefficient and consequently the effectiveness performance of the membrane exchangers. Based on the measured data, an empirical correlation is developed to predict the convective heat transfer coefficient and the friction factor for the rectangular air channels with the inserts installed.

1.2. Heat transfer enhancement

Heat and mass transfer play a crucial role in the performance of many engineering systems such as heat exchangers for air heating, cooling and refrigeration, temperature suppression schemes for engines, motors, and electronic devices, chemical reactor cooling and heating systems, energy exchangers that transfer both heat and water vapor, etc. [1], [2]. Over

several decades, there has been an increasing number of research papers published on heat transfer enhancement (see Figure 1-1) [3].

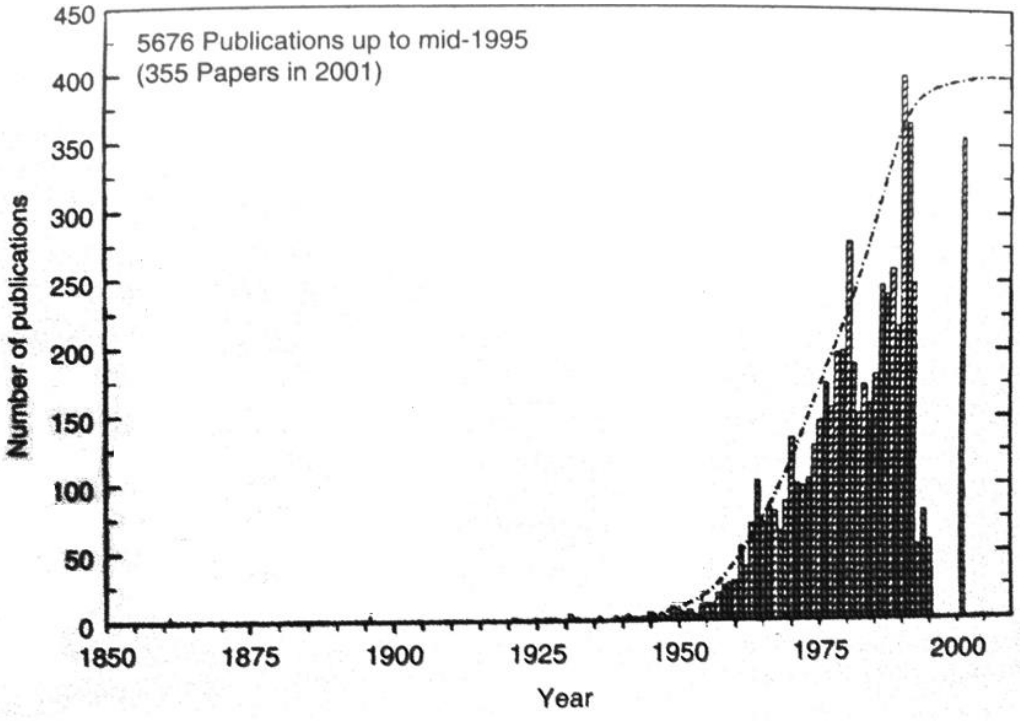

Figure 1-1 References on heat transfer augmentation vs. year of publication [4].

The main objective of heat (mass) transfer enhancement methods is, for a selected flow rate, to decrease the fluid heat (mass) transfer flux resistance when the flow channel Reynolds number (Re) is low and the flow is laminar. Heat transfer enhancement techniques can be divided into two groups: active and passive. Active techniques use an external energy source such as electrical, mechanical power (e.g. vibrations), magnetic field, etc. to enhance the heat flux. Passive techniques use fluid additives (e.g. nanoparticles or bubbles) or special geometric surface modifications and separate inserts or panels for heat flux augmentation. Each of these passive methods requires additional fan or pump power inputs and each implies that additional interface areas are used. These additional surface areas are not included in the calculation of heat exchanger area. The passive techniques are often more attractive for industry because the

passive techniques are less expensive and more reliable compared to the active ones [3]. Heat flux enhancement means that the same heat rate performance can be achieved using a smaller heat transfer surface area [5].

Many heat transfer enhancement techniques use fins with high thermal conductivity to increase the heat transfer coefficient or heat transfer area. Fins enhance the heat flux by including hydrodynamic instabilities and flow mixing near the heat flux surfaces [6].

1.2.1. Practical problem

Membrane energy exchangers are a new category of exchangers that transfer both heat and moisture between two fluids. The fluids are separated by a semi-permeable membrane which separates the fluids but allows water vapor transfer between the two fluids.

The heating, ventilation, and air conditioning (HVAC) research group at University of Saskatchewan has performed research on membrane energy exchangers since 2002. One specific membrane energy exchanger is called the RAMEE (Run-Around Membrane Energy Exchanger) which is an air-to-air energy recovery system comprised of two remote liquid-to-air membrane energy exchangers (LAMEEs) coupled by a liquid desiccant loop. LAMEEs use semi-permeable membranes that are permeable to water vapor, but impermeable to liquid water. The membranes separate the liquid desiccant from the air, while still allowing both heat and water vapor flux [7].

The HVAC research group at the University of Saskatchewan has numerically and experimentally studied the performance of RAMEEs and LAMEEs. They have studied the flow configuration and the steady-state and the transient performance of exchangers and systems. They employed air screens in the air channels of their exchangers to provide the

support for the elastic semi-porous membrane. More recently, they have tested the exchanger performance with inserts in the air channels [7].

The overall heat transfer coefficient in a LAMEE depends on the air convective heat transfer coefficient, the thermal conductivity of the membrane, and the solution convective heat transfer coefficient,

$$U = [\frac{1}{h_{\text{air}}} + \frac{\delta}{K_{\text{mem}}} + \frac{1}{h_{\text{solution}}}]^{-1}, \quad (1\text{-}1)$$

where h_{air} is the air convective heat transfer coefficient [W/m^2·K], h_{solution} is the solution convective heat transfer coefficient, K_{mem} is the thermal conductivity of the membrane [W/m·K], and δ is the membrane thickness [m].

The air convective heat transfer coefficient is the order of 20 W/m^2·K, $\frac{K_{\text{mem}}}{\delta}$ is the order of 250 W/m^2·K, and the solution convective heat transfer coefficient is the order of 1000 W/m^2·K. Therefore, the air convective heat transfer coefficient has a dominant effect on the overall heat transfer coefficient [8], [9]. Therefore, the HVAC research group recently considered enhancing the air convective heat transfer coefficient to increase the overall heat transfer coefficient. The following section reviews some of the relevant studies on heat transfer enhancement methods for channels with a similar geometry to the air channels of a LAMEE. The next section explains the physics of the problem and the potential for the heat flux enhancement inside the air channels of the LAMEE.

1.2.2. Literature review

Past studies of the heat transfer enhancement show extensive research, but only a few papers presented data on the heat transfer enhancement for the flow between parallel plates for

Re smaller than 2200. This section reviews the experimental and the numerical studies on the heat transfer enhancement within rectangular channels at low Reynolds numbers.

The passive methods of heat transfer enhancement for internal flows can be divided into three groups: inserts, internal fins, and internal roughness. The studies that are reviewed here are mainly focused on inserts with various geometries and internal fins. The inserts are effective if used in the laminar flow and can enhance the heat flux in hollow channels [3].

Olsson and Sundén [10] investigated the heat transfer enhancement within a rib roughened rectangular channel with an aspect ratio of 1:8. They conducted their experiments for five different rib geometries (cross ribs, parallel ribs, cross V ribs, parallel V-ribs and multiple V-ribs) at Reynolds numbers (Re) between 500 and 15000. The flow visualization conducted by Olsson and Sundén at Re = 1100 showed that the secondary flow strongly affects the velocity distribution and flow disturbances. They showed that the cross ribs and parallel ribs increased the heat transfer more and increased the pressure drop less than the cross V ribs, the parallel V ribs, and the multiple V-ribs within the channels for Re less than 2000 [10].

Zhu et al. [11] numerically investigated the heat transfer enhancement within a rectangular channel. The bottom wall of the channel was roughened with ribs and insulated and the other wall had a vortex generator (Figure 1-2) with constant temperature. They studied the effect of the angle of vortex generators and period length (*L/H*, Figure 1-2) of vortex generators on heat transfer enhancement for Re between 3×10^5 and 1.5×10^5. They used vortex generators with a period length (*L/H*, Figure 1-2) of 2.5, 3.75, and 5. The results showed that the rib roughened wall and the vortex generator with the period length (*L/H*,) of 3.75 and the angle of 45° (β, Figure 1-2) enhanced the convective heat transfer coefficient by a factor of four. On the other hand, the pressure drop was 44 times higher than the hollow channel [11].

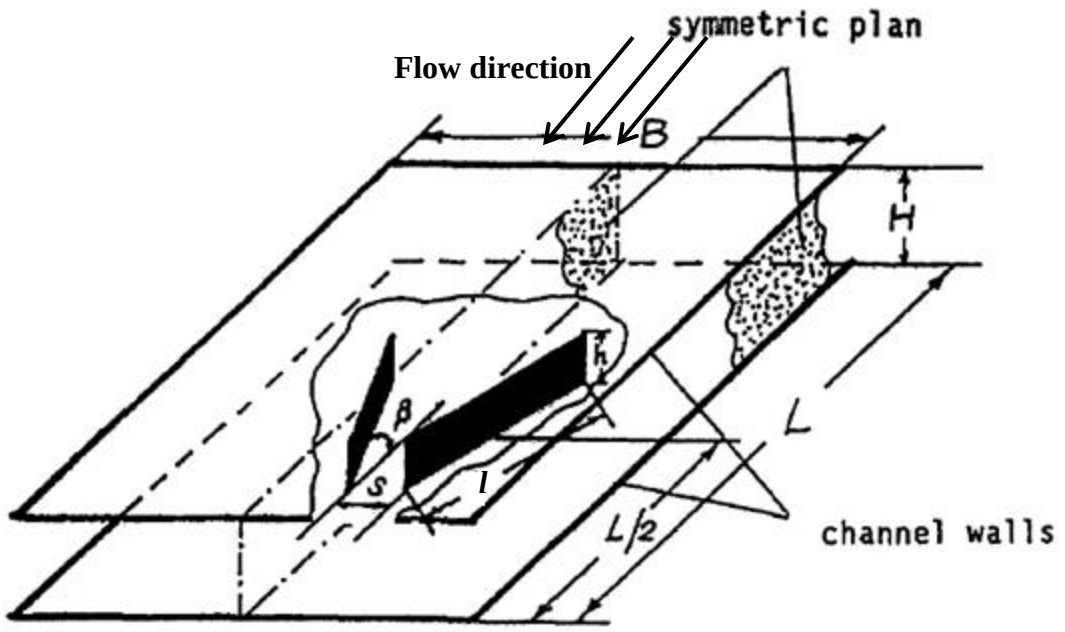

Figure 1-2 Symmetric plan of the channel with vortex generators and geometrical parameters (l = 1.2H, h = 0.6H, s = 3.75H, B = 4H) [11].

Russell et al. [12] investigated the effect of using longitudinal vortices on enhancing heat flux in flat heat exchangers. They used delta and rectangular winglets vortex generators inside the channels. They showed that the rectangular winglet in two staggered rows with a 20° angle of attack was the most effective on heat transfer enhancement of the flat exchangers. The rectangular winglets increased the heat transfer by 47% and increased the pressure drop by 30% at Re = 500. They concluded the application of winglets is more effective in the flat exchangers for Re between 1500 and 2200. They only did experiments on the full-scale flat heat exchangers without winglets. A limitation of their work was using the available correlations in the literature for predicting the convective heat transfer coefficient and the pressure drop, which typically have a 10-30% deviation from the actual value [12], [13].

Sparrow and Tao [14] experimentally measured the heat flux in a flat rectangular channel which had periodic cylindrical rods along one principal wall (isometric view of the channel with rods is shown in Figure 1-3). They conducted experiments within the channel with two different thermal boundary conditions for five values of Re between 10,000 and 45,000. In the first thermal boundary condition, one wall was isothermal and the other wall was adiabatic. In the second thermal boundary condition, both walls of the channel were isothermal. The rodded wall of the channel was made of naphthalene and they measured the mass transfer coefficient. They determined the local heat transfer coefficient with the analogy between the mass and heat transfer. They studied different channel aspect ratios and distances between the rods. The distance between rods affected the heat transfer on the smooth wall and the pressure drop within the channel. They showed that the heat transfer and pressure drop increased as the aspect ratio of the channel decreased and the distance between the rods decreased. The average heat transfer was enhanced by 90% by the rods at one principal wall. Also, they developed a power law correlation for the mass transfer and friction factor and the correlation matched very well with their experimental measurements [14].

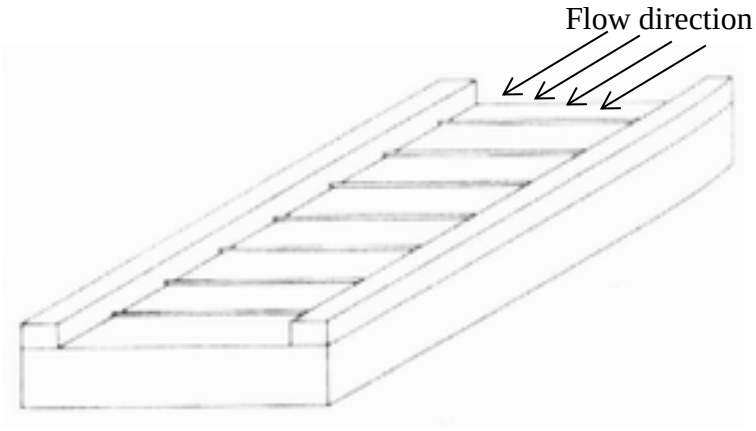

Figure 1-3 Isometric view of the test section without the upper wall [14].

Han et al. [15] experimentally tested the effect of the rib geometry on the heat flux enhancement for the flow between two parallel plates. They used ribs with different shapes, angles of attack and pitch-to-height ratios. They conducted the experiments for the channel with constant heat flux on the side walls and the channel width varied between 2.5 cm and 1.3 cm. They proposed the convective heat transfer coefficient and friction factor correlations in terms of the rib geometry and Re. The correlations proposed by Han et al. had 20% to 40% discrepancy with the available correlations for similar flow and channel configurations. The results showed that the symmetric arrangement of the ribs with the angle of attack of 45° and the pitch-to-height ratio of ten provided the best enhancement in heat transfer compared to the other rib geometries that they tested. Han et al. showed that the ribs enhanced the heat transfer by a factor of three compared to the hollow channel with the same friction factor [15].

Zhang and Balachandar [16] numerically simulated the flow inside parallel plate fin heat exchangers. Their study was focused on the flow for inline and staggered fin arrangements at Re of 246, 720, 1245, and 1465. They found that the flow transition from the laminar regime to the turbulent regime occurred between the Re of 246 and 720. They showed that the fins increase the heat transfer and pressure drop by disturbing the boundary layer and providing the larger velocity and temperature gradients near the wall. The flow simulation showed that increasing the Re generates vortices at the fin surfaces, causes flow mixing and heat flux enhancement. On the other hand, the form drag increases due to the wake behind the fins which causes the friction factor to increase inside the channel [16].

Hamdan and Al-Nimr [17] numerically investigated the effect of porous fins on the heat flux enhancement within an isothermal parallel plate channel at a Re of 20, 60 and 100. They studied the effect of the porous material properties on the heat flux enhancement. They

showed that increasing the fin thickness, the permeability, the pore size, and the thermal conductivity of the porous fins increased the heat transfer within the channel by making the hydrodynamic and thermal boundary layers thinner on the fin surfaces and providing better mixing in the flow [17].

Vujisic [6] investigated the effect of eddy-promoter bars on the heat transfer enhancement within a parallel plate channel. He conducted the experiments for the channel with one heated wall for a Re between 555 and 5145. He spaced the cylindrical bars periodically at the center of the channel and at equal distances in the flow direction. The Nusselt numbers were measured to be 11 and 12 at Re of 656 and 820, respectively, which is significantly greater than $Nu = 5.8$ (for laminar flow in a hollow channel with a constant heat flux on one wall and the other wall insulated). Also, he developed an analogy between the heat and momentum for the tested eddy promoters which can predict the Nusselt number for the periodically spaced cylindrical bars with 10 to 14% accuracy compared to the experimental data [6].

LePoudre et al. [18] numerically investigated the effect of a corrugated porous screen on the heat transfer enhancement in flat plate heat exchangers. They studied heat transfer inside a parallel-plate channel with constant heat flux on both walls for Re between 1370 and 2750. Their study reported 90% heat transfer enhancement in the channel with the corrugated screen compared to the hollow channel. However, the pressure drop was increased by factor of four compared to the hollow channel [18].

1.3. Motivation and research objectives

The review of the publications in the area of the heat transfer enhancement in Section 1.2 showed the effect of the fins and inserts on the heat transfer inside rectangular channels.

To enhance the convective heat transfer within the air channels of a LAMEE the HVAC research group at the University of Saskatchewan has employed turbulence enhancing inserts to serve dual purposes: (a) enhance the heat and mass transfer and (b) support the flexible membranes.

Figure 1-4 shows the schematic of the inserts used within the air channels of a LAMEE. The inserts were constructed by vertical cylindrical bars with a diameter of 1.6 mm and horizontal ribs. The horizontal ribs hold the cylindrical bars and support the flexible membrane. The bars were spaced evenly at the centers of the air channels of the LAMEE.

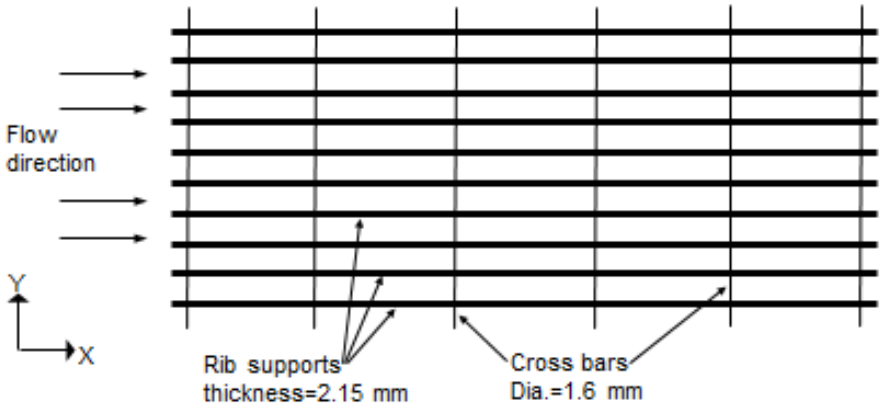

Figure 1-4 Schematic of the turbulence enhancing insert in a LAMEE.

The bars provide better mixing in the main flow (Figure 1-5) and increase the temperature gradient at the wall surface of the channels. The inserts disturb the hydrodynamic and thermal boundary layers and reduce the thermal resistance at the wall surface of the channels. Therefore, it is expected the turbulence enhancing inserts enhance the heat and mass transfer within the air channels of the LAMEE.

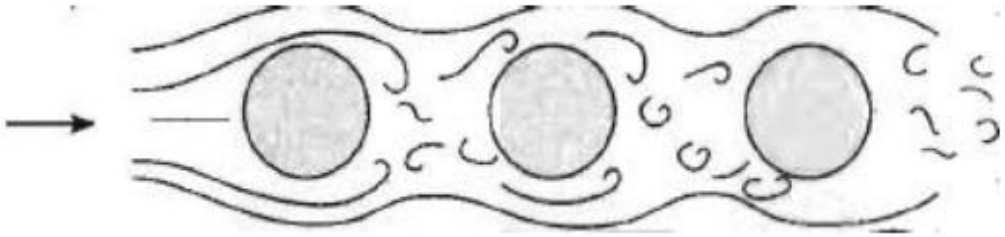

Figure 1-5 Schematic of the effect of cylindrical bars on the flow [19].

Review of the similar work on heat transfer enhancement shows that the heat transfer enhancement for membrane flat-plate exchangers especially for a LAMEE is missing in the literature.

The HVAC group at the University of Saskatchewan has the practical problem of using inserts within the air channels of LAMEEs and there are no available data in the literature; therefore, the current research focuses on experimentally measuring the heat transfer and pressure drop within the air channels with turbulence enhancing inserts. For this purpose the small-scale wind tunnel for exchangers insert testing (WEIT) is used to test the turbulence enhancing inserts. The objectives for this thesis and the chapter of the thesis that addresses the objectives are listed below:

1. Investigate the effect of the inserts on the heat transfer within the WEIT facility (Ch. 5)
2. Develop a correlation to predict the enhanced convective heat transfer coefficient produced by the inserts within the air channel of a LAMEE (Ch. 6)
3. Develop a correlation to predict the friction factor for the inserts within the air channel of a LAMEE (Ch. 6)
4. Investigate the effect of the heat transfer enhancement by the inserts on the performance of a LAMEE (Ch. 7)

1.4. Thesis overview

The experimental facility and sensors calibration are described in Chapter 2. Also, the mass and energy balance confirmation is presented in Chapter 2. Chapter 3 provides dimensionless parameters used in this thesis and the calculation methods used to determine the convective heat transfer coefficient (*Nu*) and friction factor (f_D) from the measured data. The convective heat transfer coefficient for the hollow channel (without inserts) is validated in Chapter 4. Also, the repeatability of the experimental data and verification of *Nu* for different heat fluxes from the test plates are investigated in Chapter 4. The experimental data for the heat transfer and pressure drop for all the tested inserts are presented in Chapter 5. Chapter 6 uses the data in Chapter 5 to develop an empirical correlation to allow the prediction of *Nu* and f_D as a function of Re and dimensionless geometry ratios. An application of the tested inserts is presented in Chapter 7, which contains the experimental and numerical results for a LAMEE with a turbulence enhancing insert. Summary, conclusions, and future work are presented in Chapter 8.

CHAPTER 2
EXPERIMENTAL FACILITY AND INSTRUMENTATION

2.1. Introduction

This Chapter describes the test facility that is used to measure the pressure drop and to determine the convective heat transfer coefficient across a test section containing a turbulence enhancing insert. The test facility is a small-scale wind tunnel for exchanger inserts testing (WEIT) with a rectangular test section.

This chapter explains the WEIT facility, the experimental procedure, the sensors and their calibration. Section 2.2 describes the turbulence enhancing inserts; and section 2.3 describes the experimental facility used to test the inserts. Section 2.4 describes the instrumentation and sensor calibration. In Section 2.5, preliminary test data are presented which confirms that, for the flow rates tested, the wind tunnel provides fully developed flow at the entrance of the test section.

2.2. Turbulence enhancing inserts

The turbulence enhancing inserts tested are designed to enhance the heat and mass flux on the input surfaces of air channels of a LAMEE. The design of the inserts tested in this thesis is shown in Figure 2-1. Each insert is comprised of several equally spaced horizontal ribs each aligned in the stream-flow direction and several vertical cylindrical cross-bars centered on the flow channel centerline and each aligned normal to the flow direction. The only variation in

design between the different inserts is in the spacing of the ribs (dimension V in Figure 2-1) and the cross-bars (dimension H in Figure 2-1). The dimensions of the horizontal plastic ribs are shown in Figure 2-2. The ribs are rapid prototyped in the Engineering Shops using FULLCURE 850 composite material. The ribs are 5 mm wide and 490 mm long. The cylindrical cross-bars are made of steel with a length of 152.4 mm and diameter of 1.6 mm.

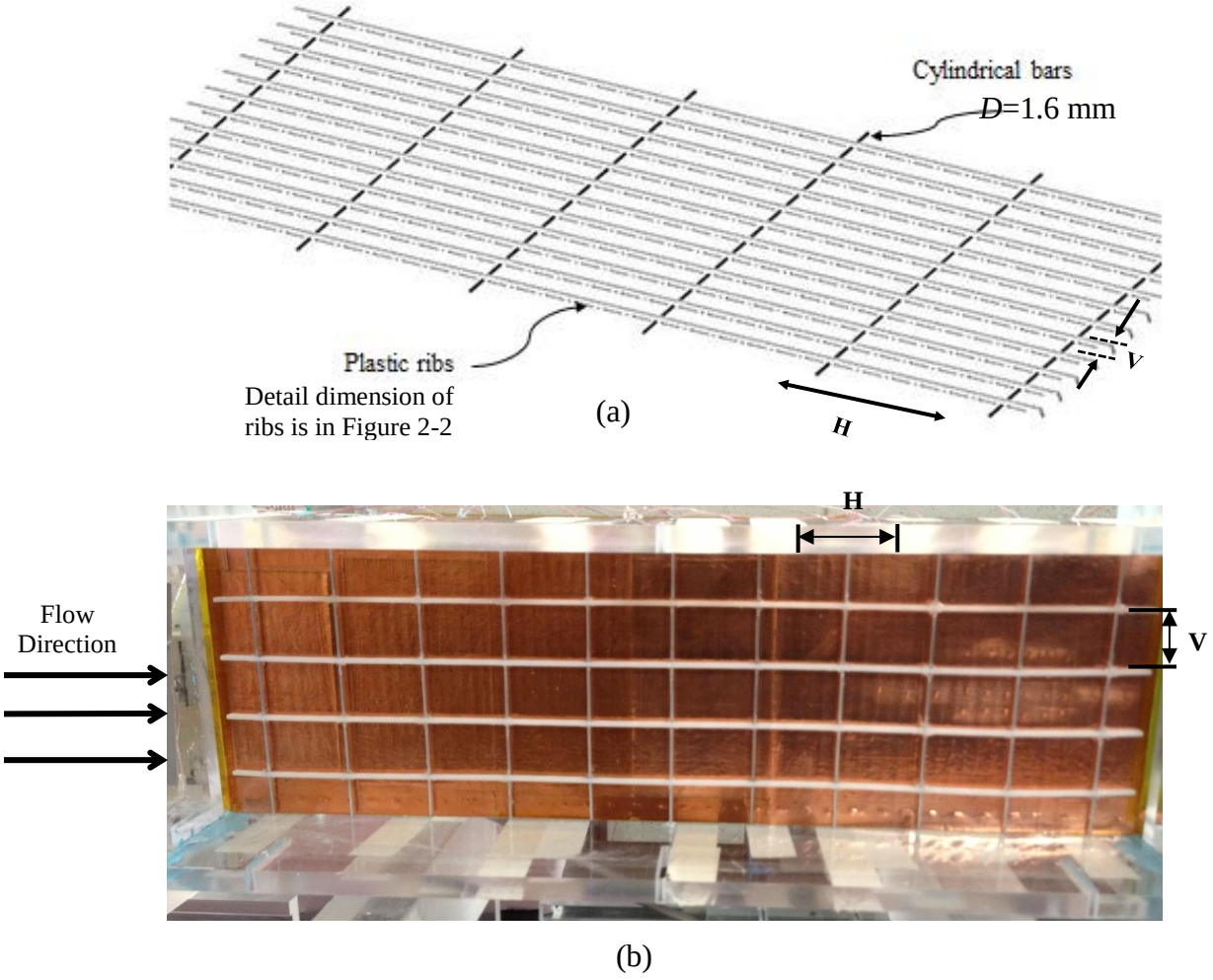

Figure 2-1 (a) Isometric view of an insert and (b) an insert inside the test section.

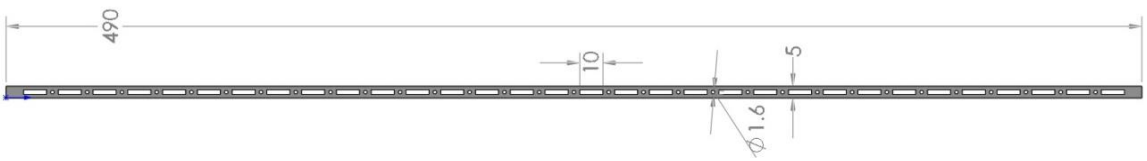

Figure 2-2 Top view and dimension of the plastic ribs (dimensions in mm).

Figure 2-1 (b) shows the front view photo of a turbulence enhancing insert placed inside the test section of the WEIT facility but with the front side of the test section sidewall removed. As Figure 2-1 (b) shows, H is the cylindrical bar interval distance and V is the plastic rib spacing. Nine inserts were tested during this research each with different spacing between the plastic ribs and cylindrical cross-bars. The ribs are placed either 30 mm, 20 mm or 10 mm apart, and the distance between the cross-bars is either 30 mm, 45 mm, 60 mm or 90 mm. Table 2-1 shows the dimensions of the turbulence enhancing inserts that are tested in this thesis and the nomenclature used to represent each case. For example, B90R10 means that the cylindrical cross-bars are 90 mm apart and the plastic ribs are 10 mm apart.

Table 2-1 Spacing between the cylindrical cross-bars (B) and the plastic ribs (R) of the turbulence enhancing inserts.

Case	Cylindrical bars intervals, H (mm)	Plastic ribs spacing, V (mm)	Case	Cylindrical bars intervals, H (mm)	Plastic ribs spacing, V (mm)
B90R10	90	10	B45R20	45	20
B90R20	90	20	B45R30	45	30
B90R30	90	30	B30R20	30	20
B60R20	60	20	B30R30	30	30
B60R30	60	30			

2.3. Apparatus and Procedure

The (WEIT) facility is presented in Figure 2-3 and is designed to produce hydrodynamically fully developed air flow with a constant and uniform temperature at the inlet of the test section. The ambient air is the working fluid and is drawn in by the vacuum pump at the downstream of the test facility. The main application of the WEIT facility is determining the enhanced convective heat transfer coefficient and increased pressure drop due to exchanger inserts. The heat transfer rate and pressure drop are measured along the test section. The total heat transfer rate is determined by measuring the mass flow rate of the air and the bulk air temperature at the inlet and outlet of the test section, while the pressure drop is determined by measuring the static pressure along the test section. The pressure drop and heat transfer measurements are conducted in steady state condition. The steady state condition is determined when a measured parameter, such as temperature or pressure, changes less than 0.2% from the average value in a period of 10 minutes. These measurements allow calculation of Nusselt number and Darcy friction factor for the insert using the methodology presented in Chapter3. The test section of the WEIT facility simulates the air channels in a LAMEE under the condition of constant heat flux on the side wall of the test section.

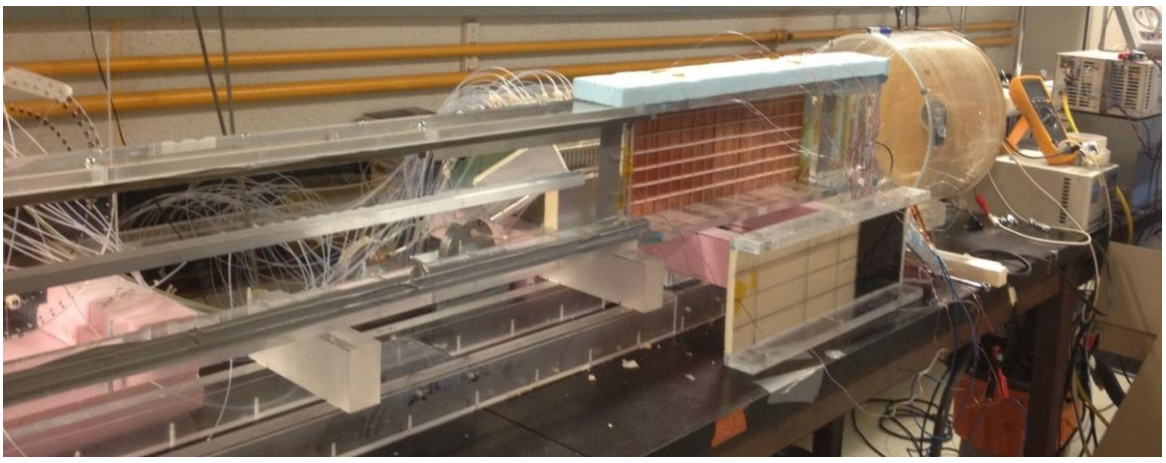

(a)

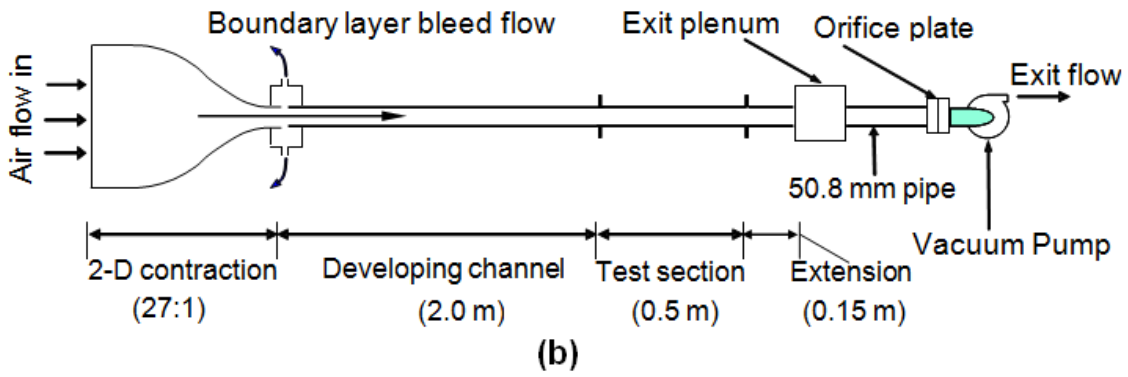

Figure 2-3 (a) Experimental facility (b) Schematic diagram of WEIT facility (top view).

2.3.1. Airflow Network

As shown in Figure 2-3(b) the WEIT facility consists of four main sections: a 2-D contraction nozzle, a developing section, a test section and an exit plenum. The 2-D contraction nozzle is 32 cm long with 27:1 contraction ratio. The air enters the nozzle and then accelerates smoothly before entering the rectangular developing channel. The developing channel and test section (Figure 2-3 (b)) have the rectangular cross section. They are 5 mm wide by 152.4 mm high.

The developing channel is 2 m long which allows the air flow boundary layer to become hydrodynamically fully developed before entering the test section. The channel walls are made of 12.5-mm acrylic plates. One of the 152.4-mm side walls of the developing channel has a slit cut-out for inserting a pressure probe. The probe can scan the dynamic pressure of the air flow in the channel located about 10 mm upstream of the test section inlet.

Figure 2-4 shows the test section and the extension channel located after the test section. At the outlet of the test section, the contraction nozzle with the contraction ratio of 15:1 and angle of 35° is located within the extension channel to mix the air and provide a more accurate measurement of the bulk air temperature. The bulk air temperature is measured at the outlet of the nozzle (Figure 2-4) by three thermocouples. The large plenum (with diameter of

306 mm and length of 309 mm) downstream of the extension channel is intended to reduce disturbances in the test section. The exit plenum also provides a transition from the rectangular test section to a circular pipe where the airflow rate is measured downstream of the exit plenum. The pipe with a diameter of 50.8 mm is connected to the downstream side of the exit plenum. The pipe section contains an orifice plate to measure the air mass flow rate. A commercial vacuum pump facilitates the air flow in the test facility as shown Figure 2-3(b).

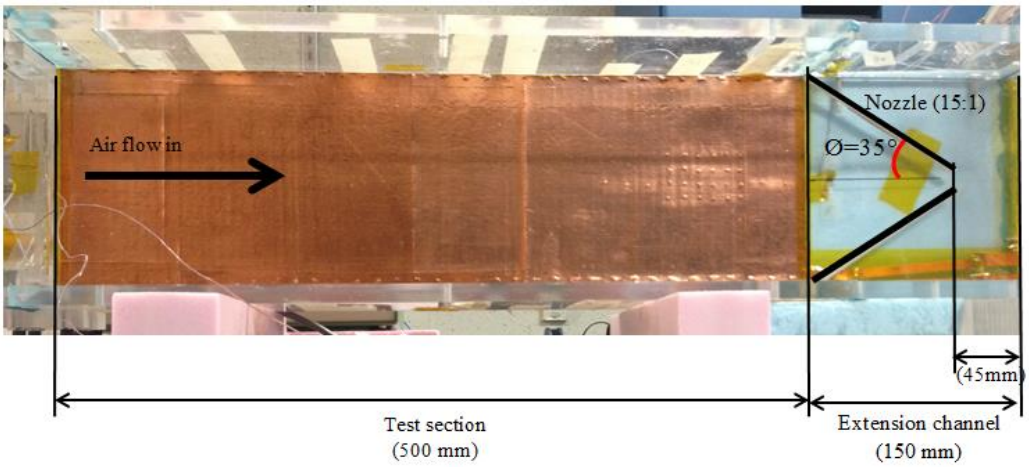

Figure 2-4 Detailed view of the test section and the extension channel.

2.3.2. Test section

Figure 2-6 shows the dimensions and top view of the test section in the WEIT facility. The test section dimensions are chosen based on the typical dimensions of an air channel in a LAMEE. The test section has the removable side walls with different side walls used for the heat transfer and pressure drop measurements.

2.3.2.1. Side wall for pressure drop measurement

The side wall that is designed for the pressure drop measurement is made of 12.5-mm-thick clear acrylic with 0.3-mm static pressure taps located along the centerline of the wall as shown in Figure 2-5. The pressure taps are located every 15 mm in the flow direction and the static pressure for each tube is read by the differential pressure transducer relative to the first

pressure tube located 10 mm downstream of the test section inlet. Details on the sensor and its calibration are given in Section 2.4.

The pressure taps are also drilled on the side walls of the developing channel to measure the static pressure in the hollow channel prior to the test section (channel without turbulence enhancing insert) as a reference for comparison with pressure drop across the turbulence enhancing insert in the test section. Moreover, the pressure drop measurements along the developing channel are used as an indication of the hydrodynamically fully developed flow. A total of 15 and 48 pressure taps are drilled on the side walls of the developing channel and the test section, respectively.

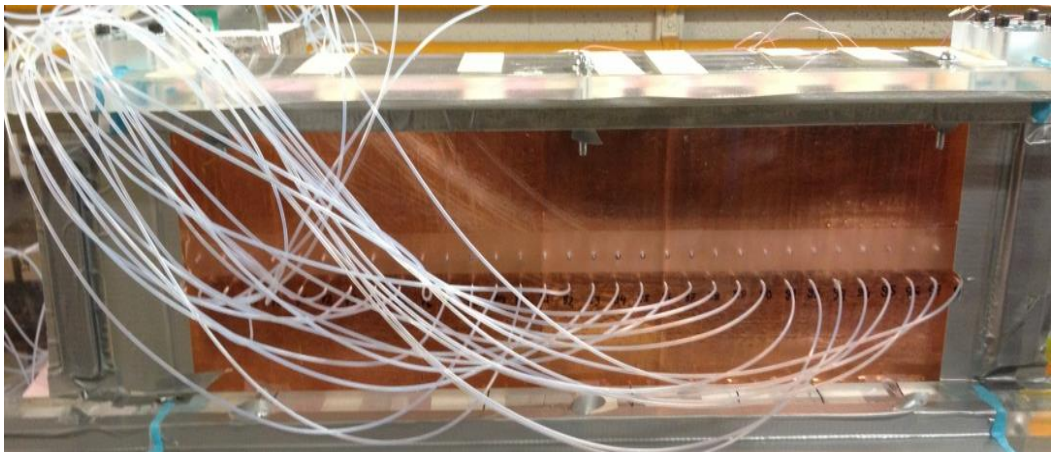

Figure 2-5 Side wall of the test section with pressure tubes.

2.3.2.2. Side wall for heat transfer measurement

The sidewalls for the heat measurements are made of acrylic and fitted with heaters and T-type thermocouples as shown in Figure 2-6. The heaters strip are 6.4 mm wide and 0.07-mm-thick and are made of copper. The copper strips (McMaster-CARR Copper foil tape with non-conductive adhesive) are attached side by side, 0.3 mm apart on the acrylic wall and soldered in a serpentine pattern to form a continuous heater on the flow side of the wall. The

copper strips are covered with 0.08 mm thick copper foil to provide a constant heat flux along the test surface.

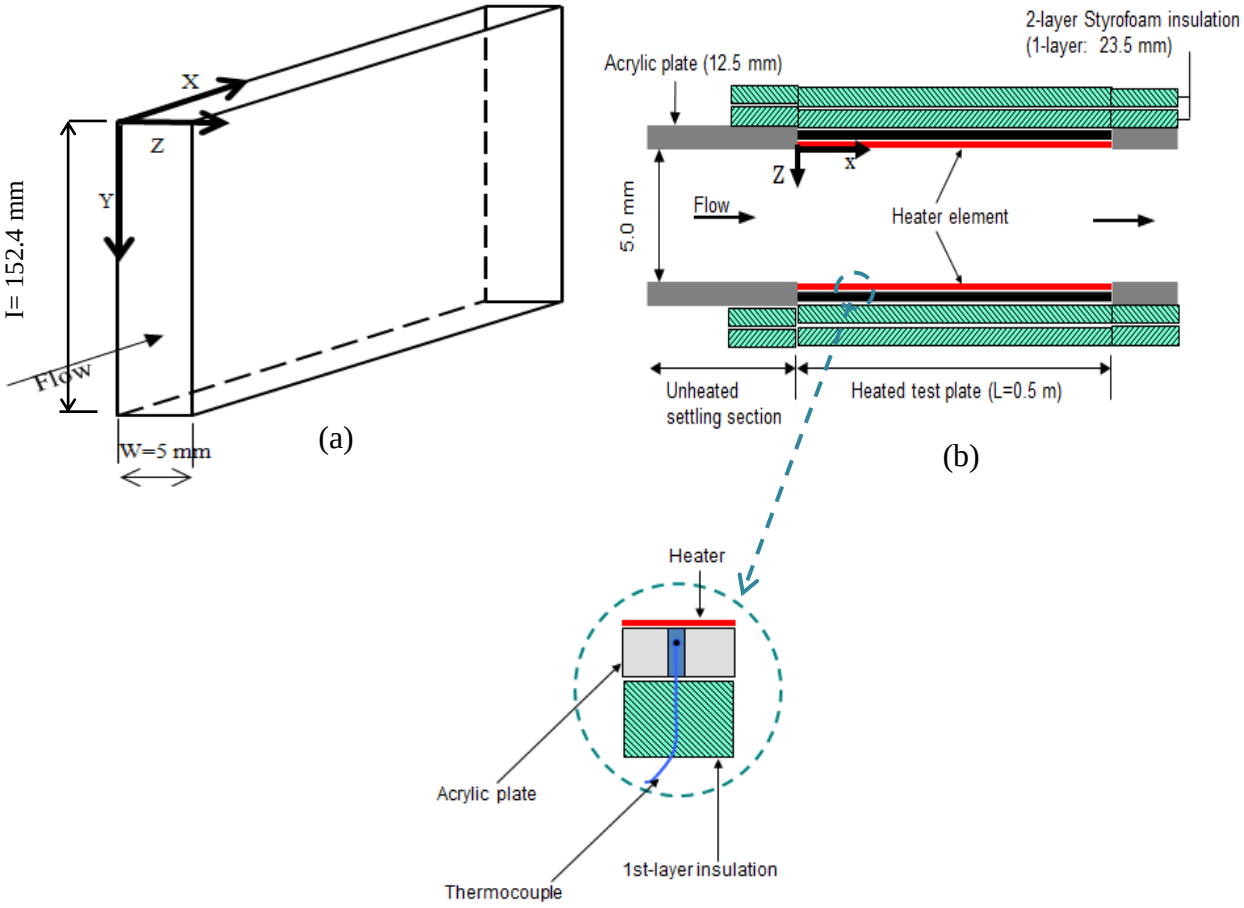

Figure 2-6 Isometric (a) and side (b) views of the rectangular test section showing the coordinate system, dimensions, insulation and location of the thermocouple near the heater element.

Figure 2-6 shows that each side wall of the test section has an electrical heater. Two power supplies (LAMBDA - LLS9040) are implemented to regulate the voltage for each heater. As shown in Figure 2-6 (b) the test section walls are insulated with two layers of 23.5-mm-thick insulation during the heat transfer measurements. The Cartesian coordinate system for the data analysis is also shown in Figure 2-6. There are thermocouples located between the

insulation layers and between the insulation layer and acrylic wall to measure the heat lost from the side, top and bottom walls of the test section. Figure 2-7 shows the location of thermocouples on the side walls of the test section.

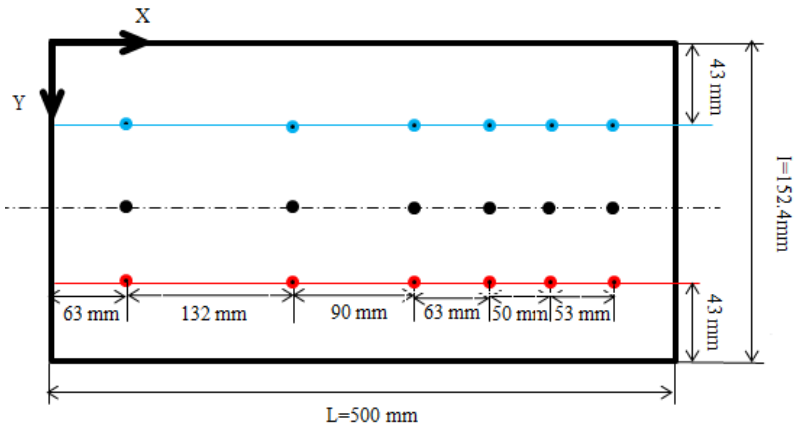

Figure 2-7 Front view of the side wall showing the location of the thermocouples between the side walls and the insulation.

The air temperature and the wall surface temperature need to be measured at the inlet and outlet of the test section to calculate the air convective heat transfer coefficient within the test section. The inlet air temperature is measured by three thermocouples which are located at X = -10 mm and Y equals to 40 mm, 76 mm, and 112 mm. The outlet temperature of the air is measured by three thermocouples located at the nozzle exit (Figure 2-4), in the extension channel.

The wall surface temperature is measured by thermocouples at the inlet and outlet of the test section. Figure 2-8 shows the location of the thermocouple tips, inserted through the drilled holes in the test plate and placed just below the heater elements. Four thermocouples are embedded at X = 10 mm and the other four thermocouples are located at X = 490 mm to measure the side wall surface temperature at the inlet and outlet of the test section, respectively. The thermocouples at each side are 10 mm apart, in the Y direction.

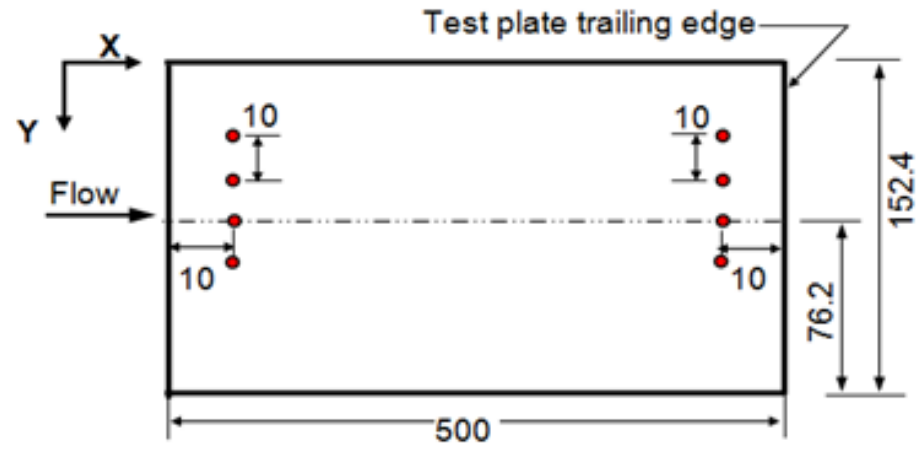

Figure 2-8 Thermocouples location for the wall temperature measurements along the test plate (all dimensions are in mm).

2.3.3. Data Acquisition

A personal computer with National Instruments (NI) LabVIEW® 10.0 is used to record the experimental data. Figure 2-9 presents the interface of the LabVEIW which is designed to read and record the data from the thermocouples, heaters, and pressure transducers. The thermocouples are connected to a 24-bit (NI 9214) data acquisition card and the pressure transducers are connected to a 16-bit (NI 9105) analogue input module. The 24-bit data acquisition card and 16-bit analogue input module are connected to the computer through a NI CDAQ 9178 chassis. All the temperature, air flow rate, and pressure data are the mean of 100 samples collections over the 10 seconds. All the measurement data are recorded every 30 seconds.

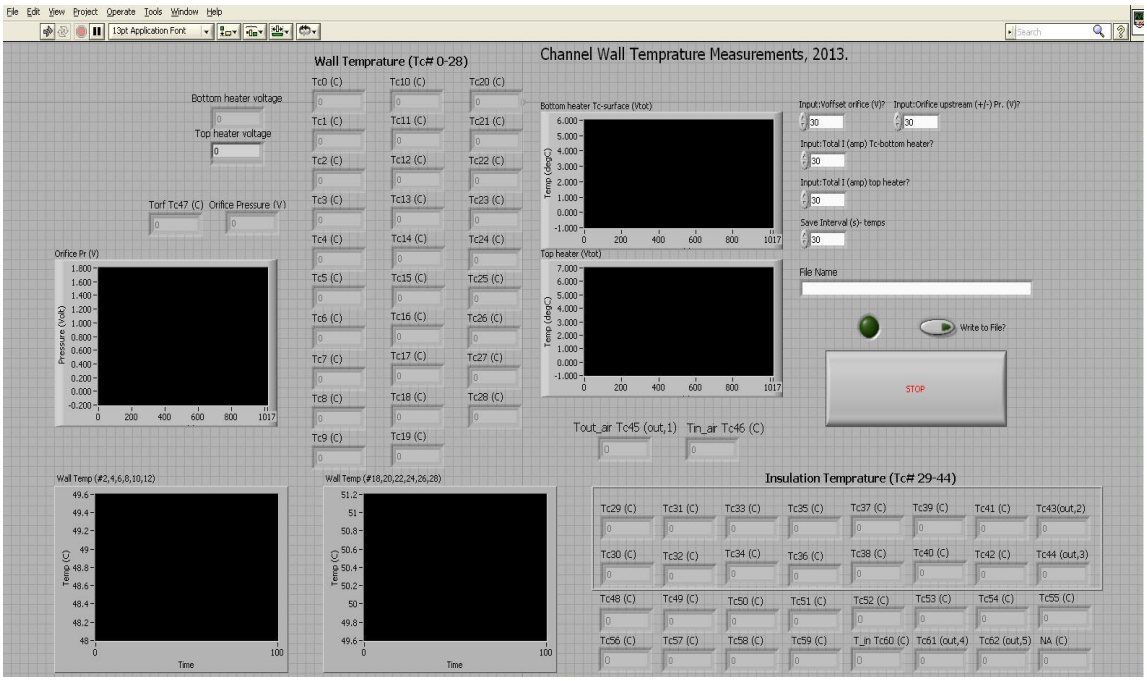

Figure 2-9 LabView graphical user interface.

2.4. Measurement and instrument calibration

This section provides an overview of the instrumentation for measuring the convective heat transfer coefficient and pressure drop across a turbulence enhancing insert inside the rectangular test section of the WEIT facility. All the instruments are calibrated and their total uncertainties are calculated.

2.4.1. Temperature sensors

T-Type thermocouples are used to measure the wall surface temperature and bulk air flow temperature at the inlet and outlet of the test section. Thermocouples are calibrated against the dry-well temperature generator (Hart scientific 9107 by Fluke Company) in a temperature range of 15-70°C. A calibration curve is generated for each thermocouple based on the read temperature of the thermocouples and temperature generator (reference temperature). The total 95% bias uncertainties of the thermocouples range from ±0.1°C to ±0.2°C including the bias uncertainty of the dry-well temperature generator which is ±0.1°C

[20]. The maximum total uncertainty of ±0.2°C is used for the thermocouples in all uncertainty calculations.

The bulk air temperature at the upstream and downstream of the test section is measured with three thermocouples at the inlet and outlet of the test section, respectively. The measured temperatures by each thermocouple had no greater difference than 0.1°C compared to the other thermocouples at the same location. Since the difference between the measured temperature by three thermocouples either at the inlet or outlet of the test section is less than the uncertainty of the thermocouples, the average air temperature is reported in results.

2.4.2. Pressure transducer

Validyne DP15-20 and DP103 electric pressure transducers are used in the WEIT facility to measure the pressure drop across the orifice plate and the static pressure within the developing channel and the test section, respectively. A Druck precision portable pressure calibrator (DP6105) is used to calibrate the pressure transducers. The maximum outputs of the transducers are set to 10 volts, and the sensors DP15-20 and DP103 are calibrated over their range of application which is 837 Pa for DP15-20 (orifice plate pressure drop) and 84 Pa for DP103 (pressure drop within the test section). Figure 2-10 (a) and Figure 2-10 (b) show the calibration curves for DP15-20 and DP103 pressure transducers, respectively. The total bias uncertainty of the pressure transducers is due to the data reduction error and the precision uncertainty of the Druck.

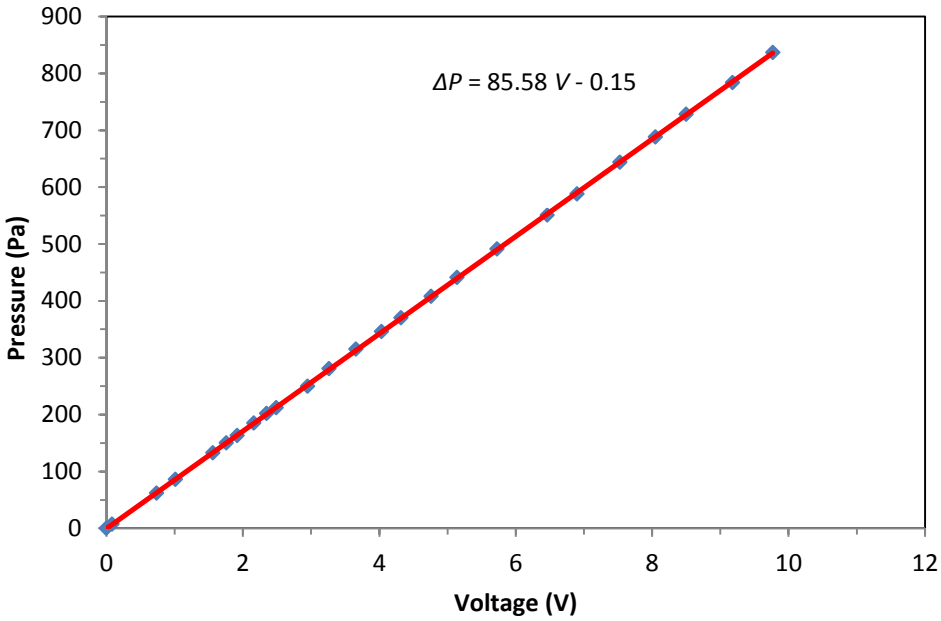

(a)

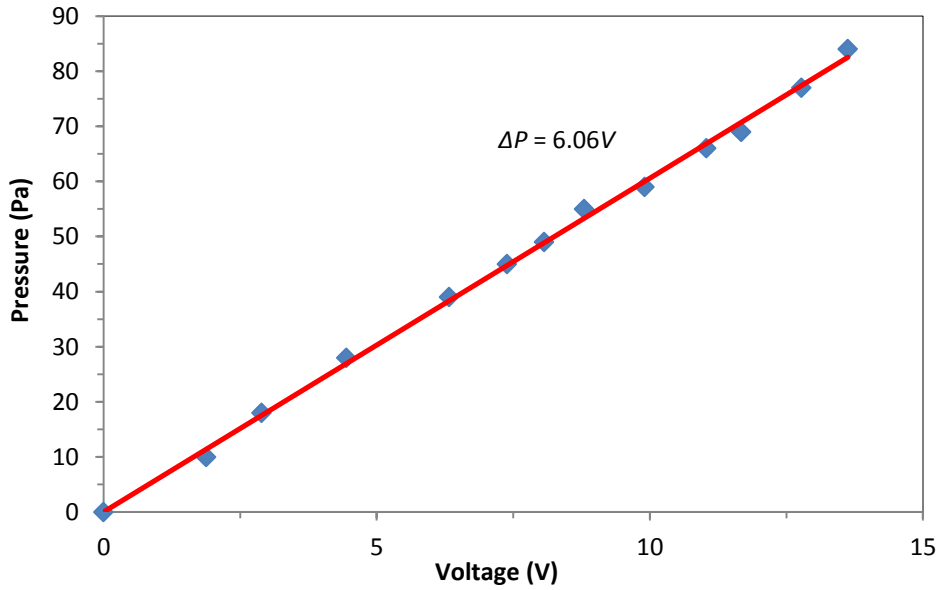

(b)

Figure 2-10 Calibration curve for (a) DP15-20 (orifice plate transducer), (b) DP103 (test section pressure transducer).

The data reduction error of DP15-20 and DP103 is calculated as ±2.5 Pa and ±0.6 Pa, respectively. The precision uncertainty of the Druck is ±1 Pa, which corresponds to the smallest significant number of the reading pressure. The bias uncertainty of the Druck is ±0.1

Pa. Propagation of the data reduction error and the precision uncertainty of the Druck gives the total bias uncertainty of DP15-20 and DP103, which is ±3.1 Pa and ±1.2 Pa, respectively.

2.4.3. Orifice plate

As Figure 2-3 shows the pipe section with 50.8 mm diameter at the downstream of the WEIT facility contains an orifice plate to measure the air flow rate in the test section. The pipe length is 134 cm upstream of the orifice plate exceeding the minimum pipe length required in [21]. The mass flow rate of air is measured based on the pressure drop across the 12.5 mm tapered orifice plate. The differential pressure across the orifice plate is measured with the pressure transducer (Validyne DP15-20) with a full scale reading of 800.0 ± 3.1 Pa.

The orifice plate is calibrated against three different mass flow controllers, each with a bias uncertainty of ±0.05 g/s, using a duct with the same piping dimension as the WEIT facility. Figure 2-11 presents the calibration curve for the 12.5-mm orifice plate against three flow controllers.

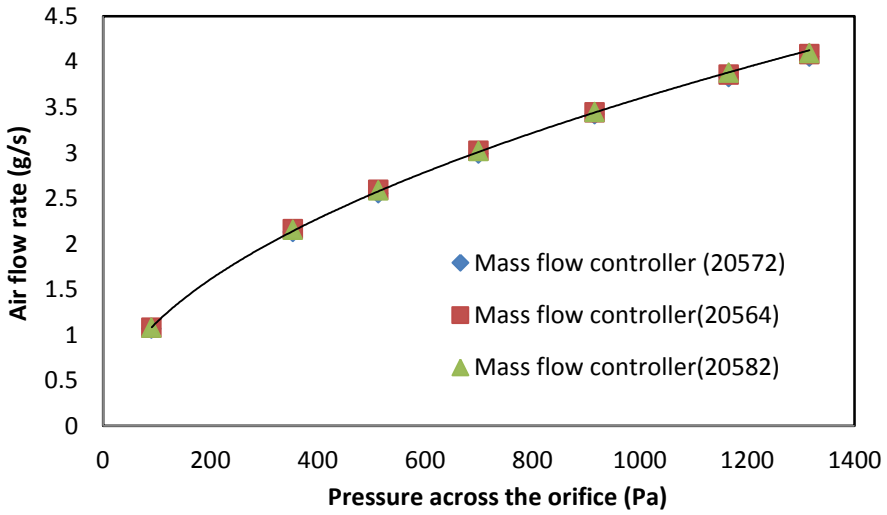

Figure 2-11 Calibration data for the 12.5 mm orifice plate.

Equation (2-1) shows the relation of the mass flow rate and the pressure drop for the 12.5 mm orifice plate, which is calculated from the experimental data.

$$\dot{m} = 0.00011 \Delta P^{0.5}, \quad (2\text{-}1)$$

where $\dot{m}$ is the mass flow rate of the air [g/s] and ΔP is differential pressure [Pa]. The differential pressures in the experiments range from 100 Pa to 700 Pa. The total uncertainty of the differential pressure for the orifice plate varies from ±5% to ±1% for the pressure range of 60 Pa to 877 Pa.

2.5. Commissioning of WEIT facility

2.5.1. Mass balance procedure

The mass flow rate of the air is measured by the orifice plate at the downstream of the WEIT facility and the measured value is used in all the calculations. Since the experimental measurements are conducted within the test section, the measurement of the mass flow rate by the orifice plate should be in balance with the inlet air flow to the test section.

The inlet mass flow rate of the air is measured by a pressure probe (Figure 2-12) at the entrance of the test section to compare the orifice plate measurement with the inlet air mass flow rate to the test section. The inlet air mass flow rate to the test section is calculated from the dynamic pressure by measuring the total pressure and static pressure within the channel. The static pressure is constant in the YZ plane (Figure 2-3) and measured by the 0.3-mm pressure tube drilled to the side walls of the developing channel. The total pressure probe with a diameter of 0.3 mm is inserted into the channel through a slit on the sidewall of the developing channel, 10 mm upstream of the test section. The head of the probe is located in the channel parallel to the airflow stream. Figure 2-12 shows the total pressure probe for measuring the total pressure in the channel.

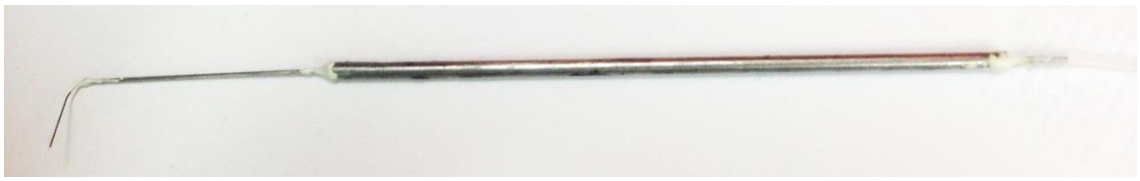

Figure 2-12 Total pressure probe with diameter of 0.3 mm.

The dynamic pressure at each location of the pressure probe is identified by the pressure transducer which measures the difference of the total pressure and the static pressure. A two-axis motorized traverse (bislide positioning system, Velmex XN10-0060-E25-71) moves the probe for scanning the total pressure within the channel cross section and locates the probe at the desired Y and Z location inside the channel. Figure 2-13 shows the bislide positioning system.

The Velmex bislide positioning system has two slides with servo motors to position the probe at the desired Y and Z location. Each motor is individually controlled by a VM stepping motor controller (Figure 2-13). The commands are sent through the COSMOS software to move the Velmex bislide system and position the pressure probe inside the channel. The user has to define the number of steps and the velocity (steps per second) for each motor through the software to position the probe. Each slide has a lead screw with a pitch of 0.000625 in. (2×10^{-5} mm). The mass balance results will be presented in Section 3.4.

(a) (b)

Figure 2-13 Velmex bislide positiong system.

2.5.2. Fully developed flow at the entrance to the test section

The air velocity profile at the inlet of the test section is an important parameter that affects the convective heat transfer coefficient in the test section. The fully developed flow in the test section is important because the experimental results in this research could be compared to the data available in the literature; moreover, the effect of developing thermal boundary layer on the heat transfer can be determined.

In this research, hydrodynamically fully developed flow at the inlet of the test section is determined by measuring the velocity profile across the width of the developing channel and static pressure drop along the length of the developing channel.

2.5.2.1. Velocity profile

The velocity profile is determined by measuring the dynamic pressure across the width of the channel. Since the pressure probe has to be located with a distance of two times the probe diameter from the side walls to prevent the flow eddies near the wall from affecting the measurement, the traverse pressure measurement was performed across the channel width from Z = 1 mm to 4 mm with increments of 0.5 mm. Each measured pressure is the average of the

10 consecutive pressure readings in 6 seconds. The velocity at each location is calculated from equation (2-2) [22].

$$V_X = \sqrt{((P_{tot}-P_{static})/0.5\rho)}, \quad (2\text{-}2)$$

where, V_X is the local velocity of the air at X = -10 mm and specific Y and Z in the channel [m/s], P_{tot} is the total pressure measured [Pa], P_{static} is the static pressure [Pa], and ρ is the density of the air [kg/m^3].

The measured velocities are corrected by using correction equations given in the Refs. [23], [24]. The correction equation given in Ref. [24] takes into account the displacement effect of the pressure probe in a shear flow. Figure 2-14 shows the traverse velocity measurement across the width of the developing channel for the laminar flow (Re = 2100) at X = -10 mm and three different Y locations.

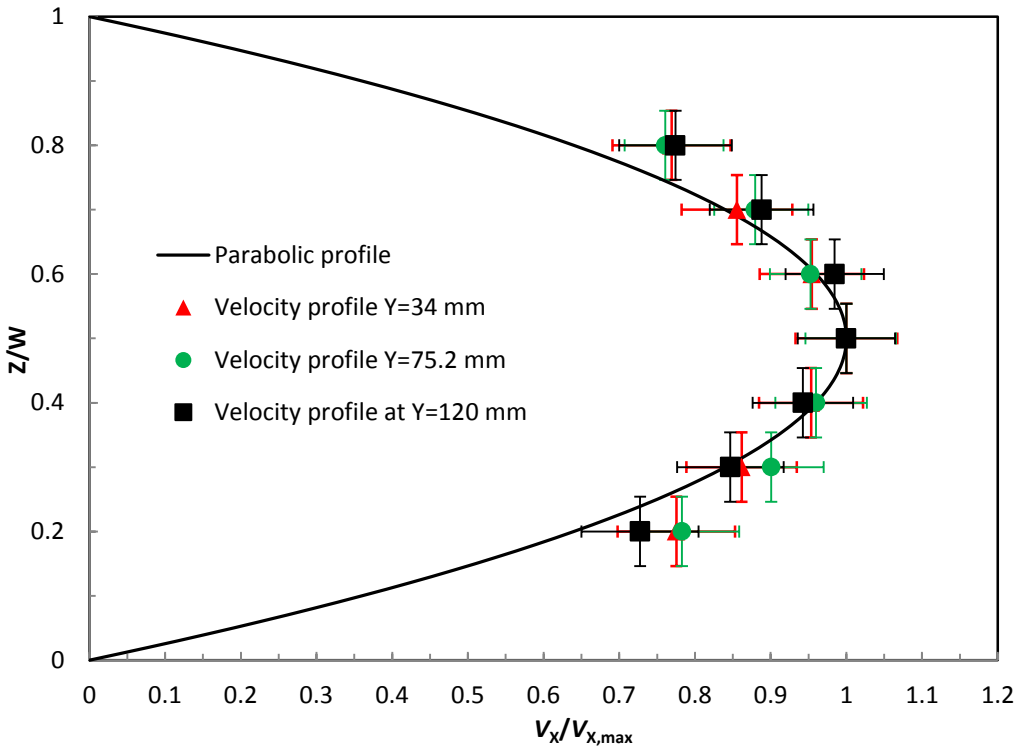

Figure 2-14 Laminar velocity profile at X=-10 mm. The 95% uncertainties in velocity measurements are shown with error bars.

As Figure 2-14 shows the air flow velocity profile for the laminar flow follows the ideal parabolic Poiseuille velocity profile, which indicates that the flow is hydrodynamically fully developed. The 95% uncertainty in the velocity ratio is calculated based on the bias uncertainty and standard deviation of the mean local velocity over the maximum velocity of the air flow in the channel and shown with uncertainty bars in Figure 2-14. Moreover, the uncertainty of the pressure probe tip location inside the channel is based on the accuracy of the bislide positioning system and equals to ±0.1 mm, which gives the uncertainty of ±0.05 for Z/*W* (shown in the Figure 2-14).

2.5.2.2. Pressure drop

The pressure drop along the developing channel and the test section (without inserts) is measured from X = -290 mm to X = 490 mm with respect to the first pressure tap on the test section (X=10 mm) at Re = 1600 and the experimental data are shown in Figure 2-15. The 95% uncertainties in measured static pressure drop are shown with uncertainty bars in Figure 2-15 including the bias uncertainty of the pressure transducer and the precision uncertainty of the experimental data.

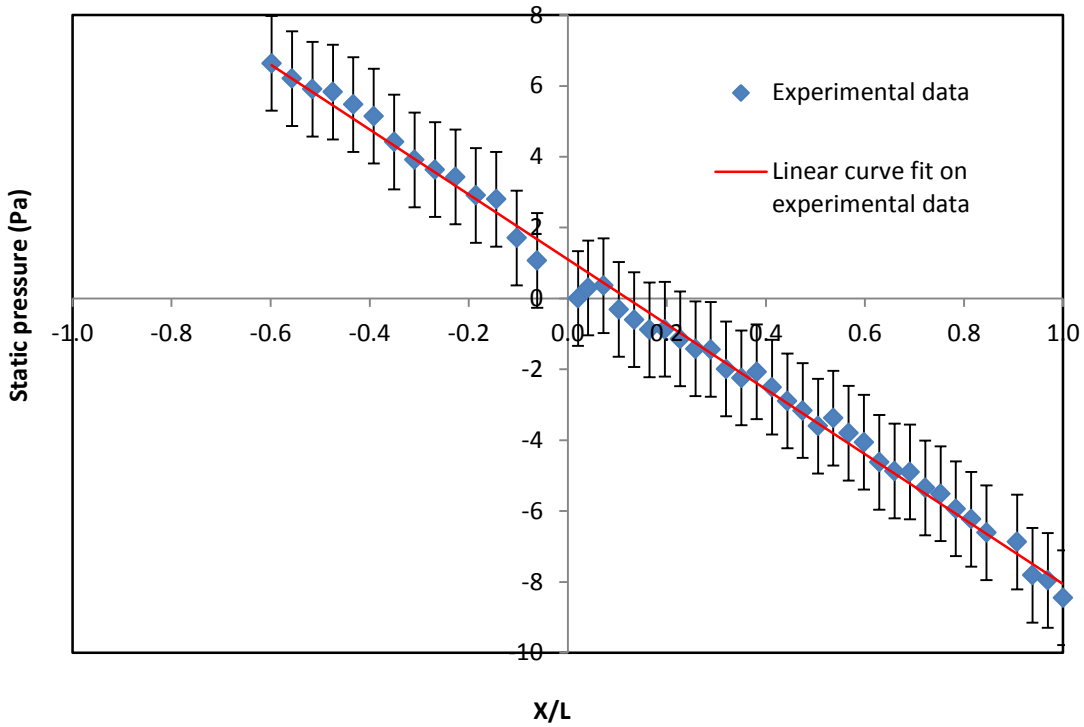

Figure 2-15 Static pressure drop along the developing channel and the test section without inserts (X/L = 0 corresponds to the inlet of the test section).

The static pressure varies linearly with X indicating that the flow is hydrodynamically fully developed. The nonlinear pressure data from X/L = -0.1 to 0.1 is due to a small gap between the side walls of the developing channel and the test section. Since the pressure gradient is linear at the inlet of the test section and through the test section (Figure 2-15) and the velocity profile is nearly parabolic (Figure 2-14), the air flow at the inlet of the test section is hydrodynamically fully developed. The ΔP/L for the laminar flow between the parallel plates is reported -20.1±2.6 Pa/m at the tested Reynolds number of 1600 [22], which corresponds to an average velocity of 2.6 m/s in the test section. The experimental data in Figure 2-15 shows that the ΔP/L is -18.4±1.3 Pa/m. The experimental pressure gradient agrees with the theoretical value available in the literature within their uncertainties.

The fact that the experimental pressure gradient is lower than the theoretical value may be due to slight leakage in the WEIT facility and possible slight expansion of the test section. Both of these effects are considered in the uncertainty of the theoretical pressure gradient (i.e., ±2.6 Pa/m). For example, Section 3.4 will show that the mass balance is within ±0.1 g/s meaning that the mass flow rate of air through the test section may be 0.1 g/s lower than the mass flow rate of air at the orifice plate due to leakage. Assuming this leakage rate, gives a possible actual velocity of 2.4 m/s in the test section and a pressure gradient of ΔP/L of 19.2 Pa/m. Therefore, leakage alone does not account for the difference between the experimental and theoretical pressure gradients.

CHAPTER 3
DATA ANALYSIS METHOD

3.1. Introduction

This chapter presents the methodology used to determine the Darcy friction factor and convective heat transfer coefficient (Nusselt number) within the test section of the WEIT facility. The bias and precision uncertainties of the calculated variables are also presented in this chapter. Finally, the mass and energy conservation equations are applied to the experimental data to show that mass and energy are conserved within experimental uncertainty bounds.

3.1. Entrance effects

Chapter 2, Section 2.4 shows that the flow is hydrodynamically fully developed at the entrance of the test section of WEIT facility. The air flow has the ambient air temperature which enters the test section with a uniform temperature profile. The heaters are located in the side walls of the test section and these are in contact with the air flow. The heat from the walls is transferred to the airflow by convection through the thermal boundary layer which begins to develop at the entrance of the test section. This forced convective flow thermal entry length is calculated by equation (3-1) [22]. As the channel in the test facility has the rectangular cross section, the characteristic length is defined by hydraulic diameter in equation (3-2).

$$\left(\frac{x_{\mathrm{fd,t}}}{D_{\mathrm{h}}}\right)_{\mathrm{lam}} \approx 0.05\ \mathrm{Re}\ Pr, \tag{3-1}$$

(for a hollow flow channel with Pr = 0.7)

$$D_{\mathrm{h}} \equiv \frac{4A_{\mathrm{c}}}{P} \tag{3-2}$$

The hollow channel tests are conducted for Re (calculated based on hydraulic diameter) between 900 and 2200, which corresponds to thermal entry lengths between 315 mm and 757 mm. Since the test section is only 500 mm long, the thermal entrance length is important for all the tests. Table 3-1 shows the thermal entry length for each Reynolds number that is tested for the hollow channel.

Table 3-1 Thermal entry length for the experiments conducted in the hollow channel.

Air flow velocity (m/s)	Reynolds number	$x_{\mathrm{fd,t}}$ (mm)	Air flow velocity (m/s)	Reynolds number	$x_{\mathrm{fd,t}}$ (mm)
1.5	920	321	3	1850	646
2	1260	439	3.5	2160	757
2.5	1550	541			

3.2. Dimensionless variables and properties

The main purpose of the experiments is to measure properties needed to determine the friction factor and Nusselt number and show how they vary as a function of the Reynolds number.

3.2.1. Reynolds number (Re)

The Reynolds number in the channel is calculated based on the mass flow rate and the channel hydraulic diameter. The aspect ratio of the hollow channel is 1:30.5 providing a hydraulic diameter of $2W$ (two times the channel width), which is the same as for flow between two infinite parallel plates [22]. The Reynolds number is calculated by equation (3-3).

$$\mathrm{Re} = \frac{\rho V_{\mathrm{ave}} D_h}{\mu_{\mathrm{f}}}, \tag{3-3}$$

where ρ is the density of the air [kg/m^3], V_{ave} is the average velocity of the air [m/s], D_h is the channel hydraulic diameter [m], and μ_{f} is the viscosity of the dry air [N·S/m^2]. All the data are reported based on the Reynolds number within the hollow channel at the entrance of the test section.

All the properties are determined at the average of the bulk air inlet and outlet temperatures,

$$T_{\mathrm{ave}} = \frac{T_{\mathrm{air,in}} + T_{\mathrm{air,out}}}{2}, \tag{3- 4}$$

where T_{ave} is the average temperature and, $T_{\mathrm{air,in}}$ and $T_{\mathrm{air,out}}$ are the bulk air temperature at the inlet and outlet of the test section, respectively.

The viscosity of the dry air (μ_{f}) is calculated based on the Sutherland law at T_{ave} [22],

$$\mu_f = \mu_0 \left(\frac{T_{\mathrm{ave}}}{T_0} \right)^{3/2} \left(\frac{T_0 + S}{T_{\mathrm{ave}} + S} \right), \tag{3- 5}$$

where μ_0 =1.71 E-5 [N·S/m^2], T_0 =273 [K], and S =110.4 [K].

3.2.2. Friction factor (f_D)

The pressure drop is an important parameter to determine the fan or pumping power requirements. Since the turbulence enhancing inserts increase the pressure drop inside the channel compared to the hollow channel, it is important to study this parameter. The pressure drop inside the channel is measured with the static pressure taps along the side walls of the test section and quantified with the friction factor, which is the dimensionless wall shear stress and defined in equation (3-6),

$$f_D \equiv \frac{-(dP/dx)2D_h}{\rho V_{\text{ave}}^2}, \tag{3-6}$$

where f_D is the Darcy friction factor, dP/dx is the pressure gradient along the test section [Pa/m], D_h is the hydraulic diameter [m], and V_{ave} is the air bulk mean velocity [m/s].

3.2.3. Nusselt number (*Nu*)

The heat transfer enhancement in the literature is usually presented by the Nusselt number which, for laminar flow, can be interpreted as the dimensionless temperature gradient of the fluid normal to the heat flux surface [19]. A larger Nusselt number in the channel means a greater temperature gradient at the heated surface,

$$Nu = \frac{h_{\text{ave}} D_h}{k_{\text{air}}}, \tag{3-7}$$

where Nu is the average Nusselt number, h_{ave} is the average convective heat transfer coefficient [W/m^2·K], and k_{air} is the thermal conductivity of the air [W/m·K]. Since the thermal conductivity of the air changes with the air temperature, the thermal conductivity of the air is calculated at the T_{ave} (K) using the following equation [22].

$$k_{\text{air}} = 1.5207\text{E}11\,T_{\text{ave}}{}^3 - 4.8574\text{E}-8\,T_{\text{ave}}{}^2 + 1.0184\text{E}-4\,T_{\text{ave}} - 0.00039333 \tag{3-8}$$

When an insert is installed, the Nusselt number depends on the geometry of the insert and the Reynolds number. Since the insert ribs are not bonded to the membrane surface, it is most convenient to assume the insert does not increase the heat transfer area.

The average convective heat transfer coefficient is calculated from the measured heat flux to the air and the logarithmic mean temperature difference according to equations (3-9) and (3-10),

$$Q_{\text{air}} = h_{\text{ave}} A \Delta T_{\text{lm}}, \tag{3-9}$$

$$Q_{\text{air}} = \dot{m} C_{\text{p,air}} (T_{\text{air,out}} - T_{\text{air,in}}), \tag{3- 10}$$

where Q_{air} is the heat transfer rate from the heaters to the air in the test section [W], A is the surface area of the side walls, h_{ave} is the average convective heat transfer coefficient [W/m^2·K], ΔT_{lm} is the log mean temperature difference for the air flow [K], $\dot{m}$ is the mass flow rate of air [kg/s], and $C_{\text{p,air}}$ is the heat capacity of the air [J/kg.K]

3.2.3.1. Heat Flux

The total heat power input is calculated by measuring the input voltage and current to the heater. The heat flux in equation (3-9) is determined by subtracting the conduction losses from the total power heat input and dividing by the air-side surface area of the heater. The conduction losses from the test section are measured by the embedded thermocouples in the sidewalls of the test section and between the insulation (Figure 2-8). The conduction loss heat flux at the position of each thermocouple is calculated by equation (3-11),.

$$Q''_{\text{loss}} = \frac{k_{\text{insul}}(T_{\text{wall,surf}} - T_{\text{insul}})}{t_{\text{insul}}}, \tag{3-11}$$

where Q''_{loss} is the conduction heat flux from the test section to the surrounding [W/m^2], k_{insul} is the thermal conductivity of the Styrofoam [W/m·K], $T_{\text{wall,surf}}$ is the wall surface temperature [K], T_{insul} is the measured temperature between the insulation [K], and t_{insul} is the insulation thickness which is 23 mm. The thermal conductivity of the Styrofoam is 0.03±0.005 (W/m·K) which is measured by the Fox 314 apparatus in the Thermal lab at the University of Saskatchewan [25].

The conduction losses are measured at 18 points along the test section wall. There are 6 points in the flow direction and 3 rows along the height of the test section (Y = 43 mm, 76 mm, and 109.4 mm in Figure 2-8). The heat loss is calculated at each point for a specific height and the data are curve-fitted at each row as shown in Figure 3-1. Each curve fitting equation is integrated over one third of the side wall area and the summation of three integrated equations gives the total heat loss from the side walls to the surroundings. Figure 3-1 shows the calculated conduction losses at the center line of the test section for the hollow channel test at Re = 920. The calculated heat losses in other rows are in the same range of the center line.

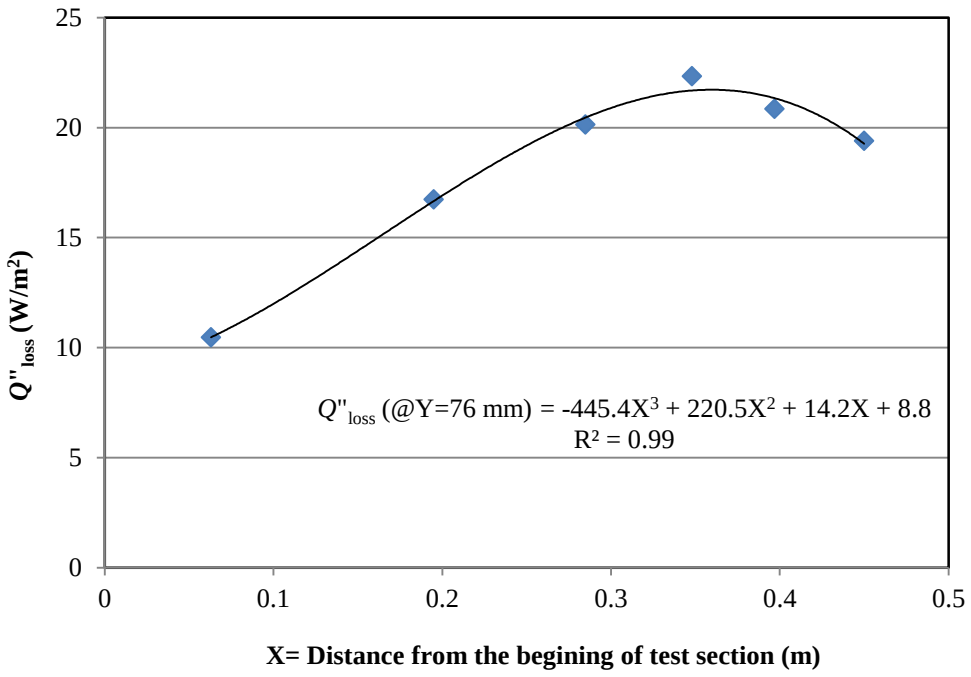

Figure 3-1 Conduction loss from the test section measured at the center line of the test section at Re = 920 (Q_{air}/A = 346 W/m^2).

3.2.3.2. Log mean temperature difference

The log mean temperature difference is calculated by measuring the air temperature at the inlet and outlet of the test section and the side walls surfaces of the test section.

$$\Delta T_{\mathrm{lm}} = \frac{[(T_{\mathrm{surf,in}} - T_{\mathrm{air,in}}) - (T_{\mathrm{surf,out}} - T_{\mathrm{air,out}})]}{\ell n[(T_{\mathrm{surf,in}} - T_{\mathrm{air,in}})/(T_{\mathrm{surf,out}} - T_{\mathrm{air,out}})]}, \tag{3-12}$$

where T is the temperature [K], and subscripts "surf", "air", "in" and "out" represent surface, air, and inlet and outlet of the test section, respectively.

3.3.The bias and precision uncertainty of calculated parameters

In order to ensure confidence in the results, the uncertainty of the measured and calculated values should be determined. The uncertainties in the measured data are estimated based on the 95% confidence interval and the errors in the computed values are determined based on the root-sum-square propagation of the uncertainties [20],

$$U_{\mathrm{T}} = \sqrt{(B)^2 + (P)^2}, \tag{3-13}$$

where U_{T} is the total uncertainty at 95% confidence level, B is the total bias uncertainty, and P is the total precision uncertainty of a parameter. The precision uncertainty is defined as:

$$P = t\left[\sqrt{\frac{\sum_{i=1}^{N}(x_i - \bar{x})^2}{N(N-1)}}\right]^{1/2}, \tag{3-14}$$

where t is the student's t value at a 95% confidence level.

3.3.1. Reynolds number

The uncertainty of Re is propagation of the uncertainty in the density of the air, the viscosity of the air, the uncertainty of the average velocity of the airflow and the uncertainty in the hydraulic diameter of the channel. The total uncertainty of the density and viscosity of the air is ±1%. The total uncertainty of the hydraulic diameter of the channel is ±2%. The uncertainty of the average velocity of the air is mainly due to the mass flow rate measurement

across the orifice plate. Since the uncertainty in the mass flow rate measurement is ±5% at Re = 920 and ±3.6% at the Re = 2150, the total uncertainty of the average velocity of the air ranges from ±4% to ±5.5%. Therefore, the total uncertainty of the Re ranges from ±5% to ±6% of the measured value.

3.3.2. Friction factor

The total uncertainty of the Darcy friction factor is the function of the total uncertainty in static pressure, average velocity of the air in the test section, the density and the hydraulic diameter of the channel. The maximum uncertainty in the wall static pressure is ±1.2 Pa. The total uncertainty of the Darcy friction factor ranges from ±8% to ±11%. Also, the total uncertainty of the pumping power ranges from ±7% to ±10%. The total uncertainty of the pumping power is due to the total uncertainty of the static pressure drop, and the mass flow rate measurements.

3.3.3. Nusselt number

The maximum uncertainty of the total heat flux is ±3%, which is due to the uncertainty of the input voltage by the power supply and the conduction loss measurements from the test section walls. The total uncertainty of the conduction loss measurements is ±2%.

The total uncertainty of the Nusselt number is based on the uncertainty of the convective heat transfer coefficient, the hydraulic diameter of the channel and the thermal conductivity of the air. The ±3% uncertainty in the total heat flux and ±0.3°C uncertainty in the log mean temperature difference results in ±4% to ±5% total uncertainty in the calculated convective heat transfer coefficient. The total uncertainty of the thermal conductivity of the air is ±1%, which is due to the uncertainty of the air temperature measurements. Therefore, the calculated Nusselt number has a total uncertainty of ±5% to ±7%.

3.4. Mass and energy balances

The principles of conservation of mass and energy are applied to the WEIT facility to verify that the mass and energy balances are satisfied within the experiments' uncertainty bounds.

The orifice plate measures the mass flow rate of the air and is located downstream of the test section. It is necessary to ensure that there is no leakage in the test facility and the inlet air mass flow rate to the test section is the same as the mass flow rate at the orifice plate. The pressure probe with a diameter of 0.30 mm (Figure 2-12) is inserted into the channel through a slot on the sidewall of the developing channel (X = -10 mm). Since the flow is fully developed at this location, the velocity profile in the Z direction is constant from top to bottom (at different Y locations) of the channel (Figure 2-6). The dynamic pressure is measured at 9 different heights, while the probe location within the width of the channel is changed from 1 mm to 4 mm by increments of 0.5 mm. The velocity at each location is calculated from equation (2-2).

The average velocity at a specific height within the channel is calculated by $1/W\int_0^5 V_X dZ$ by assuming a no slip condition at the sidewalls. The mass balance was assessed at Re = 2160, which corresponds to the average air velocity of 3.5 m/s. In this experiment the mass flow rate of the air at the inlet of the test section was calculated to be 2.9±0.3 g/s and the mass flow rate at the orifice plate (downstream of the WEIT facility) measured was to be 3.0±0.1 g/s. Also, the same experiment was conducted at Re = 920, which corresponds to an average air velocity of 1.5 m/s. The mass flow rate of the air is measured to be 1.2±0.1 g/s and 1.3±0.2 g/s at the upstream of the test section and downstream of the WEIT facility, respectively. The results show that there are no major leaks in the test facility and give

confidence to the orifice plate readings because the orifice plate and the air flow measurements at the test section inlet agree within the acceptable uncertainty ranges.

In addition, energy balance tests on the test facility were performed during the heat transfer tests. For the energy balance tests, the test section is assumed as a control volume and the heat produced by the heaters was compared to the heat gained by the air in each test. Conduction losses through the insulation layers account for 15% of the total heat flux produced by the heaters. The difference between the heat gain by the air plus the heat loss and the heat produced by heaters is about 5%.

$$Q_{heater} = VI - Q"_{loss}A\,, \tag{3-15}$$

where Q_{heater} is the corrected heat produced by the heaters [W], V is the voltage of power supply [V], and I is the current of the power supply [A].

Figure 3-2 shows the energy balance results, by comparing the heat production of the heaters and the heat gained by the air for the hollow channel, at five Re.

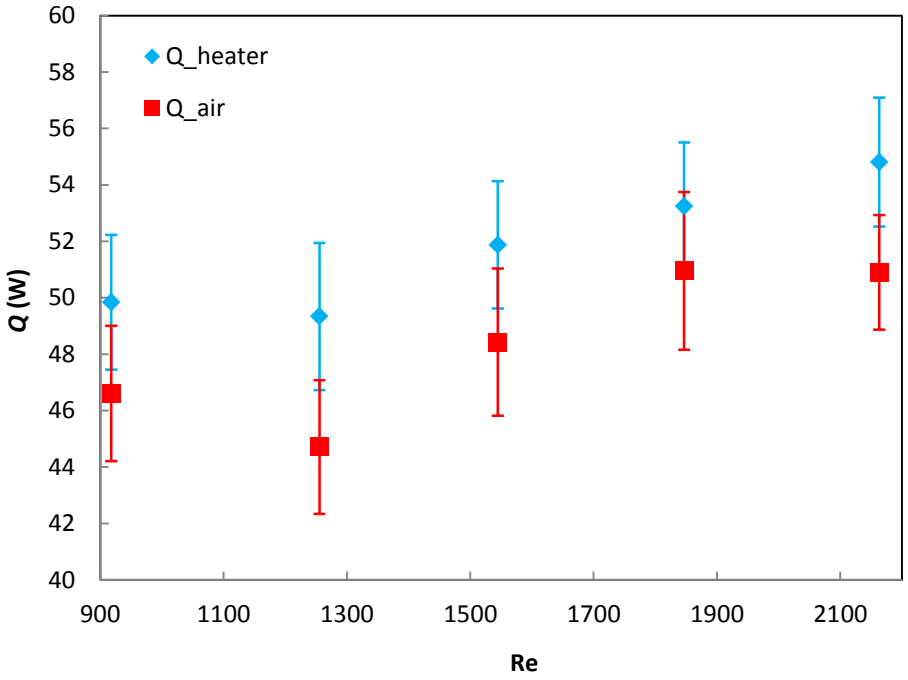

Figure 3-2 Energy balance results of the test section for the hollow channel (without a turbulence enhancing insert) at different Reynolds numbers.

Appendix A.1 shows the test conditions for the energy balance results. Results show that the heat produced by the heaters and the heat gain by the air agree with each other within their experimental uncertainties and confirm that results satisfy the energy balance.

3.5. Experimental data comparison between channel with inserts and hollow channels

All heat transfer tests are conducted in the laminar regime (Re < 2200, based on the calculated Re for the hollow channel). But the hollow channel correlations for the turbulent flow are needed to make a comparison between the heat transfer results of the inserts and the hollow channels. This will be more evident in Chapter 5.

3.5.1. Pumping power (P_{pump})

Defining the Reynolds number for the channel with the turbulence enhancing inserts is complicated. Therefore, the pumping power is defined as a reference parameter to compare the

heat transfer results between the inserts and the hollow channel. The pumping power in each channel is defined based on the volume flow rate and pressure drop inside the channel in equation (3-16).

$$P_{\text{pump}} = AV_{\text{ave}}\Delta P, \tag{3-16}$$

where P_{pump} is the pumping power [W], and A is the cross-sectional area of the channel [m^2].

3.5.2. Correlation for hollow channel

An objective is finding a corresponding average Nusselt number in the hollow channel if the pumping power of the channel with an insert is applied to the hollow channel to make the comparison between the Nusselt number of the channel with the insert and the hollow channel.

$$\left(P_{\text{pump}}\right)_{\text{hollow channel}} = \left(P_{\text{pump}}\right)_{\text{channel with insert}} \tag{3-17}$$

- **Friction factor**

The pressure drop for the hollow channel is a function of Reynolds number. Applying the pumping power of the channel with inserts to the hollow channel may result in laminar or turbulent flow in the hollow channel. Therefore, the friction factor within the hollow channel is calculated from either equation (3-18) or (3-19) [19] which depends on the type of the flow regime in the hollow channel,

$$(f_D)_{\text{lam}} = \frac{96}{\text{Re}}, \tag{3-18}$$

$$(f_D)_{\text{turb}} = (0.79\ln\text{Re} - 1.64)^{-2}, \tag{3-19}$$

where $(f_D)_{\text{lam}}$ is the Darcy friction factor for the laminar flow between infinite parallel plates, and $(f_D)_{\text{turb}}$ is the Darcy friction factor for turbulent flow inside a tube. Equation (3-19) is valid for the fully developed turbulent flow for the Re between 3000 and 5×10^6. Since a Darcy

friction factor correlation for the transition flow ($3000 \leq Re \leq 10^4$) between the smooth parallel plates cannot be found in the literature, equation (3-19) is used to predict the friction factor for the flow between the smooth parallel plates in the transitional regime.

- **Nusselt number**

If the equivalent Re for the hollow channel from equation (3-17) fits in the laminar regime ($Re \leq 2300$), the average Nusselt number for the thermally developing flow between parallel plates (same boundary layer conditions as the test section) is defined in [26, p.181]. Otherwise, the equivalent Nusselt number for the flow with Re of 3000 to 5×10^6 is calculated by equation (3-20) [19],

$$(Nu)_{\text{fully developed}} = \frac{((f_D)_{\text{turb}}/8)(\text{Re}-1000)\,\text{Pr}}{1+12.7((f_D)_{\text{turb}}/8)^{0.5}(\text{Pr}^{2/3}-1)}, \tag{3-20}$$

where $(Nu)_{\text{fully developed}}$ is the fully developed Nusselt number for circular tubes, and *Pr* is the Prandtl of the air which is the ratio of the momentum and thermal diffusivity. The Prandtl number of the air for the experiments with the air temperature ranging from 20°C to 70°C can be assumed constant and equal to 0.7 [19]. Since the air flow within the test section is hydrodynamically fully developed and thermally developing, the average Nusselt number is different from the calculated Nusselt number in equation (3-20). Equation (3-21) [27] gives the correlation to calculate the average Nusselt number according to the boundary layer conditions in the hollow test section,

$$\frac{\overline{Nu}_{\text{eq,hollow}}}{(Nu)_{\text{fully developed}}} = 1 + \frac{C}{(x/D_h)^m}, \tag{3-21}$$

where $\overline{Nu}_{\text{eq,hollow}}$ is the average Nusselt number for the thermally developing flow, and the coefficients C and m are calculated from equations (3-22) and (3-23), respectively.

$$C = 23.99\mathrm{Re}^{-0.23}, \tag{3-22}$$

$$m = -2.08\times10^{-6}\,\mathrm{Re} + 0.815 \tag{3-23}$$

Although the suggested correlations are used to predict *Nu* inside a tube, the experimental *Nu* for hollow channel at Re = 3000 was measured and compared with the predicted value from the correlations (3-20) to (3-23). The difference between the predicted value and experimental value was less than the experimental uncertainty bounds. Therefore, *Nu* for the hollow channel is calculated from correlations for $\mathrm{Re} \geq 3000$.

CHAPTER 4
VALIDATION OF EXPERIMENTAL DATA

4.1. Introduction

Chapter 2 and Chapter 3 describe the experimental facility and methods used to acquire the experimental data. This chapter investigates the validity of the experimental data by comparing the calculated data with the literature for the Nusselt number and friction factor. Also, the sensitivity of the experimental results to the surface heat flux, and the repeatability of the experimental results, are presented.

4.2. Experimental validation

To verify the WEIT facility, this section will compare experimental data with correlations and experimental data in the literature. Comparisons will be done for both the hollow channel (without an insert) and for the channel with an insert.

As mentioned previously, the experiments are in the steady state condition with a constant air temperature and fully developed velocity profile at the entrance of the test section. In the pressure drop tests, the channel walls are unheated and isothermal. The heat measurements in the test section use an average heat flux (Q_{air} /A) of 394 W/m^2 from each heated wall. The ambient air temperature is typically 24°C. The Re (based on the hollow channel hydraulic diameter) within the test section varies from 900 to 2200.

4.2.1. Hollow channel

The friction factor, average Nusselt number and test conditions for the hollow channel tests are presented in Table 4-1.

Table 4-1 Experimental data for the hollow channel.

Re	T_{air} [°C]		$T_{wall,surf}$ [°C]		$\dot{m}$ [g/s]	f_D	$f_D \cdot \mathrm{Re}$	Nu
	Inlet	Outlet	inlet	Outlet				
920	24.1	60.6	42.0	67.9	1.3	0.097±0.012	89±13	9.3±0.6
1260	26.1	51.6	42.9	59.8	1.7	0.072±0.009	91±13	9.2±0.6
1550	24.5	47.0	39.2	56.7	2.1	0.058±0.007	90±12	9.4±0.6
1850	26.4	46.2	41.6	55.9	2.6	0.049±0.012	91±12	9.9±0.7
2160	25.0	41.9	37.8	54.0	3.0	0.042±0.005	92±12	9.9±0.6

The experimental data for the hollow channel are validated with the literature by comparing the average Nusselt number and the friction factor times Reynolds number ($f_D \cdot \mathrm{Re}$) with correlations from the literature. Figure 4-1 presents the measured$f_D \cdot \mathrm{Re}$.The theoretical value of $f_D \cdot \mathrm{Re}$ for hydrodynamically fully developed laminar flow between parallel plates is independent of the Re and equal to 96 [22]. The experimental value of $f_D \cdot \mathrm{Re}$ is also nearly constant with Re which verifies that the flow is fully developed laminar flow in the test section. It should be noted the experimental *Nu* is slightly higher than the theoretical value (Figure 4-2). However, the theoretical and experimental values agree within experimental uncertainty. The difference of the experimental and theoretical *Nu* may be due to the sidewalls of the rectangular channel in the experiment and assuming the test section is infinite parallel plates.

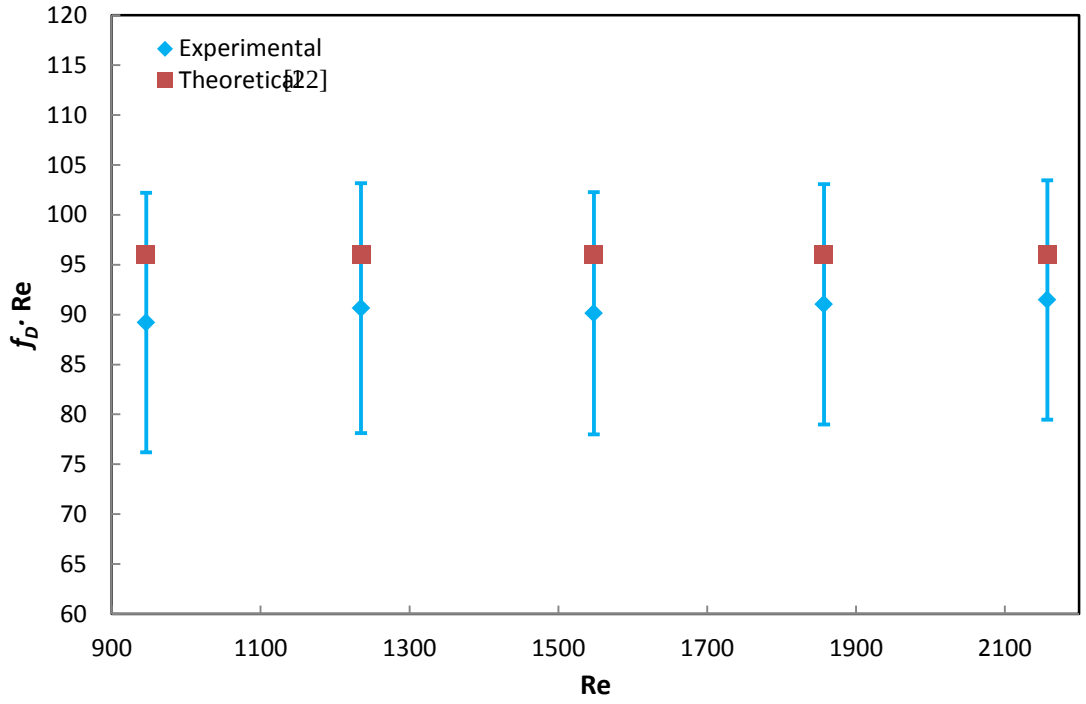

Figure 4-1 Comparison of experimental $f_D \cdot \mathrm{Re}$ and theoretical correlation for the hollow channel. The error bars represent the 95% uncertainty bounds for the experimental data.

Figure 4-2 presents the experimental and theoretical values of *Nu* within the hollow channel as a function of Re. Both experimental and theoretical Nusselt numbers increase as a function of Re. The theoretical value of *Nu* is for hydrodynamically fully developed and thermally developing flow between the parallel plates [26, p.181]. The results in Figure 4-2 show that the experimental *Nu* values agree with the theoretical *Nu* values within experimental uncertainties for all Re. The results verify that the WEIT facility calculated data for *Nu* and $f_D \cdot \mathrm{Re}$ agree with the literature within the uncertainty bounds of the experiment for the test section.

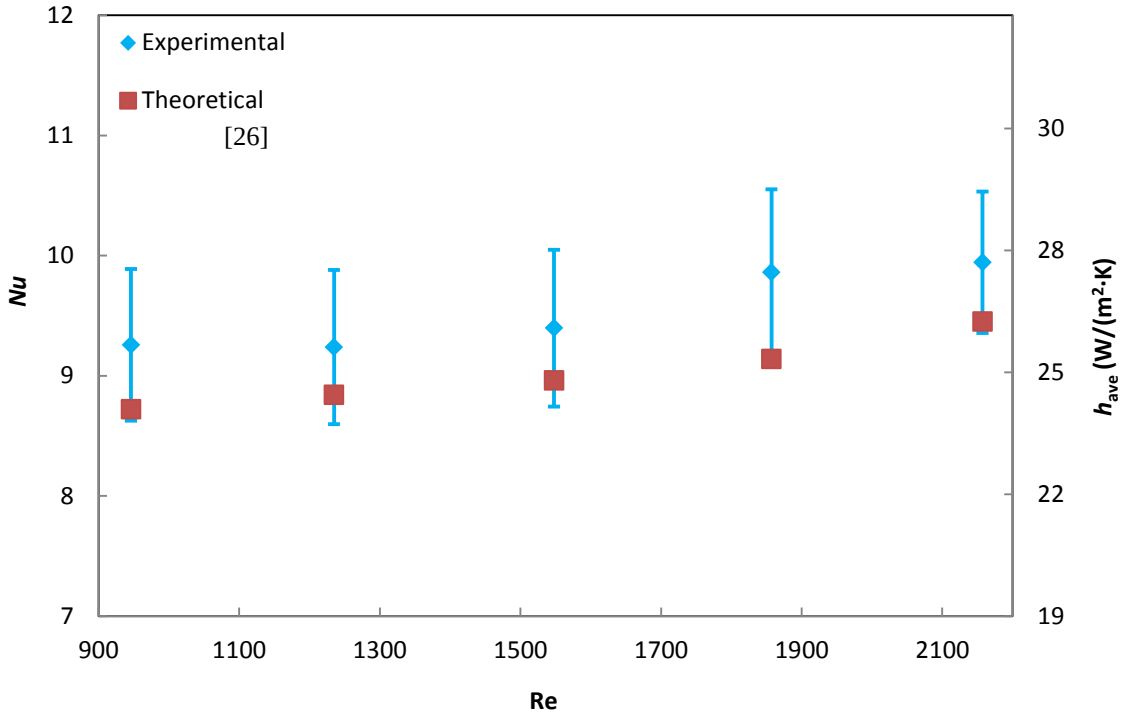

Figure 4-2 Comparison between experimental and theoretical *Nu* for the hollow channel. The error bars represent the 95% uncertainty bounds for the experimental data.

4.2.2. Channel with inserts

The most similar available work in the literature was conducted by Vujisic [6]. Vujisic [6] measured the average Nusselt number across the cylindrical bars (eddy promoters) in a 2.5-cm-wide (W) rectangular channel (Figure 4-3). The diameter (D) of the bars was0.772 cm (D/W = 0.309). The bars were centered on the flow channel centerline and normal to the flow direction with periods of 19.4 cm (S/W = 7.76). Vujisic [6] did the measurements with a constant heat flux on one side wall and the other wall was completely insulated. Figure 4-3 shows the dimensions of the test section and geometry of the eddy promoters that Vujisic [6] used in his experiments [6].

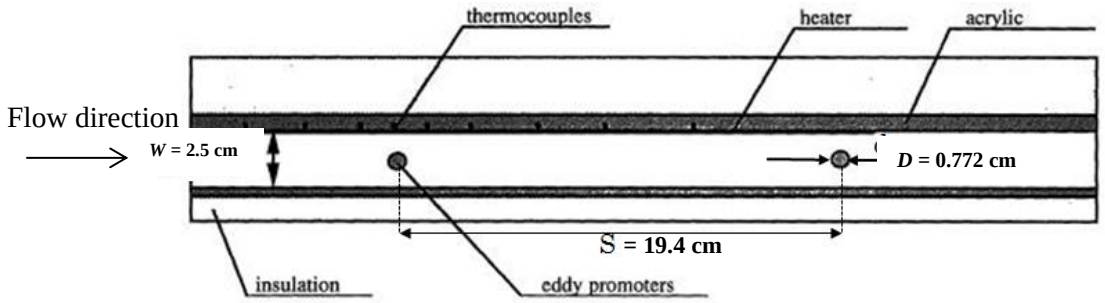

Figure 4-3 Top view of the test section available in the literature [6].

Cylindrical bars with a diameter of 1.6 mm and a spacing of 38.8 mm between the bars are employed within the test section of the WEIT facility (D/W = 1.6/5 = 0.32 and the S/W = 38.8/5 = 7.76 in the WEIT facility) to repeat the experimental tests of Vujisic [6] in the WEIT facility. Also, one of the heaters in the side wall of the WEIT facility was turned off to provide one heated side wall with constant heat flux. Figure 4-4 compares the measured Nusselt numbers within the WEIT facility and the available Nusselt numbers in literature [6] as a function of Re. Vujisic [6] reports the uncertainty of ±11% in the average Nusselt number and this is included in Figure 4-4. The *Nu* data from the WEIT facility agree with the data measured by Vujisic [6] within the experimental uncertainty bounds.

The data in the literature have a higher uncertainty than the measured averaged Nusselt number by the WEIT facility. Vujisic [6] calculated the average Nusselt number by measuring the local Nusselt numbers within the test section. Since the uncertainty of the local Nusselt number is normally higher, the reported average Nusselt number has a higher uncertainty than the Nusselt number in the WEIT facility. The different methods of the average Nusselt number calculation cause the difference between the Nusselt number in the literature and the experimental value [6].

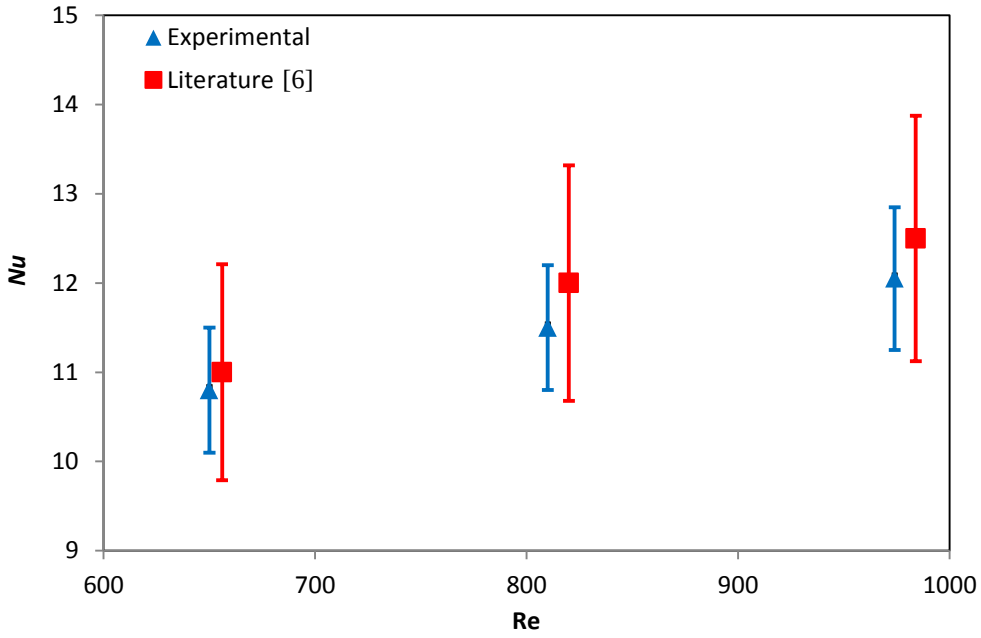

Figure 4-4 Comparison of *Nu* measured in the WEIT facility with *Nu* measured by Vujisic [6]. The tests are for the case of constant heat flux on one wall only.

4.3. Effect of heat flux on *Nu*

The Nusselt number is expected to be independent of surface heat flux. The effect of the surface heat flux is investigated by conducting three experiments for the B30R20 configuration with three different heat fluxes on the side walls of the test section at the mass flow rate of 3.0 ± 0.1 g/s (Re ≈ 2150). The constant heat fluxes were 346 W/m^2, 450 W/m^2, and 587 W/m^2 (heat flux = Q_{air}/A). The experimental data for these three experiments are tabulated in Table 4-2 and presented in Figure 4-5.

Table 4-2 *Nu* for B30R20 with three different heat fluxes on the side walls.

Q_{air}/A [W/m^2]	Re	T_{air} [°C]		$T_{wall,surf}$ [°C]		Q_{heater} [W]	Q_{air} [W]	$\frac{Q_{air}}{Q_{heater}}$ [%]	*Nu*
		Inlet	Outlet	inlet	outlet				
346	2170	24.9	42.3	32.8	44.5	55±2	53±2	96	28.5±2.0
450	2150	25.0	47.8	35.5	50.5	73±3	69±3	94	28.7±2.3
587	2170	24.9	54.7	38.0	58.5	96±4	89±4	94	28.3±1.9

The experimental data show that the measured Nusselt numbers are essentially constant. Therefore, changing the surface heat flux does not change the average Nusselt number. It only changes the measured wall surface temperatures and the outlet bulk air temperature (shown in Table 4-2). The results confirm that the measured *Nu* is independent of the heat flux from the side walls.

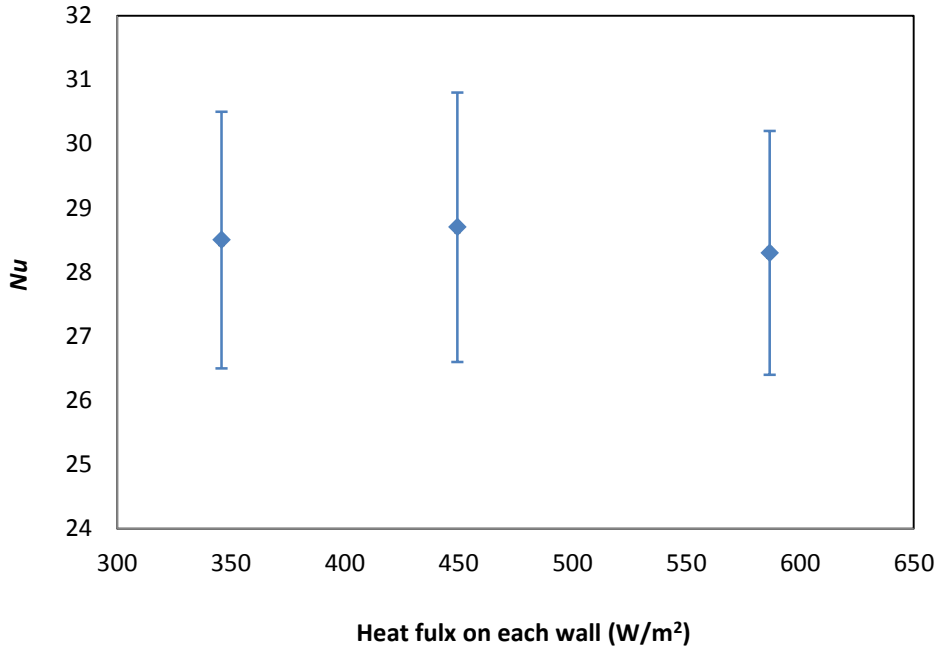

Figure 4-5 *Nu* for B30R20 at Re = 2150 with three different heat fluxes (Q_{air}/A) on the side walls.

4.4. Repeatability

The heat transfer test is repeated three times for insert B60R20 at three different Re to identify the repeatability of the measured global Nusselt number. In the first test (identified as case 1 in Table 4-3 and Figure 4-6), the Nusselt number was measured at three Re and then all the equipment was shut down. The second test (Case 2) was conducted the next day. In the third test (Case 3), the equipment was shut down and removable walls of the test section containing the heaters and thermocouples were removed and reassembled before the

experiments were repeated. The test conditions and results of these tests are presented in Table 4-3 and Figure 4-6.

Table 4-3 Repeatability of the experimental data of B60R20.

	Re	T_{air} [°C]		$T_{wall,surf}$ [°C]		Q_{heater} [W]	Q_{air} [W]	$\frac{Q_{air}}{Q_{heater}}$ [%]	Nu
		inlet	Outlet	inlet	Outlet				
Case 1	930	25.3	59.6	38.1	62.6	47±2	44±1	94	14.8±0.8
	550	24.9	48.7	34.8	51.6	54±2	51±2	94	20.5±1.3
	2170	25.7	42.9	33.7	46.1	57±2	53±2	93	24.1±1.5
Case 2	930	23.6	58.3	37.5	61.1	48±2	45±2	94	14.8±0.8
	1540	24.8	48.3	33.5	51.4	55±2	51±2	93	20.3±1.3
	2160	24.5	42.1	33.4	45.0	56±2	53±2	95	24.2±1.5
Case 3	920	25.5	59.2	39.1	62.1	45±2	43±1	96	14.9±0.8
	1560	25.6	49.4	36.3	52.3	56±2	52±2	93	20.5±1.2
	2180	25.6	42.8	34.4	45.6	56±2	52±2	93	24.0±1.5

Table 4-3 and Figure 4-6 show that the repeated tests agree well within the total uncertainty bounds (bias and precision) determined in Chapter 3. Therefore, the repeatability has a negligible impact on the overall uncertainty on the measured *Nu*. Hence, all the data presented in this thesis will be based on the single measurement rather than repeated measurements.

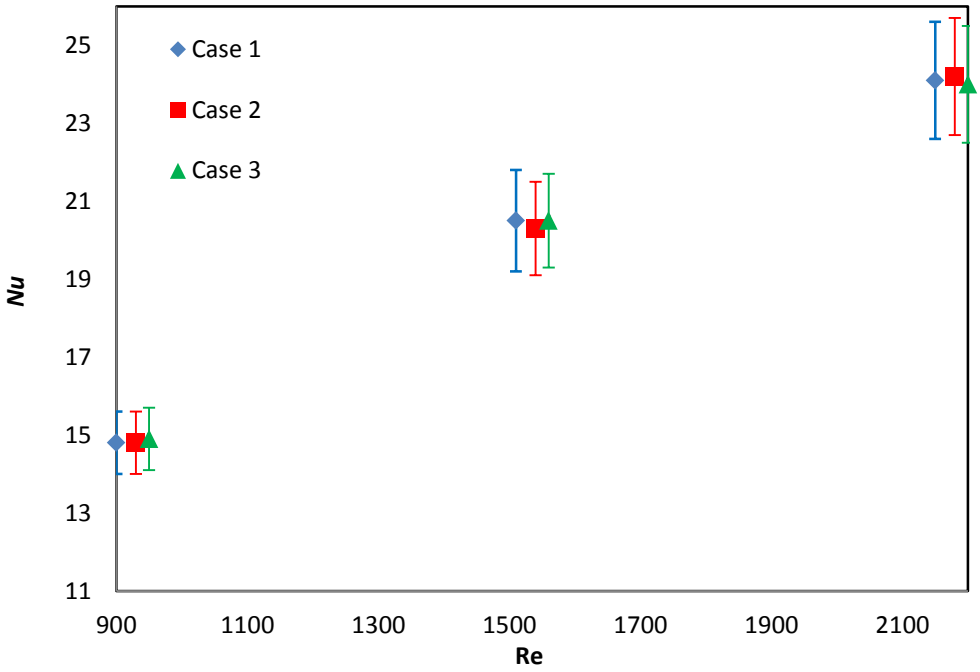

Figure 4-6 Repeatability of the measured *Nu* for B60R20.

CHAPTER 5

MEASURED NUSSELT NUMBERS AND FRICTION FACTORS

5.1. Introduction

This chapter presents the measured Nusselt numbers and friction factors for nine different inserts at Re between 900 and 2200 and compares these data with experimental data for the hollow channel (no inserts).

5.2. Nusselt number (Nu) and Darcy friction factor (f_D)

The test conditions for each test and the calculated Nu and f_D are presented in Appendix A.2. Figure 5-1 to Figure 5-4 present the calculated Nu and f_D for the channel with and without inserts as a function of Re. These figures show that the inserts increase both the convective heat transfer and pressure drop compared to the hollow channel. The inserts enhance the convective heat transfer by creating eddies in the airflow and mixing the air near the walls. As a result, wall shear stress and dimensionless temperature gradient at the wall increase, which increases the pressure drop (surface drag) and heat transfer compared to the hollow channel. The inserts also block part of the channel, which creates a form or pressure drag that does not exist in the hollow channel, and this results in higher pressure drop in the channel with the inserts compared to the empty hollow channel.

Figure 5-1 presents Nu and f_D for inserts B30R20 and B30R30 compared to the hollow channel.

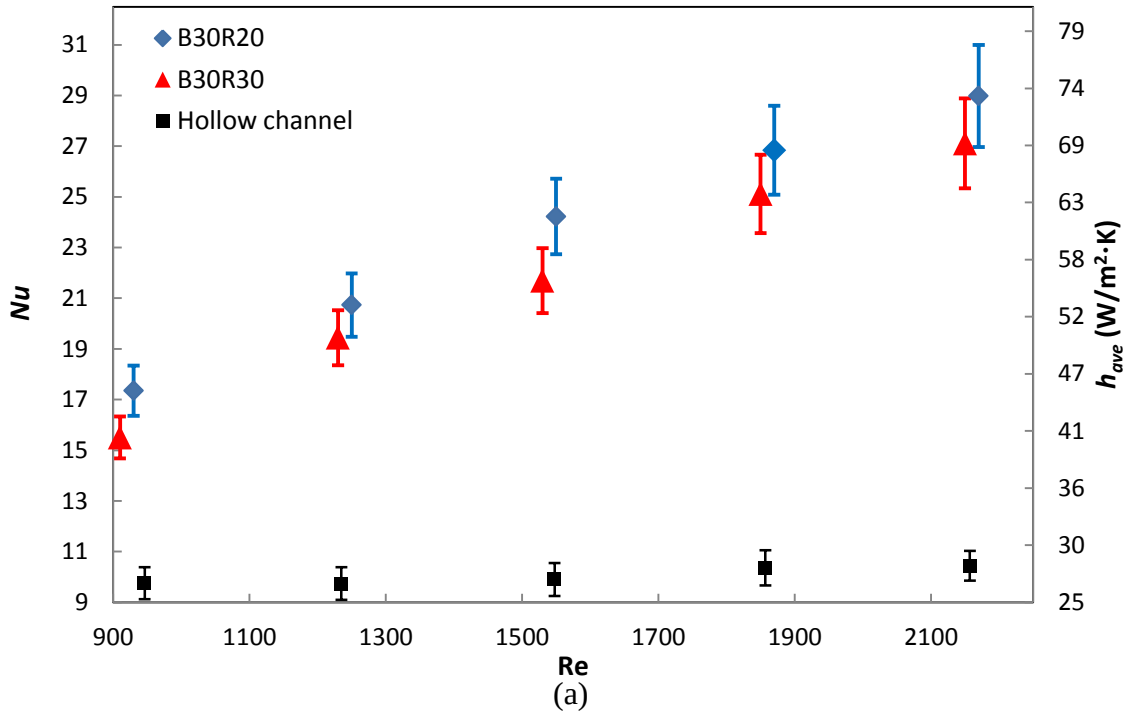

(a)

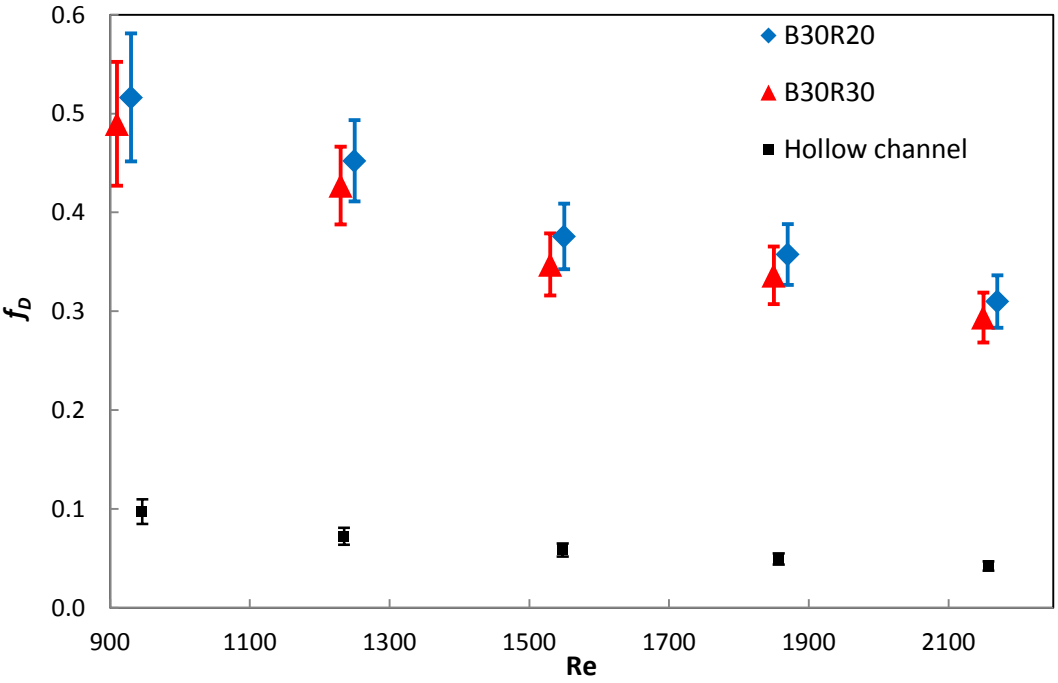

(b)

Figure 5-1 (a) Experimental Nusselt number and (b) Darcy friction factor for B30R20 and B30R30.

Figure 5-1 shows that *Nu* increases with Re and f_D decreases with Re which is expected from the literature for flow through channels and around bluff bodies [6], [17], [19].

The results for B30R20 and B30R30 show that the closer spacing of the ribs causes better mixing of the air which results in the higher Nusselt number. B30R20 and B30R30 have the same spacing for cylindrical bars but the plastic ribs have different spacing. It should be noted that the Nusselt number and friction factor are similar for both cases but B30R20 has a slightly higher *Nu* and f_D compared to B30R30 insert. Although Incropera et al. [19] shows *Nu* is higher for parallel plates than rectangular channel, the cut outs in the plastic ribs (Figure 2-2) play a role and enhance the disturbances in the flow for B30R20 compared to B30R30 insert. This effect appears to lie within the experimental uncertainty in figures below.

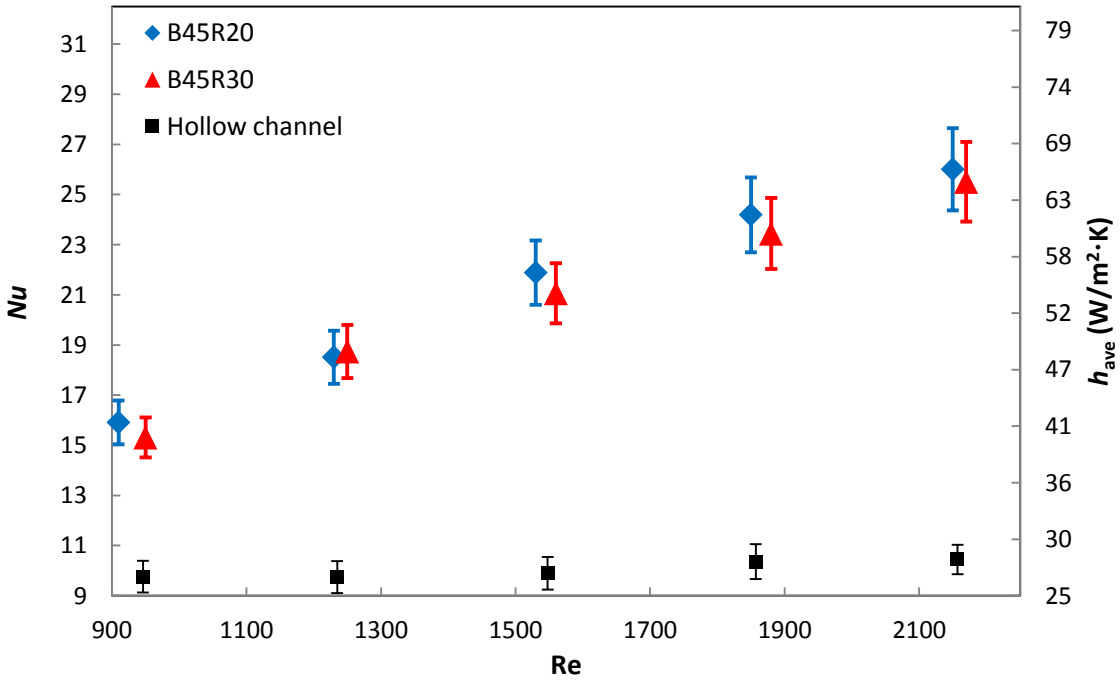

(a)

Figure 5-2 (a) Experimental Nusselt number for B45R20 and B45R30.

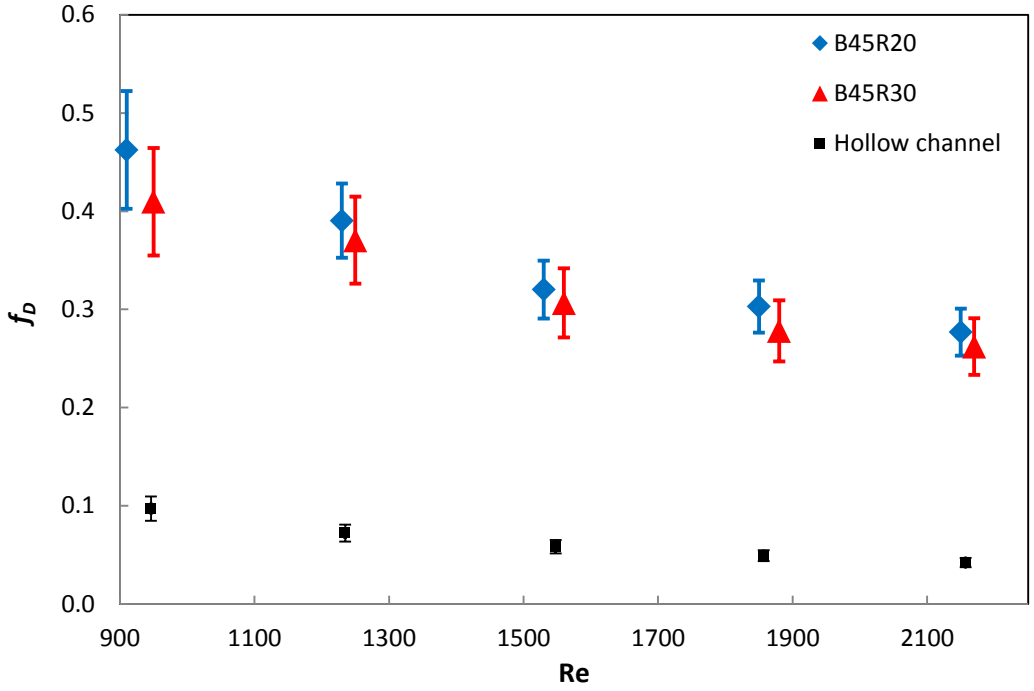

(b)

Figure 5-2 Continued- (b) Darcy friction factor for B45R20 and B45R30.

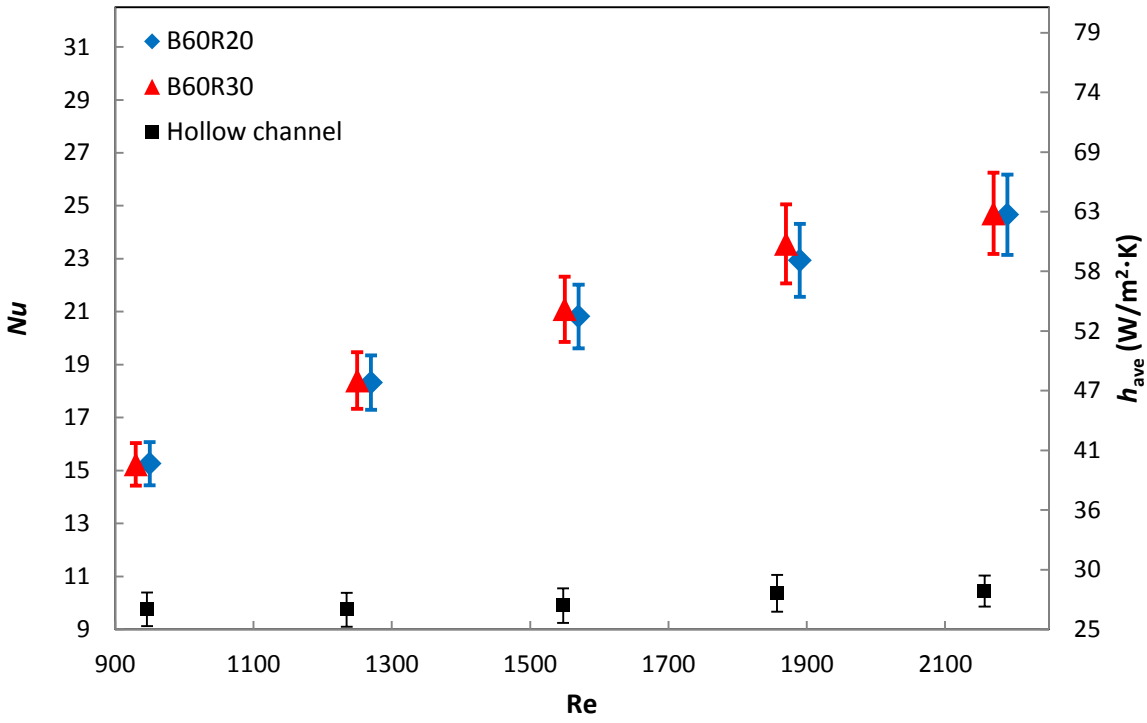

(a)

Figure 5-3 (a) Experimental Nusselt number for B60R20 and B60R30.

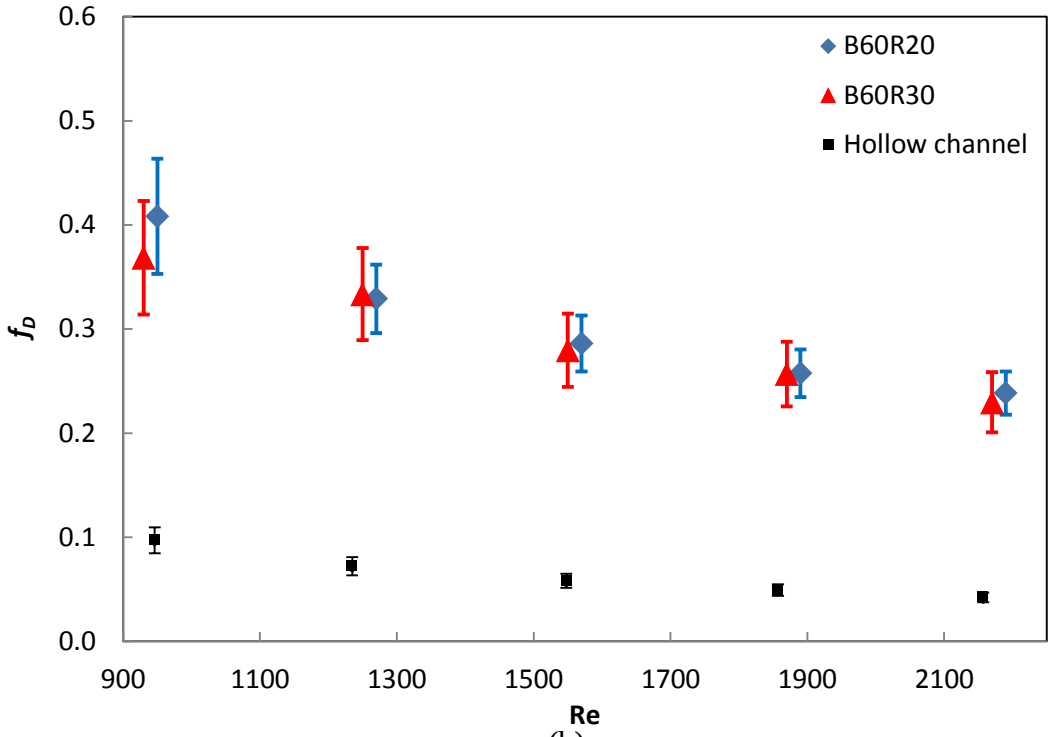

(b)

Figure 5-3 continued (b) Darcy friction factor for B60R20 and B60R30.

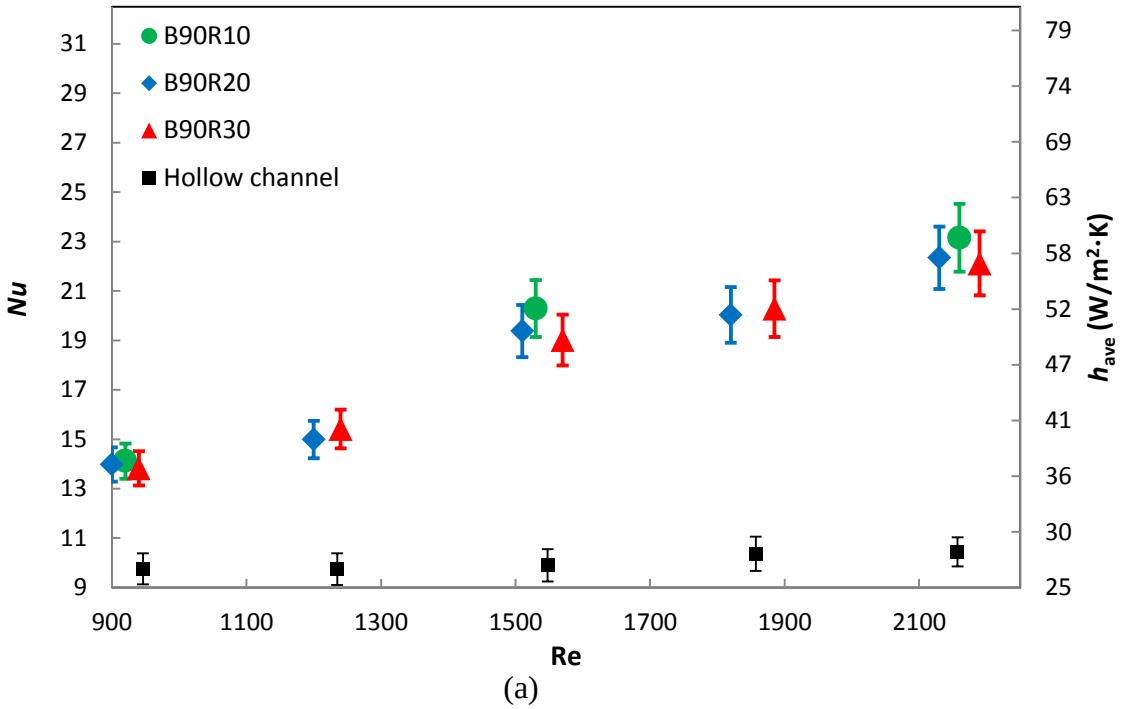

(a)

Figure 5-4 (a) Experimental Nusselt number for B90R10, B90R20, and B90R30.

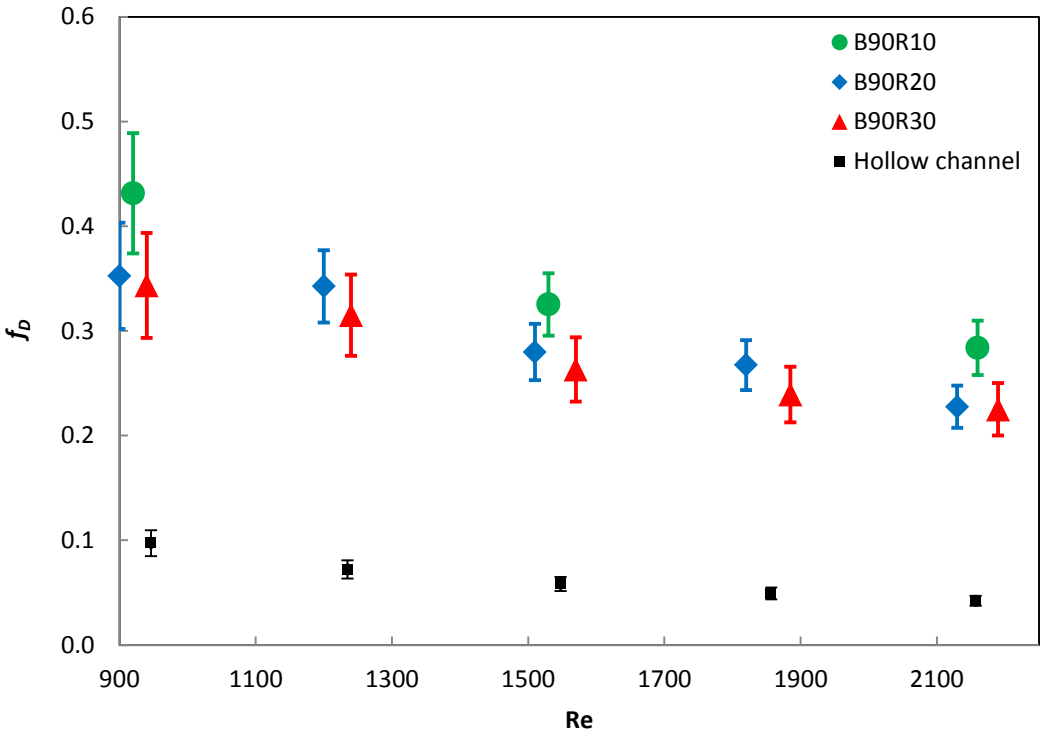

(b)

Figure 5-4 continued (b) Darcy friction factor for B90R10, B90R20, and B90R30.

The experimental data for B30R20 and B30R30 in Figure 5-1 show that the B30R20 has a higher *Nu* than B30R30. On the other hand, the friction factor of B30R20 is close to B30R30. The experimental data of the other inserts show that the difference of the *Nu* and f_D of two inserts with same cylindrical bars spacing and different plastic ribs spacing is less than 5% (i.e. comparing the *Nu* and f_D of B45R20 and B45R30 in Figure 5-2 shows that both inserts have a similar *Nu* and f_D within the experimental uncertainty bounds).

The effect of the cylindrical bars spacing on the Nusselt number and Darcy friction factor is shown in Figure 5-5. The spacing of the plastic ribs is 20 mm and the cylindrical bars spacing is either 30 mm, 45 mm, 60 mm, or 90 mm. Comparing the experimental data in Figure 5-5 shows that changing the cylindrical bars spacing is more effective on *Nu* at higher Re. For instance, the *Nu* of B30R20, B45R20, B60R20, and B90R20 is close to each other at

Re = 900. But the difference between the *Nu* increases as Re is increased. In other words, creation and dissipation of eddies by the cylindrical bars has more effect at higher Re, since the closer cylindrical bars causes the better air mixing and more eddy creation.

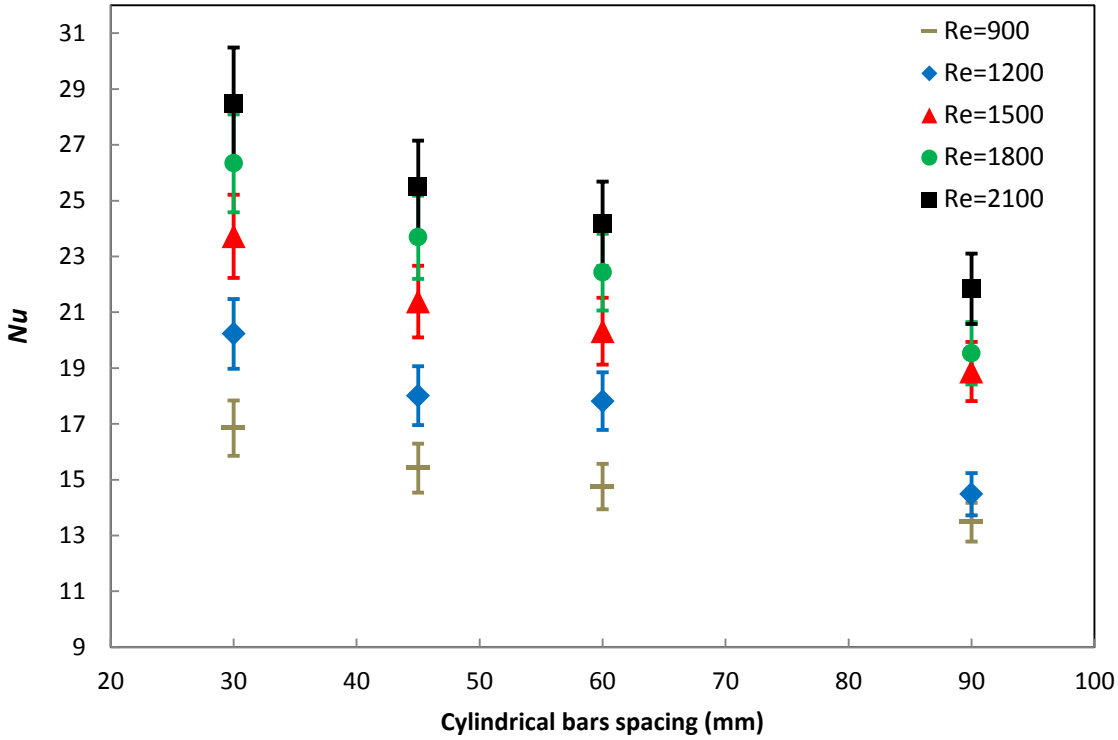

(a)

Figure 5-5 Effect of the cylindrical bars spacing on (a) *Nu* (b) f_D.

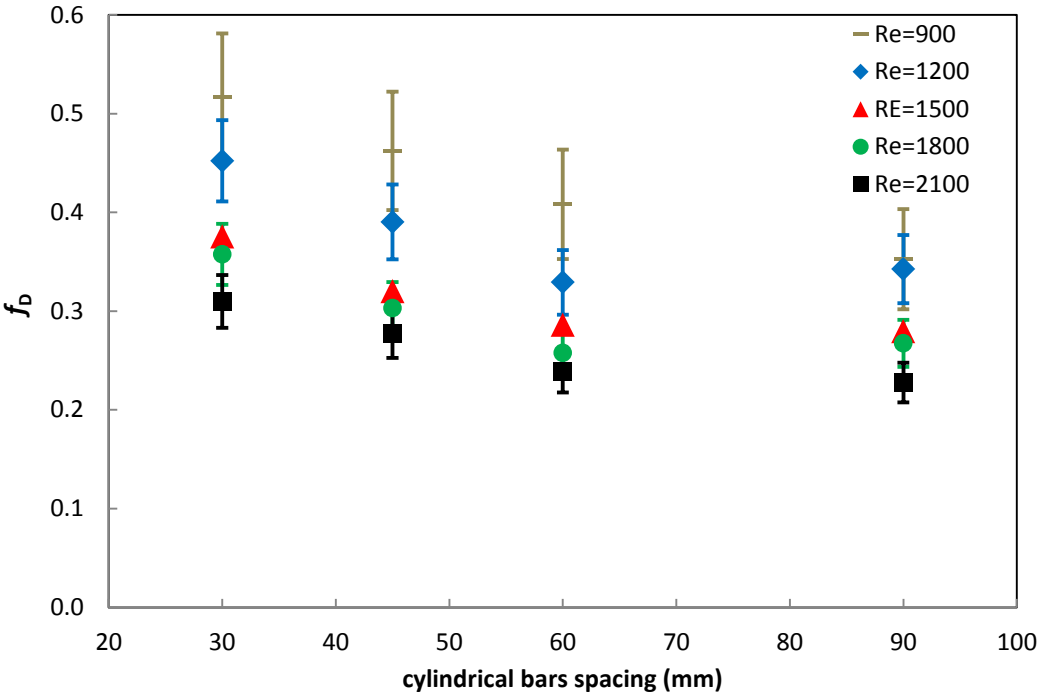

(b)

Figure 5-5 continued- Effect of the Cylindrical bars spacing on (a) Nu (b) f_D.

The pressure drop results in Figure 5-5 (b) show that the closer spacing of the cylindrical bars cases higher pressure drop in the air flow within the test section, since the closer spacing of the bars causes higher skin friction and pressure drag in the channel.

5.3. Enhancement in heat transfer

The effect of the turbulence enhancing inserts on the convective heat transfer coefficient can be identified by comparing the measured Nusselt number in the channel with inserts and the channel without inserts (hollow channel). The inserts increase the Nusselt number with the cost of higher pressure drop within the channel. Therefore, to investigate the effect of the inserts on the heat flux enhancement both the Nusselt number and friction factor are considered and compared with the hollow channel values. The Nusselt number and friction

factor for the inserts are compared to the Nusselt number and friction factor for the hollow channel at the same Reynolds number in Figure 5-6 (a) and Figure 5-6 (b), respectively.

$$Nu_{\mathrm{Re}}^{*} = \frac{Nu}{Nu_{\mathrm{exp,hollow}}}, \tag{5-1}$$

$$f^{*} = \frac{f_D}{(f_D)_{\mathrm{exp,hollow}}} \tag{5-2}$$

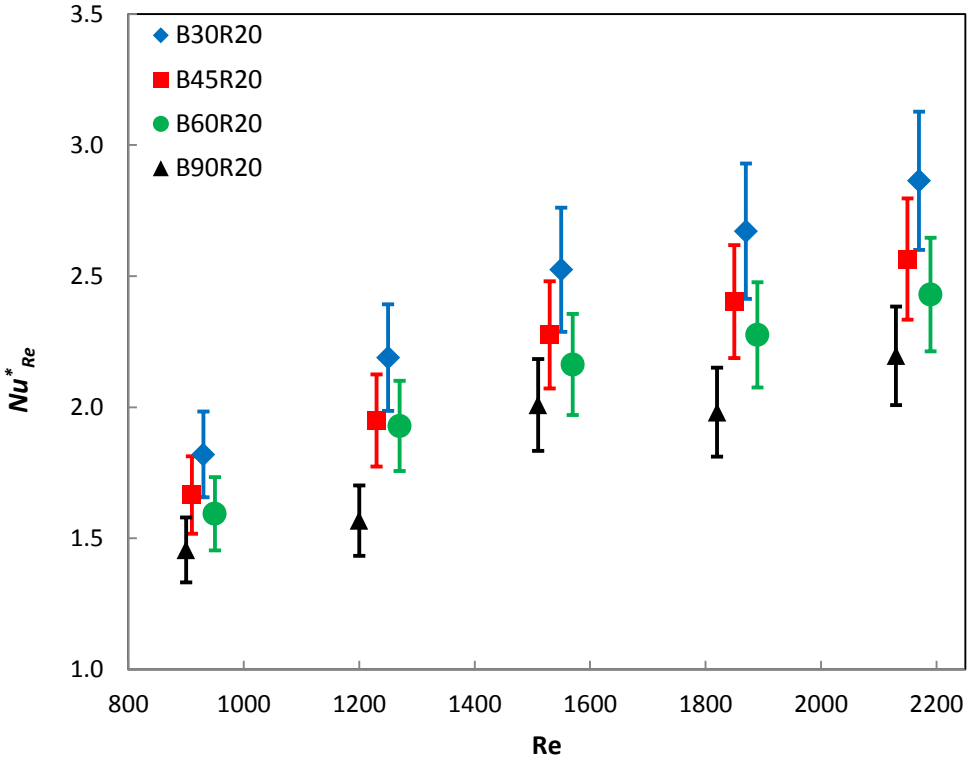

(a)

Figure 5-6 Comparison of the Nu and f_D between the channel with inserts and hollow channel (a) Nu_{Re}^{*}, (b) f^{*}.

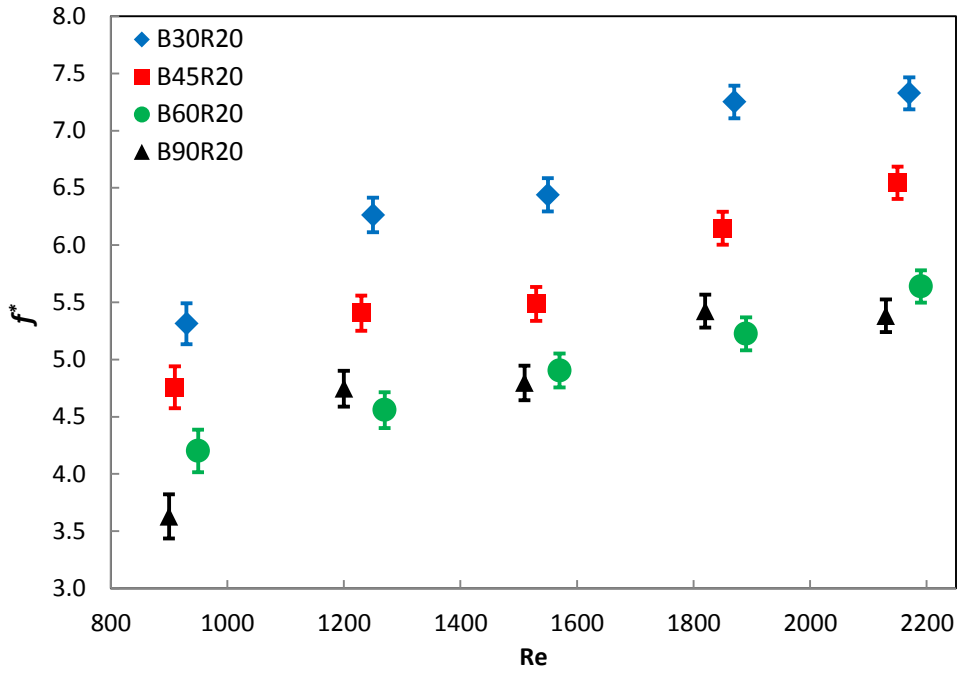

(b)

Figure 5-6 Continued - Comparison of the *Nu* and f_D between the channel with inserts and hollow channel (a) Nu^*_{Re}, (b) f^*.

Since the results in Section 5.2 show that *Nu* and f_D change within the experimental uncertainty bounds when the ribs spacing changes from 20 mm to 30 mm, this section investigates the effect of the cylindrical bars spacing on heat flux enhancement. Figure 5-6 presents the results for the inserts with ribs spacing of 20 mm and the cylindrical bars spacing of 30 mm, 45 mm, 60 mm, and 90 mm. Figure 5-6 shows that decreasing the spacing of cylindrical bars increases the *Nu* due to the better air mixing and larger enhancement in heat transfer. As an example, the results show that B30R20 enhances *Nu* by 190 percent compared to the hollow channel at Re of 2170. On the other hand, the friction factor increases by a factor of 7 at the same Re. This means that the inserts give the benefit of enhanced heat transfer, but at the cost of an increase in the pressure drop through the channel.

Comparing the Nu^*_{Re} for B45R20 and B60R20 in Figure 5-6 (a) shows that both inserts have almost same Nu^*_{Re} for the Re lower than 1500, but B45R20 has a higher Nu^*_{Re} at Re of

1530, 1870, and 2170. However, f^* for B45R20 is 60% to 90% higher than B60R20 for Re between 900 and 2180. Therefore, comparing the inserts would be complicated when considering the *Nu* and f_D separately.

The other way to compare the heat transfer enhancement by inserts is calculating the Nu_P^* when the channel with inserts and the hollow channel have a same friction factor (pumping power).

$$Nu_P^* = \frac{Nu}{\overline{Nu}_{\text{eq,hollow}}} \tag{5-3}$$

To calculate $\overline{Nu}_{\text{eq,hollow}}$ in Nu_P^*, the pumping power of the channel with an insert is calculated and the same pumping power is applied to the hollow channel and the equivalent Re in the hollow channel is obtained (Equations (3-18) and (3-19)). Then the $\overline{Nu}_{\text{eq,hollow}}$ is calculated from either the Ref. [26] or equations (3-20) and (3-21) , which depends on the flow regime in the hollow channel. According to the test conditions for the channel with inserts in Appendix A.2, the equivalent Re and $\overline{Nu}_{\text{eq,hollow}}$ for the hollow channel in each test is calculated and presented in Appendix A.3.

The Nu_P^* for the inserts is shown in Figure 5-7 as a function of pumping power and equivalent Re in the hollow channel. The results in Figure 5-7 show that the ratio of Nu^* increases as a function of pumping power and then decreases. The equivalent Re in the hollow channel (Appendix A.3) for each insert at Re of 930 and 1230 is lower than 3000 which is located in the laminar or transitional regime and Nu_P^* is larger compared to the other Re. In other words, the inserts are more effective at the laminar and transition regimes with respect to the turbulent regime and the enhancement in the heat transfer is higher in the laminar and transition regimes [3].

Comparing the spacing of the plastic ribs in Figure 5-7 shows that changing the ribs spacing while the intervals of the cylindrical bars are same, the enhancement in the convective heat transfer would be the same.

The experimental results confirm that the same convective heat transfer coefficient as the hollow channel can be reached by the presence of the turbulence enhancing inserts within the channel, while the channel with inserts runs at lower pumping power. As an illustration, the average Nusselt number for the hollow channel at the Re = 4000 is 15.7 ± 1.3 which can be enhanced by employing B45R20 within the channel at Re = 930. The pumping power for the hollow channel at Re = 4000 is 0.14 W while the pumping power for the B45R20 at Re = 930 is 0.03 W. In other words, the pumping power of B45R20 at Re = 930 is 4.7 times smaller than the hollow channel at Reynolds number of 4000.

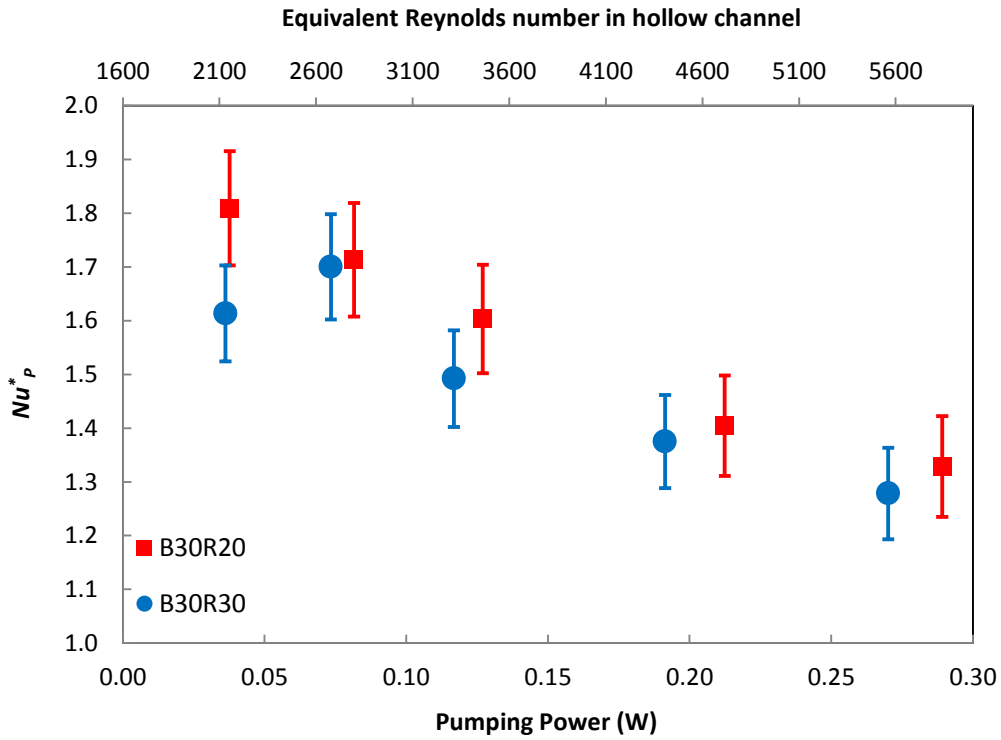

(a)

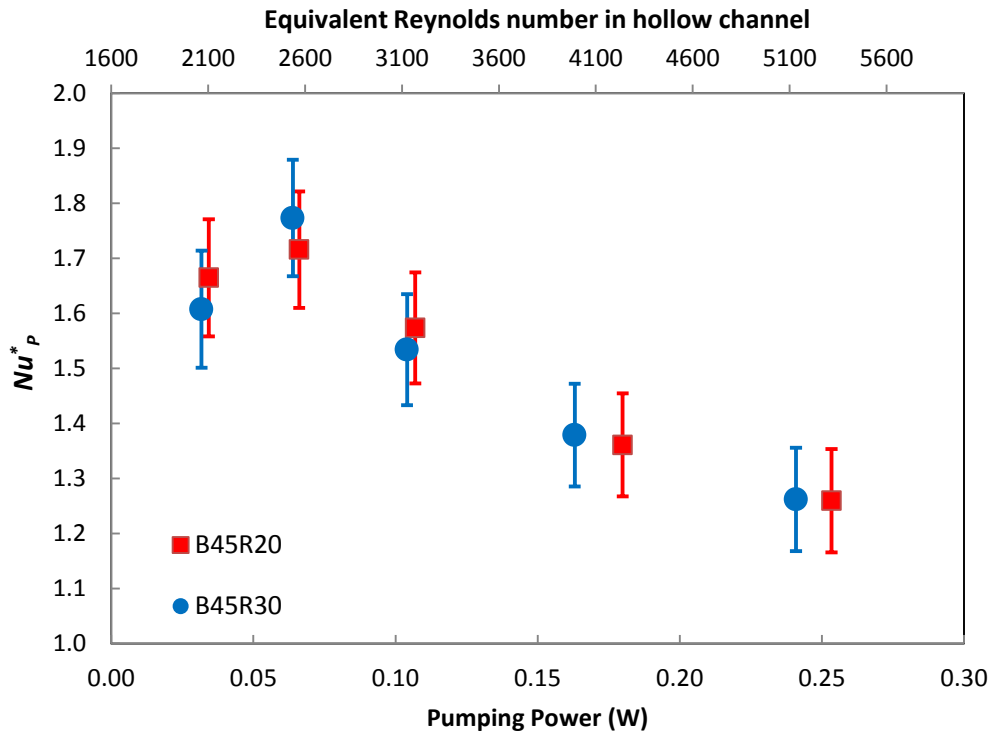

(b)

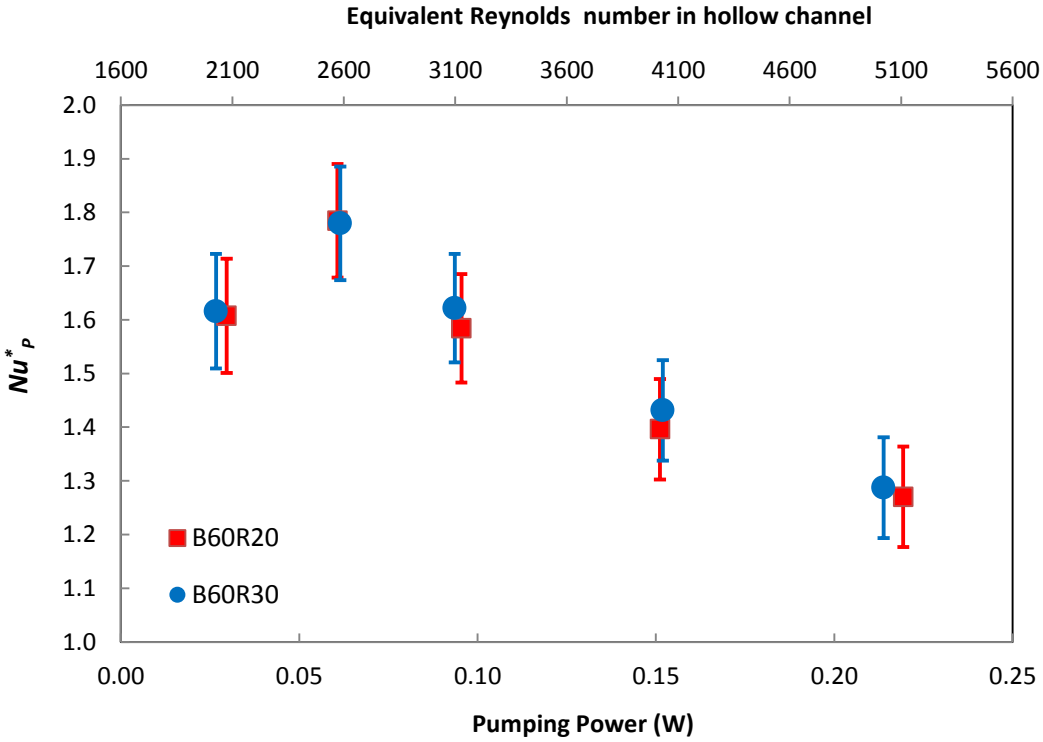

(c)

Figure 5-7 Heat transfer enhancement for (a) B30R20 and B30R30, (b) B45R20 and B45R30, (c) B60R20 and B60R30, and (d) B90R10, B90R20, and B90R30.

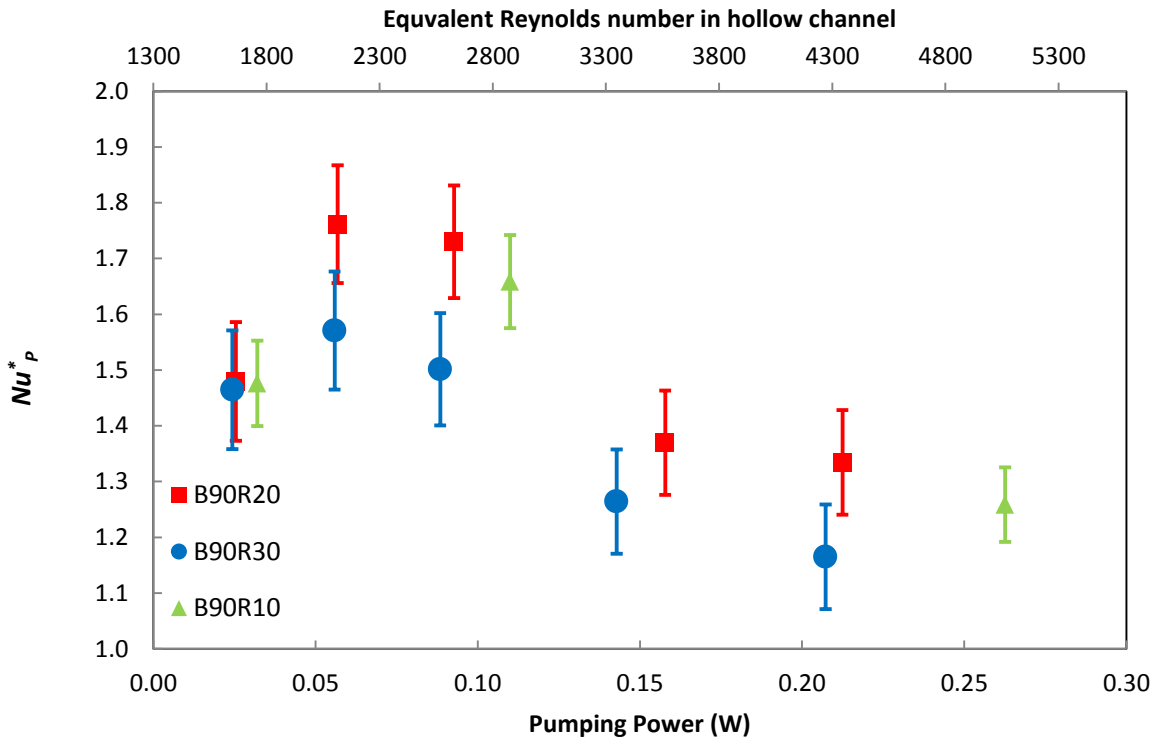

(d)

Figure 5-7 continued - Heat transfer enhancement for (a) B30R20 and B30R30, (b) B45R20 and B45R30, (c) B60R20 and B60R30, and (d) B90R10, B90R20, and B90R30.

CHAPTER 6
EMPIRICAL CORRELATIONS

6.1. Introduction

The objective of this chapter is to develop correlations that express *Nu* and f_D as a function of Re and the important dimensionless geometry ratio for the inserts. The experimental results in Chapter 5 show that *Nu* and f_D depend on the insert geometry and the air flow Re. The rib spacing changes the Nusselt number and friction factor within the uncertainty of the measurements especially when the cylindrical interval is 45, 60, or 90 mm. Therefore, the empirical correlations of Nusselt number and friction factor are defined in terms of cylindrical bar intervals and the air flow Reynolds number.

Developing correlations for *Nu* and f_D is divided into three stages. In the first stage, two models are proposed for each insert, one to represent *Nu* and one to represent f_D as a function of Re. Parameters of these correlations are estimated by fitting them to the experimental data for each insert. The values of estimated parameters are dependent on the geometry of the inserts.

In the second stage, a correlation is proposed to express each of the parameters in the first stage as a function of the geometry of the inserts. Therefore, the final form of the correlations express *Nu* and f_D as a function of both Re and the geometry of the inserts.

In the final stage, all the experimental data (except B90R10) were pooled together to estimate the parameters of the second stage.

6.2. Nusselt number correlation

Most of the *Nu* correlations in the literature for channels with fins or inserts are of the form:

$$Nu = a * \mathrm{Re}^{b}, \quad (6\text{-}1)$$

where a and b are fitting coefficients. However, the following linear correlation provides better fits for the experimental data in this thesis over the Re range from 900 to 2200:

$$Nu = a_1 * \mathrm{Re} + b_1 \quad (6\text{-}2)$$

The coefficients of the correlation and their uncertainties are calculated for the constant cylindrical bars intervals of 30 mm, 45 mm, 60 mm, and 90 mm based on the maximum likelihood method [28] and these are presented in Table 6-1.

Table 6-1 Coefficients in empirical correlation $Nu = a_1 * \mathrm{Re} + b_1$ for constant cylindrical bars intervals.

Inserts used to determine coefficients	a_1	σ_{a_1}/a_1 [%]	b_1	σ_{b_1}/b_1 [%]
B30R20 B30R30	0.0098	4.8	7.0	9.6
B45R20 B45R30	0.0085	5.0	7.4	8.6
B60R20 B60R30	0.0080	5.3	7.6	8.1
B90R20 B90R30	0.0070	5.3	6.8	8.0

It should be noted that the data for insert B90R10 are not used to develop the correlation, but will be used to test the correlation later in this section. The results in Figure 6-1 show that increasing the spacing of the cylindrical bars decreases the coefficient a_1. It should be noted that decreasing a_1 means decreasing *Nu*. Also, Figure 6-1 shows that the coefficient b_1

is nearly constant within their uncertainties as the cylindrical bars intervals changes. Therefore, it is assumed that the coefficient a_1 is dependent on the spacing between the cylindrical bars and the coefficient b_1 is independent of the geometry of the inserts. The coefficient a_1 is plotted as a function of the spacing between the cylindrical bars in Figure 6-1 to identify the relationship between the coefficient a_1 and the *W*/H (*W* is the bars width, and H is distance between the cylindrical bars).

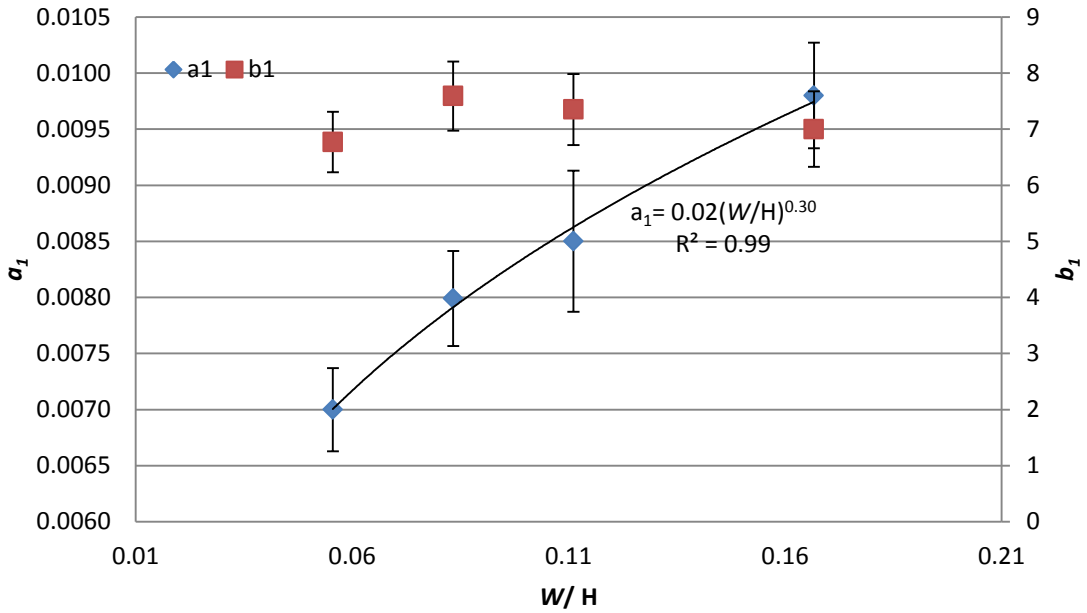

Figure 6-1 Relation of coefficient a_1 and b_1 with *W*/H.

The function between coefficient a_1 and (*W*/H) is found by curve fitting to data in Table 6-1 and the best fit is found by the tools in Excel and minimizing the root-mean-square error. Figure 6-1 indicates that the coefficient a_1 in the correlation of *Nu* has the power relation with *W*/H. Based on the data in Table 6-1 and Figure 6-1 a general correlation in the form of equation (6-3) is proposed for prediction of *Nu* in terms of spacing between cylindrical bars and air flow Reynolds number.

$$Nu = A(\frac{W}{\mathrm{H}})^{B}\,\mathrm{Re} + C \tag{6-3}$$

The empirical correlation shows that the inserts with a larger cylindrical bar spacing has a smaller average Nusselt number. Also, the inserts result in higher Nusselt number at higher Reynolds number. The correlation confirms the fact that the inserts with very large cylindrical bars intervals or inserts at very low Reynolds number do not provide much enhancement and the Nusselt number is close to the hollow channel Nusselt number.

The "leave one out" cross validation method [29] is used to verify how the general correlation predicts some experimental data when those experimental data are excluded in finding the coefficients of the correlation. Table 6-2 shows the coefficients of the correlation when each set of data is excluded in determination of coefficients.

Table 6-2 Determination of coefficient of $Nu = A(\frac{W}{\mathrm{H}})^{B}\,\mathrm{Re} + C$.

Inserts used to determine coefficients	A	σ_A/A [%]	B	σ_B/B [%]	C	σ_C/C [%]
All inserts Without B30R20 & B30R30	0.020	13	0.36	9	7.2	5
All inserts Without B45R20 & B45R30	0.017	7	0.31	7	7.1	5
All inserts Without B60R20 & B60R30	0.018	8	0.32	7	7.0	5
All inserts Without B90R10, B90R20 & B90R30	0.015	11	0.23	13	7.3	5

The experimental data in Table 6-2 are plotted in Figure 6-2 to show how well each correlation fits to the experimental data which are not used to determine the coefficients.

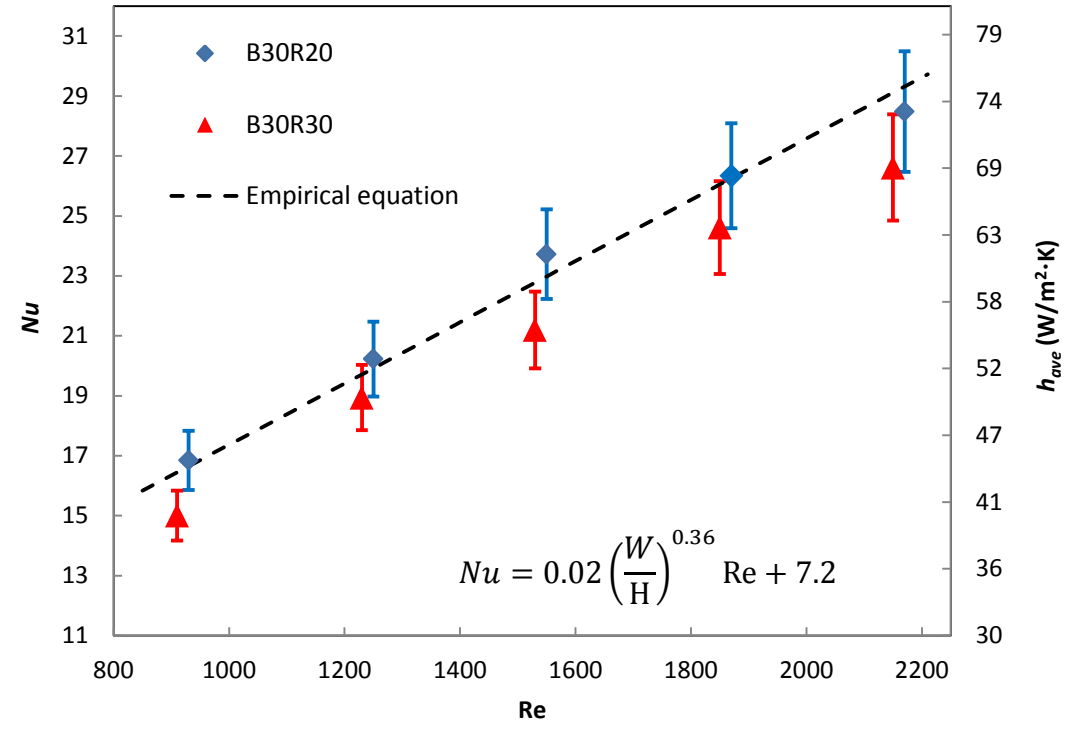

(a)

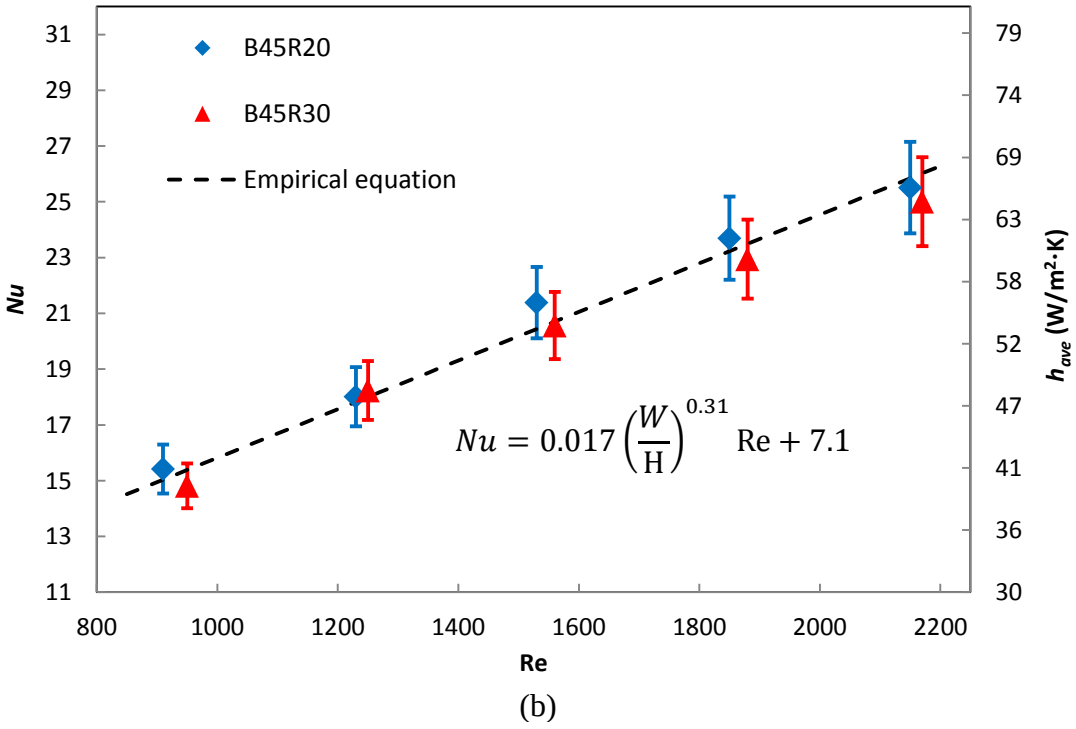

(b)

Figure 6-2 Comparison between the experimental and empirical *Nu* (a) B30R20 and B30R30, (b) B45R20 and B45R30, (c) B60R20 and B60R30, and (d) B90R10, B90R20, and B90R30 (Using data in Table 6-2).

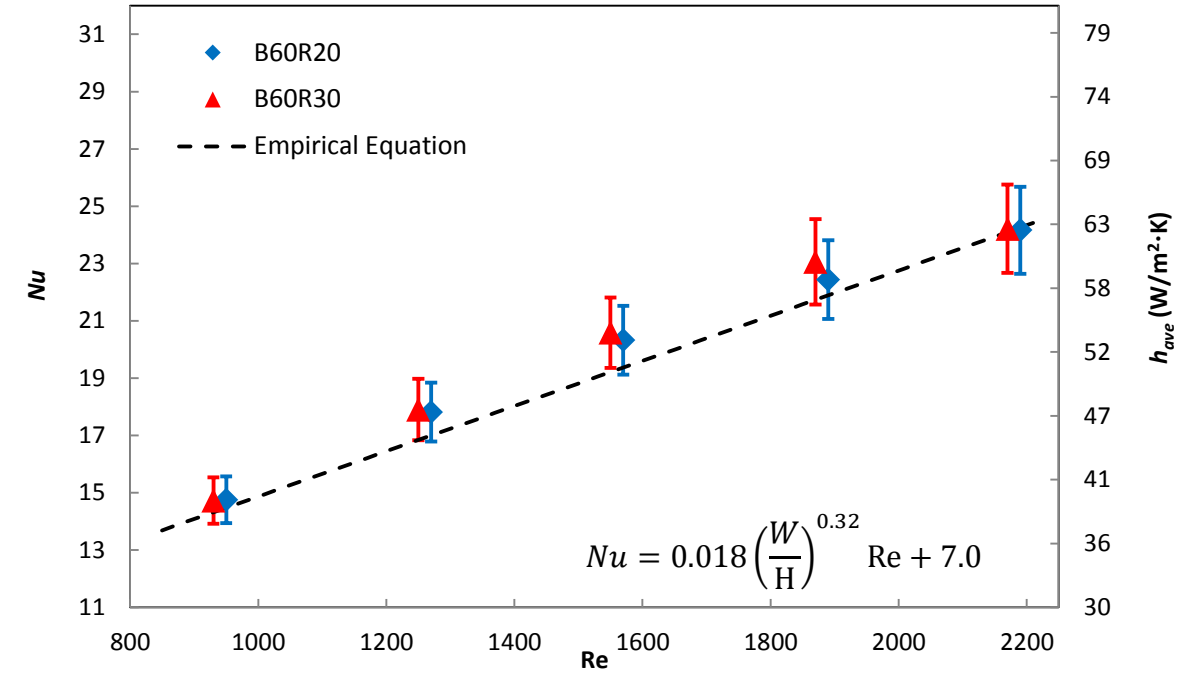

(c)

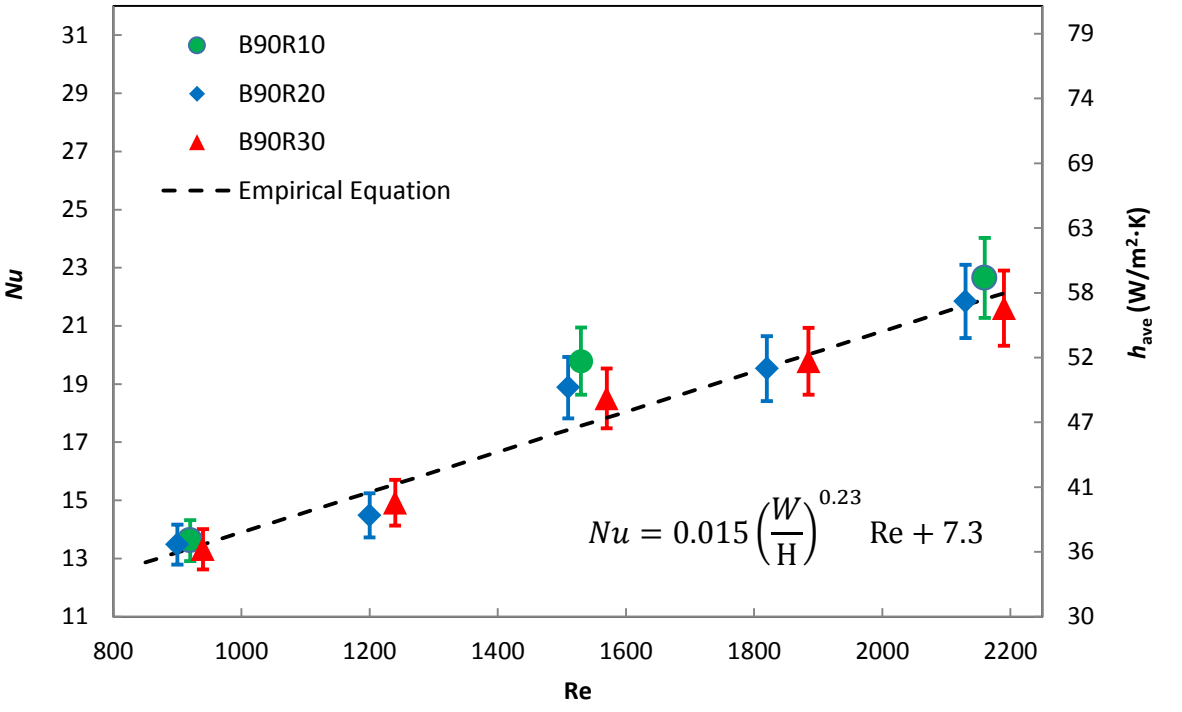

(d)

Figure 6-2 Continued- Comparison between experimental and empirical *Nu* (a) B30R20 and B30R30, (b) B45R20 and B45R30, (c) B60R20 and B60R30, and (d) B90R10, B90R20, and B90R30 (Using data in Table 6-2).

The results in Figure 6-2 show that the proposed correlations can predict most of the experimental data within their uncertainties. However, there are 5 data points where the difference between $Nu_{\text{empirical}}$ and Nu_{exp} is greater than the 95% uncertainty bounds of the experimental data: three cases in B30R30, one case in B90R10 and one case in B90R20. Since the correlation is an extrapolation when the spacing of the cylindrical bars is 30 mm and 90 mm, it is not surprising that the error of the estimation is larger for these cases than for the case of interpolation (i.e., 45 mm and 60 mm cylindrical bars spacing).

Equation (6-4) presents the final correlation of the average Nusselt number for which all experimental data (except B90R10) are used to calculate the coefficient of the correlation. In equation (6-4) the Nusselt number is correlated in terms of the cylindrical bars intervals (H), the channel width (W), and the Reynolds number.

$$Nu = (0.017 \pm 0.001)\left(\frac{W}{\mathrm{H}}\right)^{0.31\pm 0.02}\mathrm{Re} + (7.1 \pm 0.3)\begin{cases} 900 \le \mathrm{Re} \le 2200 \\ \mathrm{Pr} = 0.7 \\ 19 \le \mathrm{H}/D \le 56 \\ W/D = 3.1 \end{cases} \tag{6-4}$$

Equation (6-4) is used to calculate the empirical Nusselt number which is compared with the experimental value of the Nusselt number; the difference between the empirical and experimental value is reported in Appendix A.4. Also, the difference between the empirical and experimental Nu is shown for all inserts (including B90R10) in Figure 6-2.

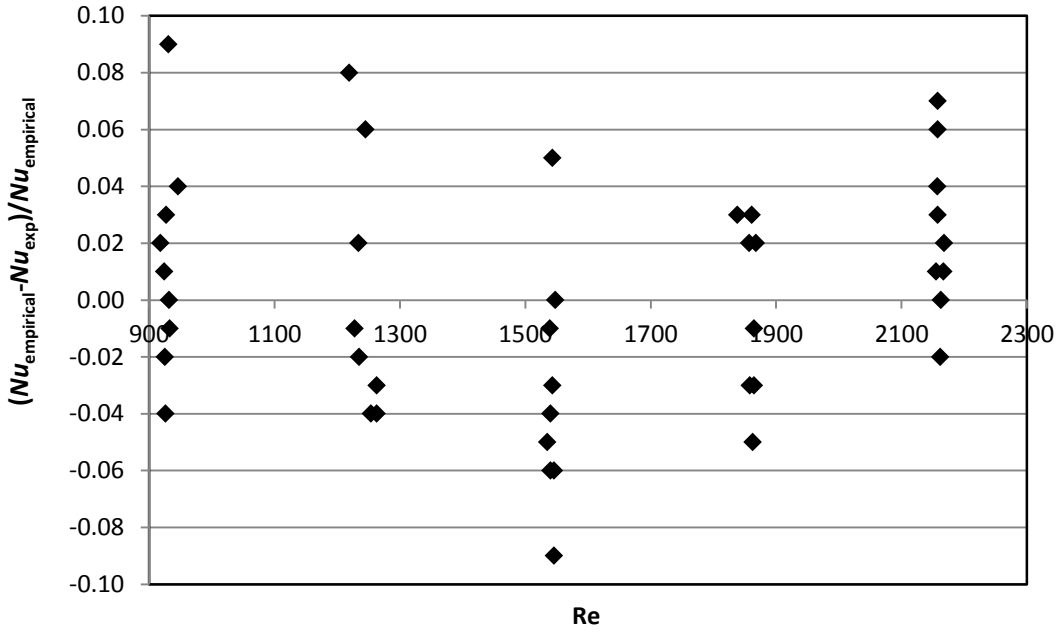

Figure 6-2 Difference between the empirical and experimental Nusselt number (data from Appendix A.4).

The results show that the empirical correlation (equation (6-4)) predicts the *Nu* for the inserts within the uncertainty of the experimental measurements.

6.3. Darcy friction factor correlation

The experimental results in Chapter 5 show that the Darcy friction factor approximately changes as an exponential function of Re. Also, the friction factor has an asymptotic value at large value of Re. Therefore, the general form of the equation of equation (6-5) is proposed for the relationship between friction factor and the Re.

$$f_D = a_2 \exp(\frac{b_2}{\mathrm{Re}}) \tag{6-5}$$

The experimental data for the friction factor of the inserts (except data of B90R10) are used to determine the coefficients for the equation (6-5) for different spacings between cylindrical bars. Since changing the plastic ribs spacing of the inserts changes the friction

factor within the uncertainty of the measurements (Figure 5-1 to Figure 5-4), the plastic ribs spacing is not included in the correlation parameters.

The same procedure as described in Section 6.2 is followed to find the correlation for the fiction factor. Table 6-3 presents the calculated coefficients of equation (6-5) for the inserts to determine how these coefficients change with the spacing between the cylindrical bars.

Table 6-3 Coefficient of $f_D = a_2 \exp(\frac{b_2}{\mathrm{Re}})$ for different cylindrical bars intervals.

Insets	a_2	σ_{a_2}/a_2 [%]	b_2	σ_{b_2}/b_2 [%]
B30R20 B30R30	0.230	4.2	753.6	7.5
B45R20 B45R30	0.187	4.3	812.5	7.2
B60R20 B60R30	0.166	4.2	806.4	7.0
B90R20 B90R30	0.172	4.1	687.9	8.0

The calculated coefficients in Table 6-3 show that the coefficient a_2 decreases and then increases by increasing the spacing between the cylindrical bars. The coefficient b_2 increases and then decreases as the bars intervals increases. Therefore, it would be hard to find the relation of the coefficients a_2 and b_2 as a function of spacing between cylindrical bars. For this purpose, it is assumed that the coefficient of a_2 is independent of geometry of the inserts and the average value of the coefficients of a_2 is used as a constant coefficient in the empirical equation. In the next step, the coefficient b_2 is calculated for each cylindrical bars spacing based on the average value of the a_2 and reported in Table 6-4.

Table 6-4 Coefficient of b_2 based on the average a_2 in correlation of $f_D = a_2 \exp(\frac{b_2}{\mathrm{Re}})$.

Insets	$\overline{a_2}$	$\sigma_{\bar{a}_2}/\bar{a}_2$ [%]	b_2	σ_{b_2}/b_2 [%]
B30R20 B30R30	0.188	2.1	997.9	2.0
B45R20 B45R30	0.188	2.1	797.6	2.7
B60R20 B60R30	0.188	2.1	636.9	2.7
B90R20 B90R30	0.188	2.1	567.5	3.0

The results in Figure 6-3 show that the coefficient of b_2 decreases as the spacing between cylindrical bars (H) increases. Figure 6-3 plots the coefficient of b_2 *as a* function of the inverse of the cylindrical bars intervals. Figure 6-3 shows that the coefficient of b_2 behaves linearly as a function of the inverse of the cylindrical bars intervals. Therefore, the general form of equation (6-6) is proposed for the empirical correlation of Darcy friction factor in terms of the Re and the spacing between the cylindrical bars.

$$f_D = A_1 \exp\left(\frac{B_1 \frac{W}{\mathrm{H}} + C_1}{\mathrm{Re}}\right) \tag{6-6}$$

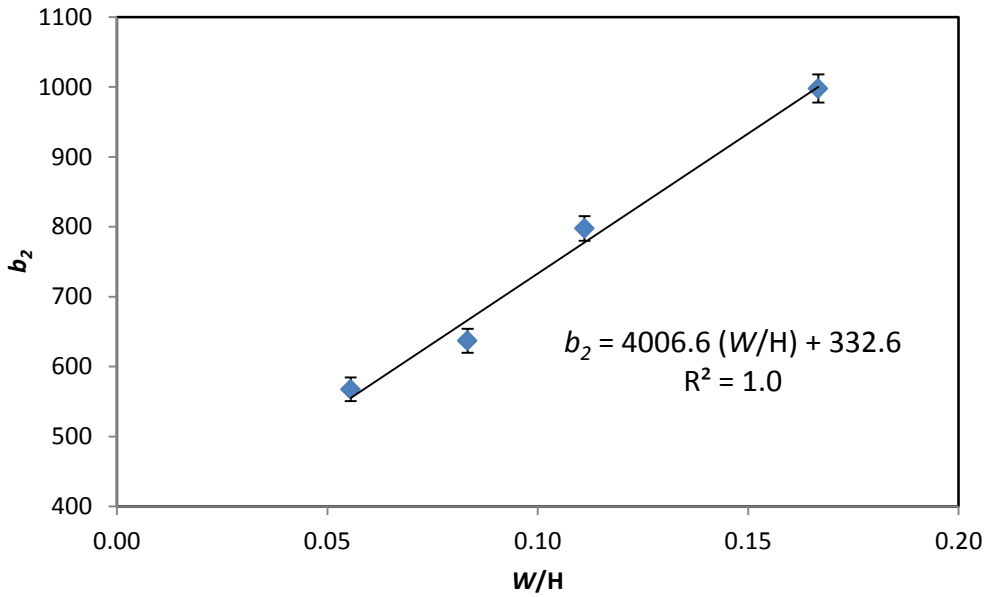

Figure 6-3 Relation between coefficient b_2 and (W/H).

The leave one out cross validation method is checked for the proposed friction factor correlation to identify how well the correlation can predict the experimental data by the Re and the spacing between cylindrical bars. Table 6-5 shows the coefficient of the correlation for different sets of experimental data.

Table 6-5 Determination of coefficient of $f_D = A_1 \exp\left(\frac{B_1 \frac{W}{H} + C_1}{Re}\right)$.

Inserts used in determination of correlation	A_1	σ_{A_1}/A_1 [%]	B_1	σ_{B_1}/B_1 [%]	C_1	σ_{C_1}/C_1 [%]
All inserts Without B30R20 & B30R30	0.174	2.4	4159.1	10.6	426.1	11.5
All inserts Without B45R20 & B45R30	0.182	2.4	3764.9	5.6	389.6	10.2
All inserts Without B60R20 & B60R30	0.190	2.4	3695.8	5.8	360.8	11.5
All inserts Without B90R10, B90R20 & B90R30	0.188	2.4	3957.8	7.1	333.3	14.7

Four different correlations for each set of data in Table 6-5 are plotted in

Figure 6-4.

Figure 6-4 shows the empirical value and the experimental data of the friction factor to compare the empirical prediction of the experimental data points while these data points were excluded in deriving the coefficients of equation (6-6).

Figure 6-4 shows that the empirical equation predicts most of the experimental friction factor data within their uncertainties. However, there are 5 data points where the difference between $(f_D)_{\text{empirical}}$ and $(f_D)_{\text{exp}}$ are larger than the 95% uncertainty bounds for the experimental data (one case in B30R30, one case in B90R20, and three cases in B90R10).

The difference between the empirical and experimental data is more significant for the cylindrical bars intervals of 30 and 90 mm. As an example, the experimental data of the inserts with cylindrical bars spacing of 45 mm, 60 mm, and 90 mm are used to find the coefficients of the correlation and predict the experimental data of B30R20 and B30R30 in

Figure 6-4. The empirical correlation predicts the friction factor out of the uncertainty bounds in experimental measurements due to the larger error in extrapolation.

The error in the prediction of friction factor is the largest for B90R10 compared to the other inserts. The main reason is that the experimental data of B90R10 were excluded in finding the empirical equation for the Darcy friction factor. The other reason is due to the larger error of estimation for the case of extrapolation.

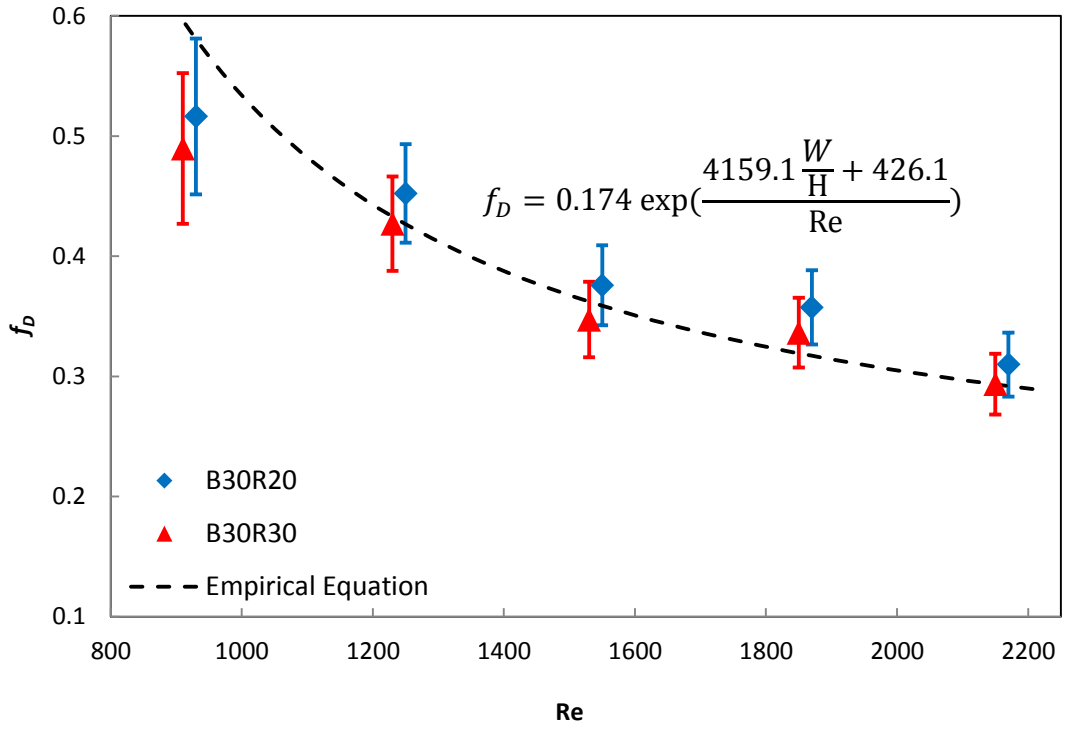

(a)

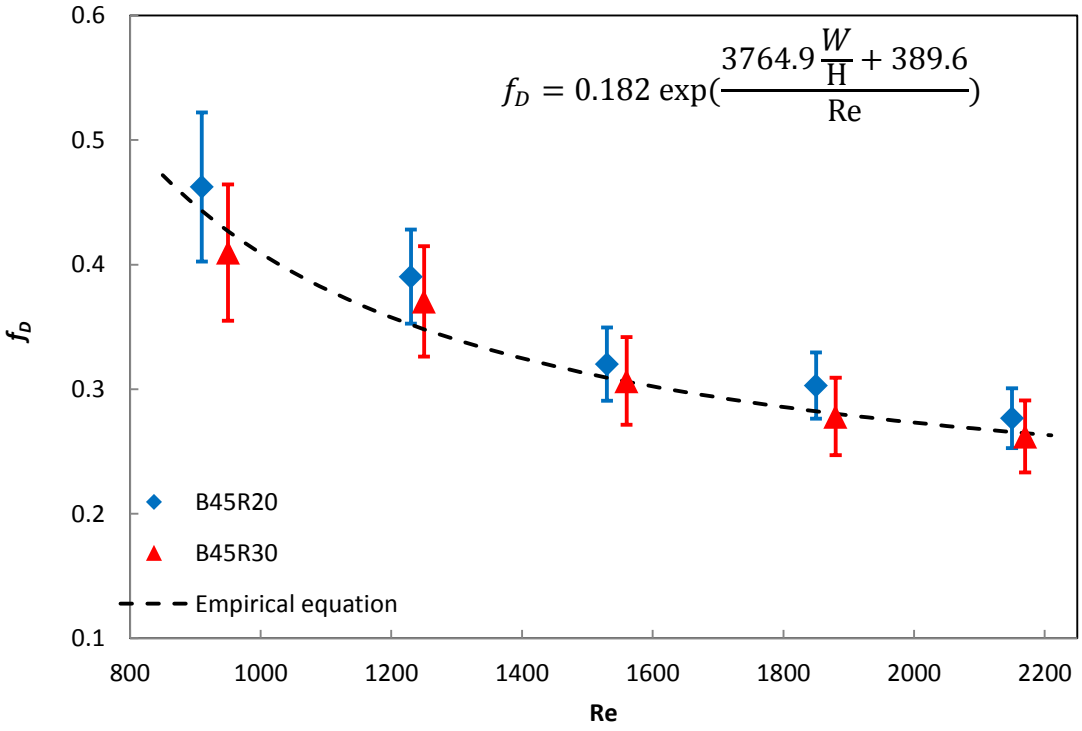

(b)

Figure 6-5 Comparison between empirical and experimental f_D for (a) B30R20 and B30R30, (b) B45R20 and B45R30, (c) B60R20 and B60R30, and (d) B90R10, B90R20, and B90R30 (using data in Table 6-5).

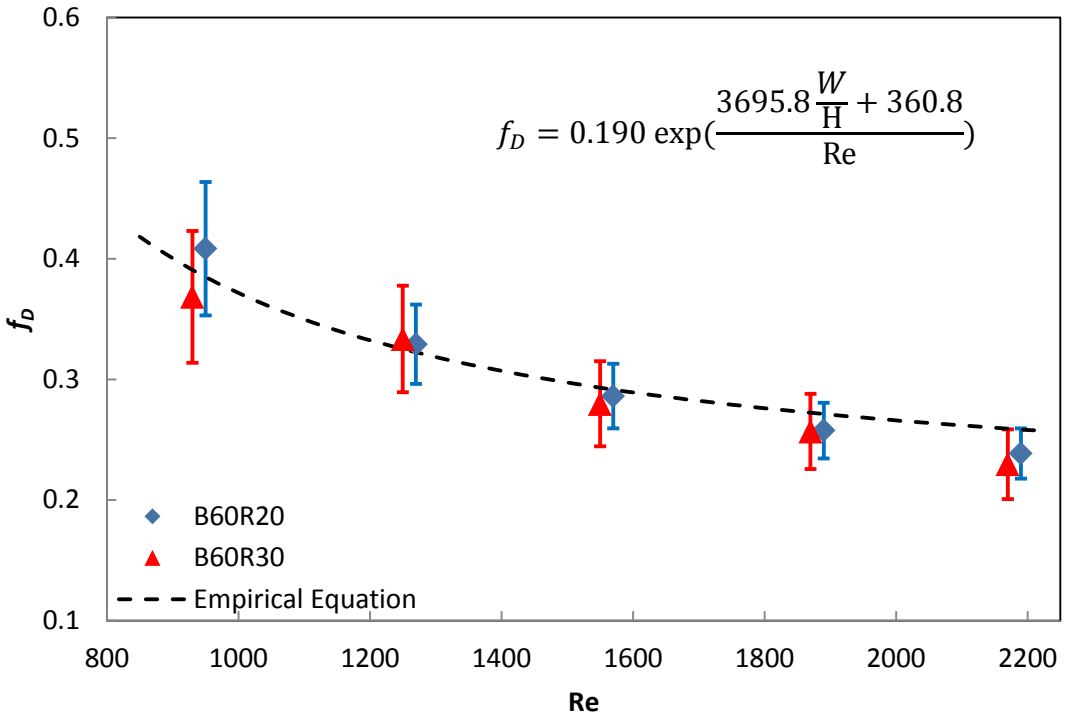

(c)

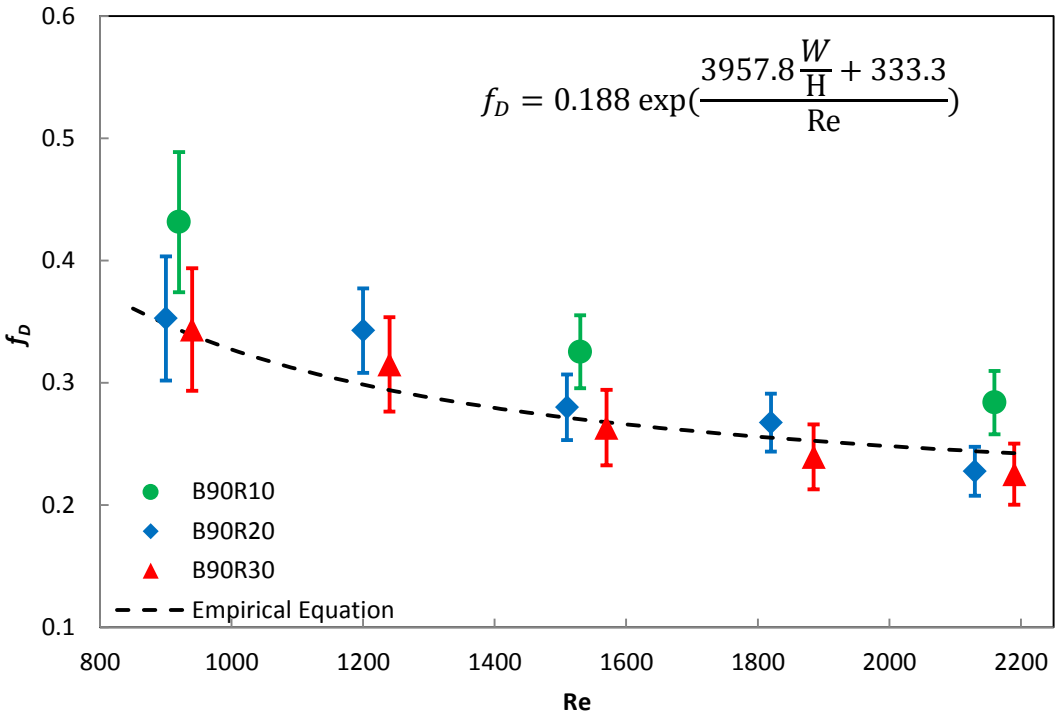

(d)

Figure 6-4 Continued- Comparison between empirical and experimental f_D for (a) B30R20 and B30R30, (b) B45R20 and B45R30, (c) B60R20 and B60R30, and (d) B90R10, B90R20, and B90R30 (using data in Table 6-5).

All experimental f_D for the inserts (except B90R10) are used to calculate the empirical correlation of the Darcy friction factor which is shown in Equation (6-7).

$$f_D = (0.183 \pm 0.004)\exp\left(\frac{(3801 \pm 205)W/H + (386 \pm 36)}{\mathrm{Re}}\right) \begin{cases} 900 \le \mathrm{Re} \le 2200 \\ Pr = 0.7 \\ 19 \le H/D \le 56 \\ W/D = 3.1 \end{cases} \quad (6\text{-}7)$$

Equation (6-7) predicts the Darcy friction factor for the inserts within the test section of WEIT facility in terms of the Re, the channel width (W), and the cylindrical bars intervals (H). The experimental and empirical values of the Darcy friction factor and the difference between the experimental and empirical values for different inserts at different Re are shown in Appendix A.5. Also, the difference between the experimental and empirical f_D for the inserts is shown in Figure 6-5.

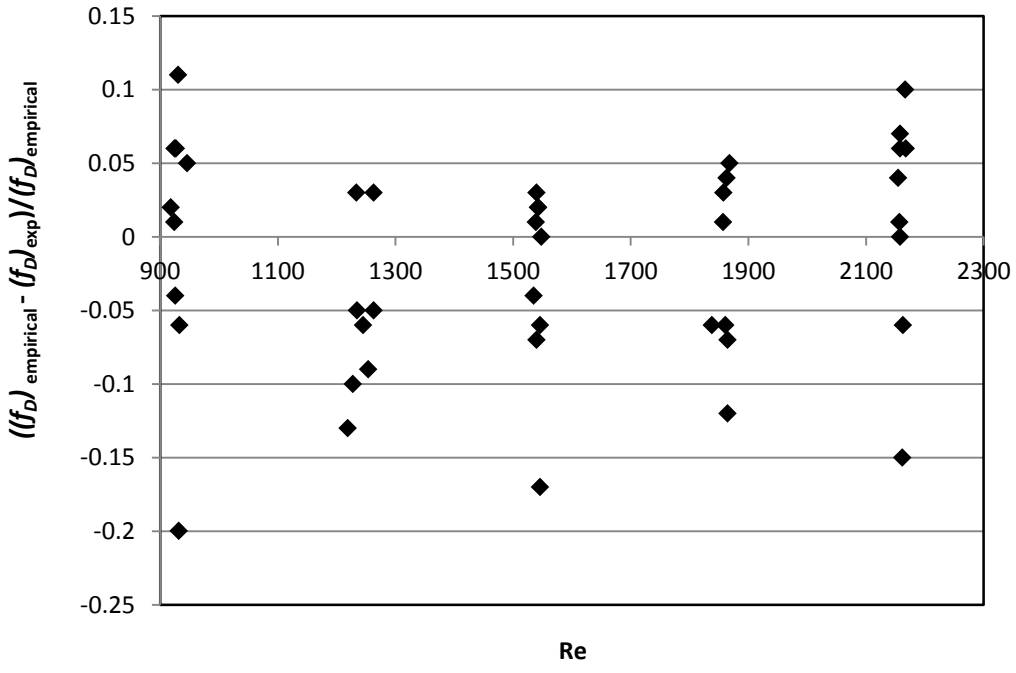

Figure 6-5 Difference between empirical and experimental f_D (data from Appendix A.5).

The results in Figure 6-5 show that the empirical equation predicts the experimental value of the Darcy friction factor within the uncertainty of the experimental and empirical values. The nominal difference between the empirical and experimental is 7 percent, which is acceptable and shows the accuracy of the empirical correlation for the Darcy friction factor. Even the highest difference between the empirical and experimental value of friction factor is about 20 percent for B90R10, which is acceptable because the B90R10 was excluded from deriving the correlation and this error mainly is due to the extrapolation.

CHAPTER 7

APLICATION OF TURBULENCE ENHANCING INSERTS IN A LAMEE

7.1. Introduction

The main functions of the turbulence enhancing inserts in the air channels of a LAMEE are to support the membranes and enhance the heat and mass transfer between the air and solution flow.

To show the application of the experimental data in this thesis, this chapter presents the experimental and numerical results from a LAMEE that has the B90R10 insert in the air channel. The LAMEE was built and tested by Davood Ghadiri Moghaddam [30] and consists of a single air channel with one solution channel on each side.

7.2. LAMEE properties

Manufacturing a full size LAMEE is costly and time consuming. Therefore a single panel LAMEE (the small scale of a LAMEE) is designed to investigate the defects of a LAMEE and improve the performance of the LAMEE [31].

Figure 7-1 shows an isometric cross-section view of the small-scale single-panel LAMEE that is used in this thesis. The single-panel LAMEE is a cross-counter flow flat plate exchanger with a 5-mm-wide air channel located between two 0.8-mm-wide solution channels. The air channel and the solution channels are separated by a semi-permeable membrane. The

B90R10 insert is used within the air channel of the small-scale single-panel LAMEE. Table 7-1 gives the design specifications of the single-panel LAMEE [31].

Table 7-1 The small-scale single-panel LAMEE specifications [31].

Parameter	**Value**
Exchanger length (mm)	490
Exchanger aspect ratio (length over height)	5.2
Air channel thickness (mm)	5
Solution channel thickness on each side (mm)	0.8
Number of paths in solution channels	8
Membrane thermal conductivity (W/m·K)	0.065
Membrane thickness (mm)	0.265
Membrane type	GE
Resistance of membrane (s/m)	24
Insert dimension and name	B90R10

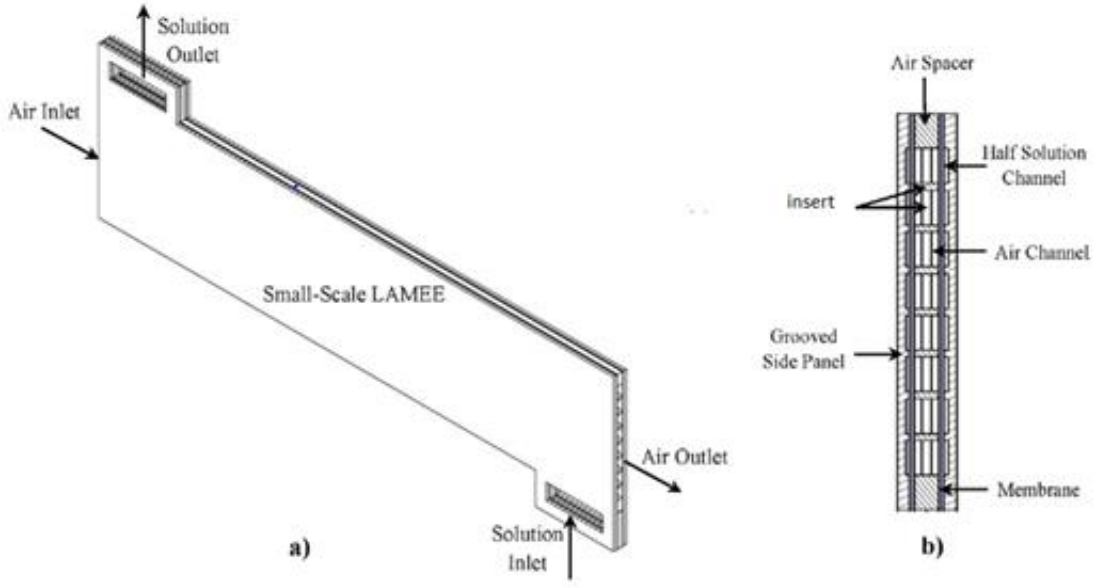

Figure 7-1 The small-scale single-panel LAMEE a) air and solution configuration, and b) cross-section view [31].

7.3. Single-panel energy exchanger test (SPEET) facility

The single-panel energy exchanger test (SPEET) facility is used to test the performance of the single-panel LAMEE. The maximum supply air flow rate in SPEET facility is 5 cfm and the detail design of the facility can be found in [30]. A supply air system, an open solution loop, and a test section are the main sections of the SPEET facility. Figure 7-2 shows the detail sections of the SPEET facility.

The dry air is supplied to the SPEET facility from a compressor with ~4%RH. The inlet air flow rate to the system is adjusted by a flow controller. The inlet air to the system is conditioned to the desired test conditions by passing the air through two water tanks and a heater. The single-panel LAMEE is located in the test section of the SPEET facility. The temperature and humidity of the air at the inlet and outlet of the test section are measured within the inlet and outlet headers of the test section [31].

LiCl is used as a solution in the open solution loop. A peristaltic pump pumps the solution from the supply tank to the inlet header of the single-panel LAMEE. The temperature of the solution is measured by the shield thermocouples at the inlet and outlet headers of the single-panel LAMEE. The single-panel LAMEE is installed in the test section of the SPEET facility and the air and solution pass through the channels of the LAMEE and heat and mass transfer occur between the air and the fluid through the membrane [30].

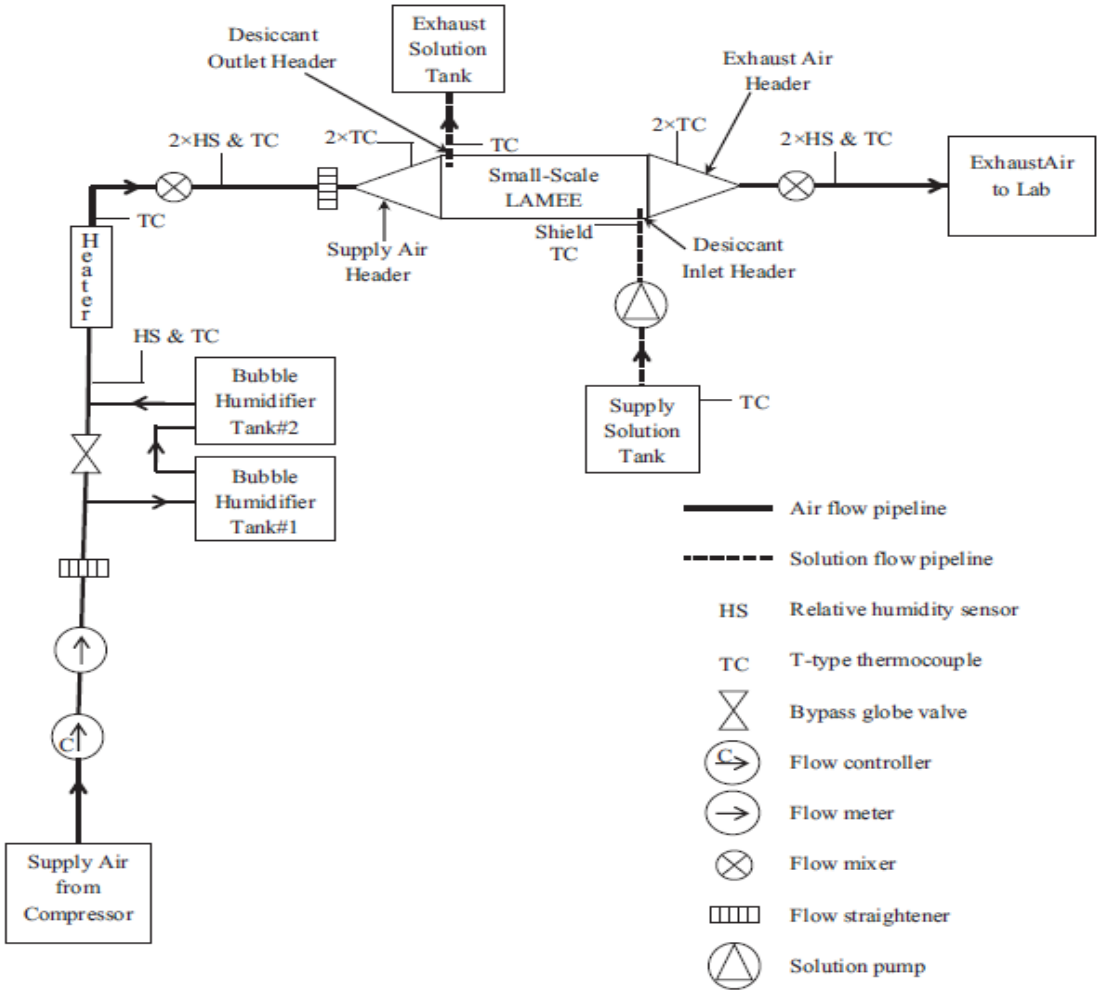

Figure 7-2 Schematic view of the SPEET facility and measurement instruments [31].

7.4. Performance evaluation of a LAMEE

7.4.1. Effectiveness

The performance of a LAMEE is evaluated by the sensible, latent, and total effectiveness. The sensible effectiveness is defined as the heat transfer in the LAMEE over the maximum possible heat transfer. The latent and total effectivenesses are defined in a similar way; however, the heat transfer is replaced by the moisture and the energy transfer in the latent and total effectiveness, respectively (Equations (7-1), (7-2), and (7-3)),

$$\varepsilon_{\text{sensible}} = \frac{T_{\text{air,in}} - T_{\text{air,out}}}{T_{\text{air,in}} - T_{\text{sol,out}}}, \tag{7-1}$$

$$\varepsilon_{latent} = \frac{W_{\text{air,in}} - W_{\text{air,out}}}{W_{\text{air,in}} - W_{\text{sol,out}}}, \tag{7-2}$$

$$\varepsilon_{\text{total}} = \frac{\varepsilon_{\text{sensible}} + H^{*}\varepsilon_{\text{latent}}}{1 + H^{*}}, \tag{7-3}$$

where ε is the effectiveness of the exchanger, T is the temperature, W is the humidity ratio, H^{*} is the operating factor in equation (7-4). The subscripts air, sol, in, out represent the air, solution, and inlet and outlet of the exchanger, respectively, and

$$H^{*} = \frac{W_{\text{sol,in}} - W_{\text{air,in}}}{T_{\text{sol,in}} - T_{\text{air,in}}} \frac{h_{\text{fg}}}{C_{\text{P,air}}}, \tag{7-4}$$

where h_{fg} is the enthalpy of the phase change for the water vapor [J/kg], and $C_{\text{P,air}}$ is the specific heat capacity of the air at constant pressure [J/kg·K].

7.4.2. *NTU* and Cr^{*}

The ε of a LAMEE depends on two dimensionless parameters: the heat capacity ratio, Cr^{*}, and the number of heat transfer units, *NTU*. Cr^{*} depends on the mass flow rates of the air and the solution and the specific heat capacity ratio of the air and solution (equation (7-4)). *NTU* depends on the overall heat transfer coefficient, the heat transfer area of the exchanger, and the heat capacity of the air (equation (7-4)),

$$Cr^{*} = \frac{C_{\max}}{C_{\min}} = \frac{(\dot{m}C_P)_{\text{air}}}{(\dot{m}C_P)_{\text{solution}}}, \tag{7-5}$$

$$NTU = \frac{UA}{C_{\min}} = \frac{UA}{(\dot{m}C_P)_{\text{air}}}, \tag{7-6}$$

where $\dot{m}$ is the mass flow rate (g/s), and U is the overall heat transfer coefficient of the exchanger which depends on the convective heat transfer coefficient of air and solution, and conductivity of the membrane and is defined in equation (1-1).

$$U = [\frac{1}{h_{\text{air}}} + \frac{\delta}{K_{\text{mem}}} + \frac{1}{h_{\text{solution}}}]^{-1}, \quad (1\text{-}1)$$

The h_{air} in equation (1-1) is calculated from the measured Nu within the test section of the WEIT facility and using equation (3-7). Section 1.2.1 discussed the effect of enhancing h_{air} on the overall heat transfer coefficient.

The single-panel LAMEE is tested in the SPEET facility at Cr^* of 1, 3, 5, and 7. In these tests the NTU is constant and is equal to 3. The air and solution conditions and the effectiveness of the single-panel LAMEE are presented in Table 7-2.

Table 7-2 Measured air and solution inlet and outlet conditions for the small-scale LAMEE at NTU=3 and different Cr* with LiCl salt solution under different operating conditions [31].

Cr*	Inlet Conditions					Outlet Conditions					Results		
	$T_{\text{air,in}}$ (°C)	$W_{\text{air,in}}$ $(\frac{\text{g}}{\text{kg}})$	$T_{\text{sol,in}}$ (°C)	$C_{\text{sol,in}}$ (%)	$W_{\text{sol,in}}$ $(\frac{\text{g}}{\text{kg}})$	$T_{\text{air,out}}$ (°C)	$W_{\text{air,out}}$ $(\frac{\text{g}}{\text{kg}})$	$T_{\text{sol,out}}$ (°C)	$C_{\text{sol,out}}$ (%)	$W_{\text{sol,out}}$ $(\frac{\text{g}}{\text{kg}})$	$\varepsilon_{\text{sens}}$ (%)	ε_{lat} (%)	ε_{tot} (%)
1	35	17.28	24	34.59	5.54	30.6	11.24	39.8	33.96	15.21	40.8	51.6	48.6
3	35	17.38	24	34.59	5.54	26.6	8.31	34.2	34.24	10.75	76.2	76.6	76.5
5	35	17.29	24	34.59	5.53	25.8	7.71	31.1	34.36	8.83	83.3	81.5	82.0
7	35	17.30	24	34.59	5.54	25.5	7.43	29.2	34.43	7.80	86.6	84.0	84.7

7.5. Numerical model

The numerical model for the single-panel LAMEE and the detail of the assumptions and differential governing equations are presented by Davood Ghadiri Moghaddam [31]. One of the important inputs for the numerical model is the air side convective heat transfer coefficient which can be obtained from the experimental data in Chapter 5 or from the correlation in Chapter 6. Since the B90R10 insert is used as the insert within the air channel of the single-panel LAMEE, the experimental data of the B90R10 at different Re is used as an

input for the numerical model. Figure 7-3 presents the effect of the enhanced Nusselt number on the steady-state sensible, latent and total effectivenesses of the single-panel LAMEE.

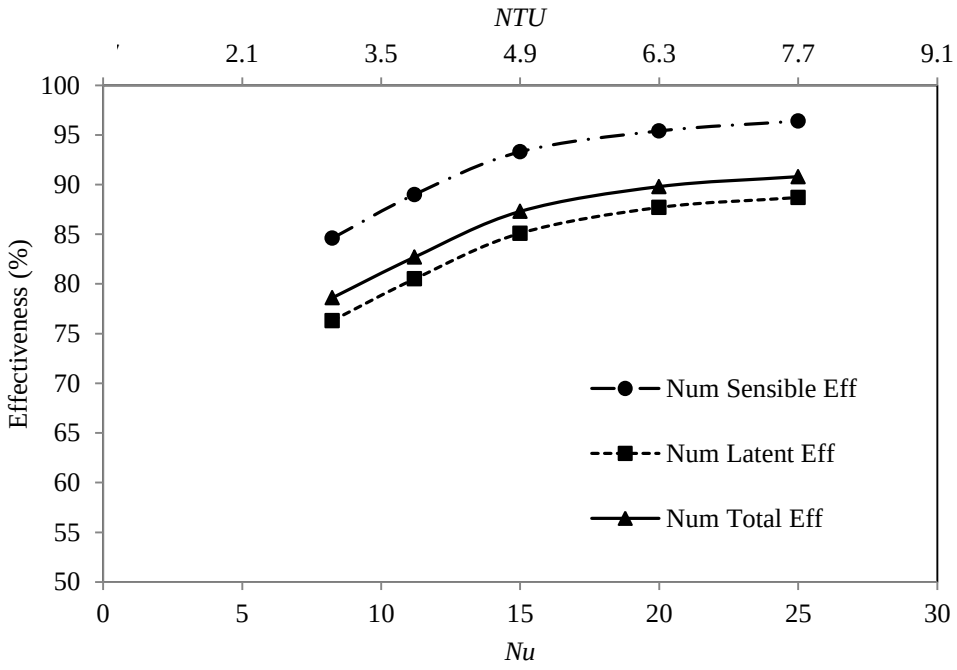

Figure 7-3 Effect of the enhanced Nusselt number on the effectiveness of the single-panel LAMEE at *NTU*=3 and Cr^*=5;the inlet conditions are the same as Table 7-2 [31].

The first point on Figure 7-3 shows the laminar Nusselt number for the hollow air channel of the single panel LAMEE. The other points on the plot are enhanced Nusselt number by using the B90R10 within the air channel. As an illustration, the enhanced Nusselt number of 11.2 at an air flow Reynolds number of 620 improves the sensible, latent, and total effectiveness of the single panel LAMEE by 4% with respect to the hollow air channel. The effect of the enhanced Nusselt number is more obvious at higher Reynolds number where the effectiveness of the LAMEE improves 11% by the insert at Re = 1620 and *Nu* = 20 [31].

The results show that the enhanced convective heat transfer coefficient affects the *NTU* and effectiveness of a LAMEE. Improvement in the air side Nusselt number increases the sensible and latent effectiveness. Improvement in the air-side convective heat transfer

coefficient increases the Sherwood number through the Chilton-Colburn analogy (equation (7-7)) and the Sherwood number has a linear relation with the convective mass transfer coefficient (equation (7-8)). Therefore, enhancement in the convective heat transfer coefficient causes improvement in the convective mass transfer coefficient as well [31],

$$Sh = Nu \cdot Le^{(-.065 \pm 0.01)}, \tag{7-7}$$

$$Sh = \frac{h_m D_h}{D_{va}}, \tag{7-8}$$

where Sh is the Sherwood number, Le is the ratio of the thermal and mass diffusivities, h_m is the convective mass transfer coefficient [kg/m^2·s], and D_{va} is the diffusivity coefficient of vapor into air [m^2/s].

7.6. Comparison of the numerical and experimental single-panel LAMEE effectiveness

The experimental values of the enhanced Nu for B90R10 are used as the inputs for the numerical code to evaluate the steady state performance of the single-panel LAMEE at the test conditions presented in Table 7-2. Figure 7-4 presents the experimental and numerical steady state performance of the single-panel LAMEE with their uncertainties at Cr^* of 1, 3, 5, and 7.

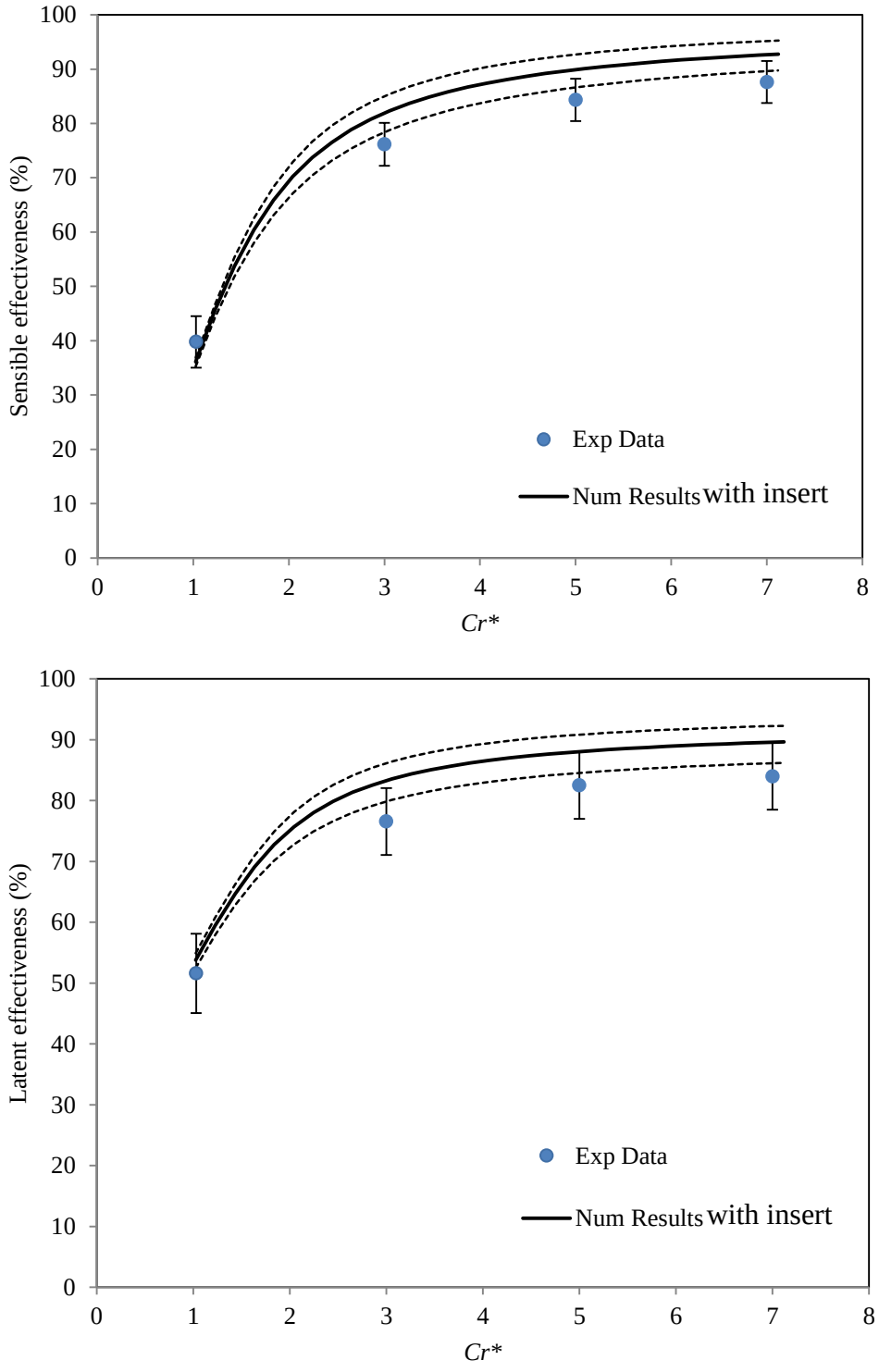

Figure 7-4 Comparison of the numerical and experimental steady state effectiveness of the single-panel LAMEE at different Cr^* and *NTU* of 3.8 [31].

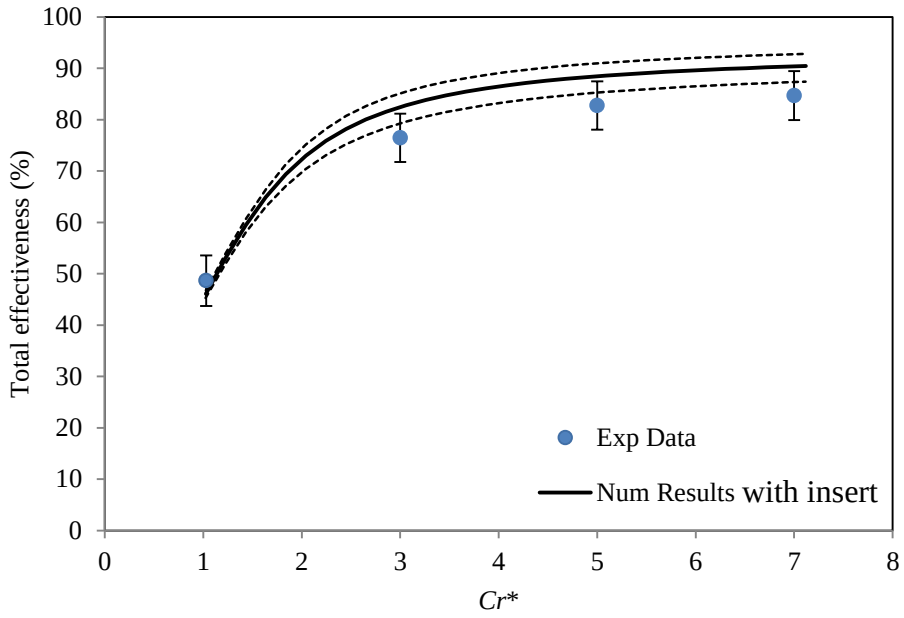

Figure 7-4 Continued- Comparison of the numerical and experimental steady state effectiveness of the single-panel LAMEE at different Cr^* and *NTU* of 3.8 [31].

The results in Figure 7-4 confirm that the experimental and numerical effectiveness cover each other within their uncertainties. The uncertainty of the experimental Nusselt number is taken into account for the uncertainties of the numerical effectiveness. The results confirm that the Nusselt numbers measured in the WEIT facility and the presented correlation in this thesis may be used in numerical models to evaluate the performance of LAMEEs. This is one step in component testing, in the future, which could eliminate the need to build and test an actual exchanger.

CHAPTER 8
CONCLUSIONS AND FUTURE WORK

8.1. Summary and conclusions

The main goal of this research is to measure and correlate the convective heat transfer coefficient in a rectangular air channel that contains a turbulence enhancing insert and use these results to investigate the effect of the inserts on the performance of a LAMEE.

A small-scale wind tunnel for exchangers insert testing (WEIT) facility is used to measure Nu and f_D for the various inserts used in the air channels of a LAMEE. The test section of the WEIT facility is 5 mm wide and has a rectangular cross section. The flow is fully developed laminar flow at entrance of the test section and thermally developing thorough the test section. The experiments are conducted at steady-state conditions with constant heat flux conditions on the side walls for Re between 900 and 2200 (a typical range of operation for a LAMEE).

The experiments were conducted for the rectangular channel with and without a turbulence enhancing insert. The empty, hollow channel is tested to provide a comparison to the data for the channel with inserts and to validate the experimental data with the available data in the literature. The experimental results for the hollow channel agree with the literature data verifying the experiments and confirming that the flow is hydrodynamically fully developed in the hollow channel and the thermal boundary layer is in the developing region for the hollow test section.

The inserts in this thesis consisted of cylindrical cross bars (B) and horizontal ribs (R). Nine different inserts were tested (Table 2-1) to investigate the effect of the cross-bar and rib spacing on the heat transfer and pressure drop within the air channel of the LAMEE. The experimental data show that the inserts enhance the heat transfer and increase the pressure drop within the air channels. The inserts enhance the heat transfer by mixing the air and disturbing the thermal boundary layer. However, the inserts increase the pressure drop by increasing the form and surface drag due to increased velocity gradients near the wall and vortex shedding downstream of the cross-bars.

The experimental results show that changing the cross-bars spacing is more important than changing the ribs spacing. Reducing the cross-bars and ribs spacing increases the air mixing and the convective heat transfer coefficient. For example decreasing the cross-bars spacing from 45 mm (B45R20) to 30 mm (B30R20) increases the *Nu* by 12%, but increasing the ribs spacing from 20 mm (B45R20) to 30 mm (B45R30) decreases the *Nu* only by 4% which is within the uncertainty of the experimental measurement).

The experimental results show that, although the inserts enhance the heat transfer rate by a factor of 1.5 to 2.9, the inserts increase the friction factor within the air channel by a factor of 3.5 to 7.3. To provide a practical comparison of the inserts, the heat transfer enhancement due to the inserts was compared to the hollow channel for the situation where the pumping power was the same. The results in the thesis show that the inserts enhance the heat transfer by a factor of 1.2 to 1.8 relative to the hollow channel which has the same pumping power as the channel with the insert. Also, the experimental results show that heat transfer enhancement of the insert compared to the hollow channel is the highest for the Re between 1000 and 1500.

The following empirical correlations were developed to predict the Nusselt number and friction factor within the air channels of a LAMEE with turbulence enhancing inserts as a function of the inserts geometry and the air flow Re.

$$Nu = (0.017 \pm 0.001)(W/H)^{0.31\pm0.02}\mathrm{Re} + (7.1 \pm 0.3) \begin{cases} 900 \le \mathrm{Re} \le 2200 \\ Pr = 0.7 \\ 19 \le H/D \le 56 \\ W/D = 3.1 \end{cases}, \quad (6\text{-}4)$$

$$f_D = (0.183 \pm 0.004)\exp\left(\frac{(3801 \pm 205)W/H + (386 \pm 36)}{\mathrm{Re}}\right) \begin{cases} 900 \le \mathrm{Re} \le 2200 \\ Pr = 0.7 \\ 19 \le H/D \le 56 \\ W/D = 3.1 \end{cases}, \quad (6\text{-}8)$$

where Nu is the average Nusselt number, W is the width of the air channel (mm), H is the spacing between the cylindrical bars in inserts (mm), and f_D is the Darcy friction factor.

The Nu and f_D correlations agree with the experimental data within ±9% and ±13%, respectively. In nearly all cases, the predicted and experimental values for the Nu and f_D agree within the uncertainty of experimental measurements.

The application of one turbulence enhancing insert (B90R10) in a Single-panel LAMEE was investigated. The numerical model of the single-panel LAMEE used the experimental results of the WEIT facility and showed that the inserts improved the effectiveness of the single-panel LAMEE by 4% and 11% at the Re of 620 and 1620, respectively compared to the case of a hollow channel at the same face velocity.

8.2. Contribution

This research covered a gap in the literature on the subject of the heat transfer enhancement in membrane flat-plate exchangers with inserts. The main contribution of this research is obtaining experimental data that quantify the effect of the inserts on the heat

transfer enhancement within the air channels of flat plate membrane exchangers at low Reynolds number (lower than 2200). The effect of the cylindrical bars spacing on the heat transfer and pressure drop were studied. Also, empirical correlations were developed to predict the Nusselt number and friction factor across the inserts.

8.3. Future work

Heat flux enhancement in membrane exchangers is an open area for research. This research showed the impact of one type of insert on the heat transfer and performance of a specific membrane flat-plate exchanger. One area of the future work would be to study the insert geometry and their placement in the air channels of exchangers.

Another area would be investigating the effect of the inserts on mass flux enhancement in the LAMEEs and finding an analogy between the heat and mass transfer for the air channels of the LAMEEs.

REFERENCES

[1] H. Huisseune, C. T'Joen, P. De Jaeger, A. Willockx, and M. De Paepe, "Study of junction flows in louvered fin round tube heat exchangers using the dye injection technique," *Exp. Therm. Fluid Sci.*, vol. 34, pp. 1253–1264, 2010.

[2] B. B. Mikic, L. B. Vujisic, and J. Kapat, "Turbulent transition and maintenance of turbulence; implication to heat transfer augmentation," *Int. J. Heat Mass Tran.*, vol. 37, pp. 425–431, Mar. 1994.

[3] R. L. Webb and N. H. Kim, *Principles of Enhanced Heat Transfer*. New York: Taylor & amp; Francis, 2005, p. 795.

[4] D. R. M. Manglik and D. A. E. Bergles, "Enhanced Heat and Mass Transfer in the New Millennium: A Review of the 2001 Literature," *J. Enhanc. Heat Transf.*, vol. 11, no. 2, pp. 87–118, 2004.

[5] S. Kakaç (Sadık), R. K. Shah, and W. Aung, *Handbook of Single-phase Convective Heat Ttransfer*. New York: Wiley, 1987.

[6] Lj. b. Vujisic, "Heat Transfer at Transition to Turbulence in Channel Flows with Eddy Promoters," Ph.D. Thesis, Massachusetts Institute of Technology, Cambridge, MA, 1994.

[7] G. Ge, M. R. H. Abdel-Salam, R. W. Besant, and C. J. Simonson, "Research and applications of liquid-to-air membrane energy exchangers in building HVAC systems at University of Saskatchewan: A review," *Renew. Sustain. Energy Rev.*, vol. 26, pp. 464–479, 2013.

[8] H. B. Hemingson, "The impacts of outdoor air conditions and non-uniform exchanger channels on a run around membrane energy exchanger," M.Sc. thesis, University of Saskatchewan, Saskatoon, SK, 2010.

[9] L. Z. Zhang and S. M. Huang, "Coupled heat and mass transfer in a counter flow hollow fiber membrane module for air humidification," *Int. J. Heat Mass Tran.*, vol. 54, pp. 1055–1063, 2011.

[10] C.-O. Olsson and B. Sundén, "Experimental study of flow and heat transfer in rib-roughened rectangular channels," *Exp. Therm. Fluid Sci.*, vol. 16, no. 4, pp. 349–365, Apr. 1998.

[11] J. Zhu, M. Fiebig, and N. Mitra, "Numerical investigation of turbulent flows and heat transfer in a rib-roughened channel with longitudinal vortex generators," *Int. J. Heat Mass Tran.*, vol. 38, no. 3, pp. 495–501, 1995.

[12] C. M. B. Russell, T. V. Jones, and G. H. LEE, “Heat Transfer Enhancement Using Vortex Generators,” in *Proc. Seventh Heat Transfer Conf.*, Vol. 3, pp. 283-288, Hemisphere, New York, 1982.

[13] A. M. Jacobi and R. K. Shah, “Heat transfer surface enhancement through the use of longitudinal vortices: A review of recent progress,” *Exp. Therm. Fluid Sci.*, vol. 11, no. 3, pp. 295–309, Oct. 1995.

[14] E. M. Sparrow and W. Q. Tao, “Enhanced Heat Transfer in a Flat Rectangular Duct With Streamwise-Periodic Disturbances at One Principle Wall,” *Trans. of the ASME J. Heat Transfer*, vol. 105, no. 4, p. 851, 1983.

[15] J. C. Han, L. R. Glicksman, and W. M. Rohsenow, “An investigation of heat transfer and friction for rib-roughened surfaces,” *Int. J. Heat Mass Tran.*, vol. 21, no. 8, pp. 1143–1156, Aug. 1978.

[16] L. Zhang and S. Balachandar, “Heat transfer enhancement mechanisms in inline and staggered parallel-plate fin heat exchangers,” *Int. J. Heat Mass Tran.*, vol. 40, no. 10, pp. 2307–2325, 1997.

[17] M. Hamdan and M. A. Al-Nimr, “The Use of Porous Fins for Heat Transfer Augmentation in Parallel-Plate Channels,” *Transp. Porous Media*, vol. 84, no. 2, pp. 409–420, Dec. 2009.

[18] P. LePoudre, C. Simonson, and R. Besant, “Channel flow with sinusoidal screen insert,” in *Proceedings of the 19th Annual Conference of the CFD Society of Canada*, Montreal, QC, April 28-29, 2011.

[19] F. P. Incropera, D. P. DeWitt, T. L. Bergman, and A. S. Lavine, *Fundamentals of Heat and Mass Transfer*, vol. 6. New York: John Wiley & Sons, 2007, p. 997.

[20] ASME PTC 19.1, *Test Uncertainty*. New York: American Society of Mechanical Engineers, 1998.

[21] ISO 5167-2, *Measurement of Fluid Flow by Means of Pressure Differential Devices Inserted in Circular Cross-section Conduits Running Full -- Part 2: Orifice plates*. International Organization for Standards, 2003.

[22] F. M. White, *Fluid Mechanics*, vol. 17. Boston: McGraw-Hill Higher Education, 2009, p. 864.

[23] S. H. Chue, “Pressure probes for fluid measurement,” *Prog. Aerosp. Sci.*, vol. 16, no. 2, pp. 147–223, 1975.

[24] K. G. Ranga Raju, P. D. Porey, and G. L. Asawa, “Displacement effect in Pitot tube measurements in shear flows,” *J. Wind Eng. Ind. Aerodyn.*, vol. 66, no. 2, pp. 95–105, Feb. 1997.

[25] S. O. Olutimayin, “Vapor boundary layer growth during transient heat and moisture transfer in cellulose insulation,” M.Sc. thesis, University of Saskatchewan, Saskatoon, SK, 2004.

[26] R. K. Shah and A. L. London, *Laminar Flow Forced Convection in Ducts : a Source Book for Compact Heat Exchanger AnalyticalData*. New York: Academic press, 1978.

[27] M. Molki and E. M. Sparrow, “An empirical correlation for the average heat transfer coefficient in circular tubes,” *Trans. ASME J. Heat Trasnfer*, vol. 108, no. 2, pp. 482–4, 1986.

[28] J. Pfanzagl, *Parametric Statistical Theory*. Berlin: Walter de Gruyter, 1994, p. 374.

[29] J. Schneider and A. W. Moore, “A Locally Weighted Learning Tutorial using Vizier 1.0,” Computer Based Learning Unit, University of Leeds, 1997.

[30] D. G. Moghaddam, P. Lepoudre, G. Ge, R. W. Besant, and C. J. Simonson, “Small-scale single-panel liquid-to-air membrane energy exchanger (LAMEE) test facility development, commissioning and evaluating the steady-state performance,” *Energy Build.*, vol. 66, pp. 424–436, 2013.

[31] D. Ghadiri Moghaddam, A. Oghabi, G. Ge, R. W. Besant, and C. J. Simonson, “Numerical model of a small-scale liquid-to-air membrane energy exchanger: Parametric study of membrane resistance and air side convective heat transfer coefficient,” *Appl. Therm. Eng.*, vol. 61, pp. 245–258, 2013.

APPENDIX A

EXPERIMENTAL DATA

A.1. Energy balance

Table A-1 shows the test conditions and energy balance results for the heat transfer tests. T_{air} represents the bulk mean temperature of the air, $\dot{m}$ is the mass flow rate of the air, and the subscripts "in" and "out" represent the inlet and outlet of the test section, respectively. The heat transfer rates are calculated using.

$$Q_{heater} = VI - Q"_{loss}A\,, \tag{3-24}$$

$$Q_{\text{air}} = \dot{m}C_{\text{p,air}}(T_{\text{air,out}} - T_{\text{air,in}}), \tag{3- 25}$$

Table A-1 Energy balance results for the heat transfer tests.

	Re	$T_{\text{air,in}}$ (°C)	$T_{\text{air,out}}$ (°C)	$\dot{m}$ (g/s)	Q_{heater} (W)	Q_{air} (W)	$Q_{\text{air}}/Q_{\text{heater}}$ (%)
Hollow channel	920	24.1	60.6	1.3	50 ± 2	47 ± 2	94
	1260	26.1	51.6	1.7	49 ± 3	45 ± 2	92
	1550	24.5	47.0	2.1	52 ± 2	48 ± 3	93
	1850	26.4	46.2	2.6	53 ± 2	51 ± 3	96
	2160	25.0	41.9	3.0	55 ± 2	51 ± 3	93
Channel with B30R20	930	24.2	59.8	1.3	50 ± 2	46 ± 2	92
	1250	26.5	54.9	1.7	52 ± 3	50 ± 2	96
	1550	24.5	49.3	2.1	56 ± 2	53 ± 2	95
	1870	26.5	47.7	2.6	58 ± 2	55 ± 2	95
	2170	24.9	42.3	3.0	55 ± 2	53 ± 2	96
Channel with B30R30	930	23.5	56.5	1.3	46 ± 2	43 ± 2	93
	1230	25.9	53.7	1.7	50 ± 2	48 ± 2	96
	1540	23.3	46.2	2.1	53 ± 2	49 ± 2	92
	1840	26.5	46.7	2.5	56 ± 2	52 ± 2	93
	2160	25.2	42.2	3.0	54 ± 2	51 ± 2	94

Channel with B45R20	930	23.9	57.8	1.3	48 ± 2	44 ± 1	92
	1230	24.5	51.6	1.7	49 ± 2	46 ± 2	94
	1540	24.4	48.5	2.1	56 ± 2	52 ± 2	96
	1870	24.7	44.8	2.6	55 ± 3	52 ± 2	95
	2160	24.9	42.7	3.0	57 ± 2	54 ± 2	95
Channel with B45R30	950	25.2	59.6	1.3	49 ± 2	45 ± 2	92
	1240	25.8	53.6	1.7	51 ± 2	48 ± 2	94
	1550	25.3	48.9	2.1	53 ± 2	51 ± 2	96
	1860	25.7	45.6	2.6	56 ± 3	51 ± 2	91
	2160	25.9	43.3	3.0	55 ± 2	53 ± 2	96
Channel with B60R20	930	23.6	58.3	1.3	48 ± 2	45 ± 1	94
	1260	24.1	51.4	1.8	51 ± 2	48 ± 2	94
	1540	24.9	48.7	2.1	55 ± 2	51 ± 2	93
	1860	24.6	44.8	2.6	55 ± 3	52 ± 2	95
	2160	24.5	42.1	3.0	56 ± 2	53 ± 2	95
Channel with B60R30	930	23.0	57.8	1.3	49 ± 2	45 ± 1	92
	1260	25.9	51.3	1.8	48 ± 2	45 ± 2	94
	1540	24.8	48.3	2.1	54 ± 2	50 ± 2	93
	1860	26.6	45.6	2.6	53 ± 2	49 ± 2	92
	2170	22.9	39.9	3.0	55 ± 2	51 ± 2	93
Channel with B90R10	930	25.2	57.7	1.3	46 ± 2	42 ± 2	91
	1550	24.9	47.1	2.1	51 ± 2	48 ± 2	94
	2160	25.7	42.6	3.0	55 ± 2	51 ± 2	93
Channel with B90R20	920	25.2	58.3	1.3	46 ± 2	43 ± 1	93
	1220	27.3	53.5	1.7	46 ± 2	45 ± 2	98
	1540	26.3	48.9	2.1	50 ± 2	48 ± 2	96
	1860	26.4	45.6	2.6	53 ± 2	50 ± 2	94
	2170	25.8	43.5	3.0	56 ± 2	53 ± 2	95
Channel with B90R30	920	25.4	59.1	1.3	47 ± 2	43 ± 1	91
	1250	24.9	50.1	1.7	48 ± 2	44 ± 2	92
	1540	26.2	49.4	2.1	53 ± 2	50 ± 2	94
	1870	27.9	46.7	2.6	53 ± 2	49 ± 2	92
	2160	28.0	44.8	3.0	54 ± 2	51 ± 2	94

A.2. Nusselt number and friction factor for inserts

The test conditions for each test and measured Nu and f_D are tabulated in Table A-2.

Table A-2 Experimental data for inserts.

	Re	T_{air} [°C]		$T_{wall,surf}$ [°C]		$\dot{m}$ [g/s]	f_D	Nu
		Inlet	Outlet	inlet	outlet			
Channel with B30R20	930	24.2	59.8	36.7	62.3	1.3	0.516±0.065	16.9±1.0
	1250	26.5	54.9	37.6	57.3	1.7	0.452±0.041	20.2±1.3
	1550	24.5	49.3	34.1	51.8	2.1	0.376±0.033	23.7±1.5
	1870	26.5	47.7	35.5	50.0	2.6	0.357±0.031	26.3±1.8
	2160	24.9	42.3	32.8	44.5	3.0	0.310±0.027	28.5±2.0
Channel with B30R30	930	23.5	56.5	35.7	59.5	1.3	0.490±0.063	15.0±0.8
	1230	25.9	53.7	35.9	56.7	1.7	0.427±0.040	18.9±1.0
	1540	24.4	48.5	32.7	49.1	2.1	0.347±0.031	21.2±1.3
	1840	24.7	44.8	34.4	49.6	2.5	0.336±0.030	24.6±1.6
	2160	24.9	42.7	32.7	44.8	3.0	0.294±0.025	26.6±1.8
Channel with B45R20	930	23.9	57.8	37.0	60.5	1.3	0.462±0.060	15.4±0.9
	1230	24.5	51.6	35.6	54.3	1.7	0.390±0.038	18.0±1.1
	1540	24.4	48.5	34.6	51.3	2.1	0.320±0.030	21.4±1.3
	1870	24.7	44.8	33.7	47.5	2.6	0.303±0.027	23.7±1.5
	2160	24.9	42.7	33.4	45.5	3.0	0.277±0.024	25.5±1.6
Channel with B45R30	950	25.2	59.6	38.5	62.6	1.3	0.410±0.055	14.8±0.8
	1240	25.8	53.6	37.1	56.4	1.7	0.370±0.044	18.2±1.1
	1550	25.3	48.9	35.3	51.8	2.1	0.307±0.035	20.6±1.2
	1860	25.7	45.6	34.6	48.4	2.6	0.278±0.031	23.0±1.4
	2160	25.9	43.3	34.2	46.2	3.0	0.262±0.029	25.0±1.6
Channel with B60R20	930	23.6	58.3	37.5	61.1	1.3	0.408±0.055	14.8±0.8
	1260	24.1	51.4	35.9	54.2	1.8	0.329±0.033	17.8±1.0
	1540	24.9	48.7	35.5	51.4	2.1	0.286±0.027	20.3±1.2
	1860	24.6	44.8	34.2	47.7	2.6	0.258±0.023	22.4±1.4
	2160	24.5	42.1	33.4	45.0	3.0	0.238±0.021	24.2±1.5
Channel with B60R30	930	23.0	57.8	36.6	60.7	1.3	0.368±0.052	14.7±0.8
	1260	25.9	51.3	36.6	54.0	1.8	0.334±0.040	17.9±1.1
	1540	24.8	48.3	35.0	51.1	2.1	0.280±0.033	20.6±1.2
	1860	26.6	45.6	35.3	48.2	2.6	0.257±0.029	23.1±1.5
	2170	22.9	39.9	31.3	42.8	3.0	0.230±0.026	24.2±1.5

Channel with B90R10	930	25.2	57.7	37.5	61.4	1.3	0.431±0.057	13.6±0.7
	1550	24.9	47.1	34.0	50.3	2.1	0.325±0.030	19.8±1.2
	2160	25.7	42.6	33.6	46.1	3.0	0.284±0.026	22.7±1.4
Channel with B90R20	920	25.2	58.3	37.5	62.1	1.3	0.353±0.051	13.5±0.7
	1220	27.3	53.5	39.1	57.0	1.7	0.343±0.035	14.5±0.8
	1540	26.3	48.9	35.4	52.1	2.1	0.280±0.027	18.9±1.1
	1860	26.4	45.6	36.1	49.5	2.6	0.267±0.024	19.5±1.1
	2170	25.8	43.5	33.9	47.6	3.0	0.228±0.020	21.8±1.3
Channel with B90R30	920	25.4	59.1	39.1	62.4	1.3	0.343±0.050	13.3±0.7
	1250	24.9	50.1	36.2	53.9	1.7	0.315±0.039	14.9±0.8
	1540	26.2	49.4	36.7	52.8	2.1	0.263±0.031	18.5±1.0
	1870	27.9	26.2	37.3	50.6	2.6	0.239±0.027	19.8±1.2
	2160	28.0	28.0	36.9	48.4	3.0	0.225±0.025	21.6±1.3

A.3. Comparison of *Nu* for channels with inserts and hollow channel where both have a same pumping power

Table A-3 Equivalent Reynolds number and Nusselt number within the hollow channel.

	Re in channel with inserts	*Nu* in channel with inserts	Pumping power [W]	$Re_{eq,\ hollow}$	$\overline{Nu}_{eq,hollow}$	$\frac{Nu}{\overline{Nu}_{eq,hollow}}$
Channel with B30R20	930	16.9±1.0	0.04	2071	9.3	1.8
	1250	20.2±1.3	0.08	3047	11.8	1.7
	1550	23.7±1.5	0.13	3802	14.8	1.6
	1870	26.3±1.8	0.21	4916	18.8	1.4
	2160	28.5±2.0	0.29	5736	21.4	1.3
Channel with B30R30	930	15.0±0.8	0.04	2030	9.3	1.6
	1230	18.9±1.0	0.07	2890	11.1	1.7
	1540	21.2±1.3	0.12	3646	14.2	1.5
	1840	24.6±1.6	0.19	4666	17.9	1.4
	2160	26.6±1.8	0.27	5544	20.8	1.3
Channel with B45R20	930	15.4±0.9	0.03	1976	9.3	1.7
	1230	18.0±1.1	0.07	2743	10.5	1.7
	1540	21.4±1.3	0.11	3489	13.6	1.6
	1870	23.7±1.5	0.18	4524	17.4	1.4
	2160	25.5±1.6	0.25	5369	20.3	1.3
Channel with B45R30	950	14.8±0.8	0.03	1901	9.2	1.6
	1240	18.2±1.1	0.06	2696	10.3	1.8
	1550	20.6±1.2	0.10	3441	13.4	1.5
	1860	23.0±1.4	0.16	4307	16.6	1.4
	2160	25.0±1.6	0.24	5235	19.8	1.3
Channel with B60R20	930	14.8±0.8	0.03	1837	9.2	1.6
	1260	17.8±1.0	0.06	2629	10.0	1.8
	1540	20.3±1.2	0.10	3296	12.8	1.6
	1860	22.4±1.4	0.15	4147	16.1	1.4
	2160	24.2±1.5	0.22	4996	19.0	1.3
Channel with B60R30	930	14.7±0.8	0.03	1742	9.1	1.6
	1260	17.9±1.1	0.06	2645	10.1	1.8
	1540	20.6±1.2	0.09	3263	12.7	1.6
	1860	23.1±1.5	0.15	4158	16.1	1.4
	2170	24.2±1.5	0.21	4933	18.8	1.3

Channel with B90R10	930	13.6±0.7	0.03	1909	9.2	1.5
	1550	19.8±1.2	0.11	3538	13.8	1.7
	2160	22.7±1.4	0.26	5466	20.6	1.3
Channel with B90R20	920	13.5±0.7	0.03	1702	9.1	1.5
	1220	14.5±0.8	0.06	2542	9.6	1.8
	1540	18.9±1.1	0.09	3248	12.6	1.7
	1860	19.5±1.1	0.16	4237	16.4	1.4
	2170	21.8±1.3	0.21	4917	18.8	1.3
Channel with B90R30	920	13.3±0.7	0.02	1665	9.1	1.5
	1250	14.9±0.8	0.06	2522	9.5	1.6
	1540	18.5±1.0	0.09	3172	12.3	1.5
	1870	19.8±1.2	0.14	4031	15.7	1.3
	2160	21.6±1.3	0.21	4856	18.6	1.2

A.4. Comparison between predicted and experimental value of *Nu*

Table A- 4 Comparison between empirical and experimental average Nusselt number for the inserts.

	Re	$Nu_{empirical}$	Nu_{exp}	$\frac{\lvert Nu_{\text{empirical}} - Nu_{\text{exp}} \rvert}{Nu_{\text{exp}}}$
B30R20	930	16.3±0.8	16.9±1.0	0.03
	1250	19.5±0.1.1	20.2±1.3	0.04
	1550	22.4±0.1.3	23.7±1.5	0.06
	1870	25.6±0.1.5	26.3±1.8	0.03
	2160	28.5±0.1.8	28.5±2.0	0.00
B30R30	930	16.3±0.8	15.0±0.8	0.09
	1230	19.3±1.0	18.9±1.0	0.02
	1540	22.4±1.3	21.2±1.3	0.05
	1840	25.3±1.5	24.6±1.6	0.03
	2160	28.4±1.7	26.6±1.8	0.07
B45R20	930	15.3±0.8	15.4±0.9	0.01
	1230	17.8±0.9	18.0±1.1	0.01
	1540	20.5±1.2	21.4±1.3	0.04
	1870	23.4±1.4	23.7±1.5	0.01
	2160	25.9±1.6	25.5±1.6	0.01
B45R30	950	15.3±0.8	14.8±0.8	0.04
	1240	17.9±0.9	18.2±1.1	0.02
	1550	20.6±1.2	20.6±1.2	0.00
	1860	23.3±1.4	23.0±1.4	0.02
	2160	25.9±1.6	25.0±1.6	0.04
B60R20	930	14.5±0.7	14.8±0.8	0.04
	1260	17.2±0.9	17.8±1.0	0.03
	1540	19.4±1.1	20.3±1.2	0.01
	1860	21.9±1.3	22.4±1.4	0.03
	2160	24.3±1.5	24.2±1.5	0.06
B60R30	930	14.5±0.7	14.7±0.8	0.02
	1260	17.2±0.9	17.9±1.1	0.04
	1540	19.4±1.1	20.6±1.2	0.06
	1860	22.0±1.3	23.1±1.5	0.05

	2170	24.4±1.5	24.2±1.5	0.01
B90R10	930	13.7±0.6	13.6±0.7	0.00
	1550	18.0±0.9	19.8±1.2	0.09
	2160	22.3±1.2	22.7±1.4	0.02
B90R20	920	13.6±0.6	13.5±0.7	0.01
	1220	15.7±0.7	14.5±0.8	0.08
	1540	17.9±0.9	18.9±1.1	0.05
	1860	20.2±1.1	19.5±1.1	0.03
	2170	22.4±1.2	21.8±1.3	0.02
B90R30	920	13.6±0.6	13.3±0.7	0.02
	1250	15.9±0.8	14.9±0.8	0.06
	1540	18.0±0.9	18.5±1.0	0.03
	1870	20.2±1.1	19.8±1.2	0.02
	2160	22.3±1.2	21.6±1.3	0.03

A.5. Comparison between predicted and experimental value of f_D

Table A- 5 Comparison between empirical and experimental f_D for the inserts.

	Re	$(f_D)_{empirical}$	$(f_D)_{exp}$	$\frac{\left\|(f_D)_{empirical}-(f_D)_{exp}\right\|}{(f_D)_{exp}}$
B30R20	930	0.55±0.03	0.516±0.065	0.06
	1250	0.41±0.02	0.452±0.041	0.09
	1550	0.35±0.01	0.376±0.033	0.06
	1870	0.31±0.01	0.357±0.031	0.12
	2160	0.29±0.01	0.310±0.027	0.06
B30R30	930	0.54±0.03	0.490±0.063	0.11
	1230	0.42±0.02	0.427±0.040	0.03
	1540	0.35±0.01	0.347±0.031	0.02
	1840	0.32±0.01	0.336±0.030	0.06
	2160	0.29±0.01	0.294±0.025	0.00
B45R20	930	0.43±0.02	0.462±0.060	0.06
	1230	0.35±0.02	0.390±0.038	0.10
	1540	0.31±0.01	0.320±0.030	0.07
	1870	0.28±0.01	0.303±0.027	0.07
	2160	0.27±0.01	0.277±0.024	0.04
B45R30	950	0.43±0.02	0.410±0.055	0.05
	1240	0.35±0.02	0.370±0.044	0.05
	1550	0.31±0.01	0.307±0.035	0.00
	1860	0.28±0.01	0.278±0.031	0.01
	2160	0.27±0.01	0.262±0.029	0.01
B60R20	930	0.39±0.02	0.408±0.055	0.04
	1260	0.32±0.01	0.329±0.033	0.03
	1540	0.29±0.01	0.286±0.027	0.01
	1860	0.27±0.01	0.258±0.023	0.03
	2160	0.25±0.01	0.238±0.021	0.06
B60R30	930	0.39±0.02	0.368±0.052	0.06
	1260	0.32±0.01	0.334±0.040	0.05
	1540	0.29±0.01	0.280±0.033	0.03
	1860	0.27±0.01	0.257±0.029	0.04
	2170	0.25±0.01	0.230±0.026	0.10

B90R10	930	0.35±0.02	0.431±0.057	0.20
	1550	0.27±0.01	0.325±0.030	0.17
	2160	0.24±0.01	0.284±0.026	0.15
B90R20	920	0.35±0.02	0.353±0.051	0.01
	1220	0.30±0.01	0.343±0.035	0.13
	1540	0.27±0.01	0.280±0.027	0.04
	1860	0.25±0.01	0.267±0.024	0.06
	2170	0.24±0.01	0.228±0.020	0.06
B90R30	920	0.35±0.02	0.343±0.050	0.02
	1250	0.29±0.01	0.315±0.039	0.06
	1540	0.27±0.01	0.263±0.031	0.02
	1870	0.25±0.01	0.239±0.027	0.05
	2160	0.24±0.01	0.225±0.025	0.07

APPENDIX B

PARAMETER ESTIMATION CODE

This section provides the code for maximum Likelihood method which is used to develop empirical correlations for *Nu* and f_D. Mathematica, a computational software program, is used for this purpose.

B.1. Friction factor correlation

```
ClearAll["Global`*"];
 (*clears all values,definitions,attributes,messages,and defaults*)
f[x_, β_] := β[[1]] * Exp[(β[[2]] + x[[1]] * β[[3]])/(x[[1]] * x[[2]])];
(*model proposed to express the dependent variable as a function of
 the independent variables. β[[i]]s are model's parameters and x[[i]]s
 are the independent variables*)

df[x_, β_] :=
   {Exp[(β[[2]]/x[[1]] + β[[3]])/x[[2]]], β[[1]]/(x[[1]] * x[[2]]) * Exp[(β[[2]] + x[[1]] * β[[3]])/(x[[1]] * x[[2]])], β[[1]]/x[[2]] * Exp[(β[[2]] + x[[1]] * β[[3]])/(x[[1]] * x[[2]])]};
(*derivative of the proposed model WRT the model's parameters*)

t = {{ 30, 927}, {30, 1254}, {30, 1546}, {30, 1865}, {30, 2168},
    { 30, 931}, {30, 1228}, {30, 1543}, {30, 1838}, {30, 2158},
    { 45, 933}, {45, 1254}, {45, 1540}, {45, 1865}, {45, 2155},
    { 45, 946}, {45, 1235}, {45, 1548}, {45, 1857}, {45, 2157},
    {60, 926}, {60, 1263}, {60, 1539}, {60, 1858}, {60, 2158},
    {60, 925}, {60, 1263}, {60, 1540}, {60, 1863}, {60, 2167},
    {90, 924}, {90, 1219}, {90, 1535}, {90, 1861}, {90, 2168},
    {90, 918}, {90, 1247}, {90, 1543}, {90, 1868}, {90, 2158}};
(*values of the independent variables at each data point,
calculations to be performed numerically*)

y = {0.51636, 0.45224, 0.37573, 0.35739, 0.3098,
    0.48957, 0.42716, 0.34732, 0.33632, 0.29362,
    0.46233, 0.39032, 0.32009, 0.30298, 0.27672,
    0.409660926, 0.370488398, 0.306605375, 0.278078272, 0.262129834,
    0.40824171, 0.329119528, 0.286128146, 0.257522119, 0.238438714,
    0.368428095, 0.333561444, 0.279767616, 0.256835812, 0.229682029,
    0.352585392, 0.342643464, 0.279832085, 0.26735104, 0.227599676,
    0.343483725, 0.315025148, 0.263240406, 0.23925332, 0.225142841};
(*values of dependent variable at each data point,
calculations to be performed numerically*)



μβ = {1, 1, 1}; (*initial guess for the model's parameters*)
```

```
n = Length[y]; (*number of data points*)
p = Length[μβ]; (*number of model's parameters*)
er = .04;
(*standard deviation in measurements, expressed as fraction of
 the value of the dependent variable at each data point*)
w = er^-2 DiagonalMatrix[y^-2];
(*weight of each data point,
proportional to the inverse of the standard deviation squared *)
re = 10^-10; (*relative error between two the result of two consequent
 iterations used as the convergence criteria*)
βi= μβ; (*initial guess for β*)
Do[a=1;

(*main loop for parmater estimation based on Maximum Li elihood
using  ox- anemasu Method *)
xi =Table[df[t[[i]],βi],{i,1,n}];
(*creates xi which is the function df calculated at t and βi*)
ηi=Table[f[t[[i]],βi],{i,1,n}];
(*creates ηi which is the function f calculated at t and βi*)
pi= nverse[ et recision[xi^T.w.xi,20]];
(* ets the arithmetic precision to prevent errors due to an ill-conditioned matrix*)
fi=xi^T.w.(y-ηi); (*used in calculating the next guess for β*)
 or[l=1,l≤7,l++, (*loop to prevent oscillation and non-convergence*)
βip1 = βi+a pi.fi; (*guess i+1 for β*)
ηip1=Table[f[t[[i]],βip1],{i,1,n}];
(*next guess for η which is the function f calculated at t and βip1*)
si=(y-ηi).w.(y-ηi); (*cost function of the ML method at ηi*)
s0=si;
sa=(y-ηip1).w.(y-ηip1); (*cost function of the ML method at ηip1*)
 f[sa>s0,a=a/2, rea []]; (*condition to end the loop*)
];
βip1=βi+a pi.fi;  (*guess i+1 for β*)
ηip1=ηip1=Table[f[t[[i]],βip1],{i,1,n}];
(*next guess for η which is the function f calculated at t and βip1*)
sip1=(y-ηip1).w.(y-ηip1); (*cost function of the ML method at ηip1*)
βi=βip1;
(*changes the current guess for β to βip1, can be
used as the initial guess in the next iteration*)
ηi=ηip1;
(*changes the current value for η to ηip1, to be
used for calculation of R-squared*)
 f[Abs[(si-sip1)]<re,
(*convergence criteria to end the main loop*)
```

```
 rint[""]; (*cosmetic output*)
 rint["!!! rogram Ended  uccessfuly!!!"];
(*printed if the loop converges successfully*)
 rint[" umber of iterations: ", ];
(*printed number of itereations of the main loop*)
 rea []
(*ends the main loop*)
];
,{ ,1,50}];
(*maximum number of iterations for the main loop, used to prevent an infinite loop*)
 rint["β: ",βi//Matrix orm];
(*prints β vector, which is the estimation for model's parameters*)
cov= [pi,4];
(*the covariance matrix for the estimated parameters*)
σ=(Diagonal[cov^.5]); (*standard deviation of the estimated parameters*)
 rint["σ%: ",Abs[σ/βi]*100//Matrix orm];
(*prints the standard deviation of the estimated parameters in percentage*)
 rint["Cov: ",cov//Matrix orm];
(*prints the covariance matrix for the estimated parameters*)
 rint[" = ",si];  (*prints the cost function for the ML method*)
 rint["R-squared: ",(1-((y-ηi).(y-ηi))/ orm[y]^2)];  (*prints the R- qaured*)
```

```
!!!Program Ended Successfuly!!!

Number of iterations: 9

β: {0.183653, 19004.5, 386.078}

σ%: {2.10272, 5.43379, 9.43881}

Cov: {{0.00001491, 0.1824, -0.1084}, {0.1824, 1.066*10^6, -2.361*10^4}, {-0.1084, -2.361*10^4, 1328.}}

S= 87.4625

R-squared: 0.995986
```

B.2. Nusselt number correlation

```
ClearAll["Global`*"];
(*clears all values,definitions,attributes,messages,and defaults*)
```

$$f[x\_, \beta\_] := \beta[[1]] * \frac{1}{x[[1]]^{\beta[[2]]}} * x[[2]] + \beta[[3]];$$

```
(*model proposed to express the dependent variable as a function
 of the independent variables. β[[i]]s are
 model's parameters and x[[i]]s are the independent variables*)
```

$$df[x\_, \beta\_] := \left\{\frac{1}{x[[1]]^{\beta[[2]]}} * x[[2]], -\beta[[1]] * x[[1]]^{-\beta[[2]]} * \text{Log}[x[[1]]] * x[[2]], 1\right\};$$

```
(*derivative of the proposed model WRT the model's parameters*)

t = N[{{ 48, 927}, {48, 1254}, {48, 1546}, {48, 1865}, {48, 2168},
     { 48, 931}, {48, 1228}, {48, 1543}, {48, 1838}, {48, 2158},
     { 28.125, 933}, {28.125, 1254},
     {28.125, 1540}, {28.125, 1865}, {28.125, 2155},
     { 28.125, 946}, {28.125, 1235}, {28.125, 1548}, {28.125, 1857}, {28.125, 2157},
     {37.5, 926}, {37.5, 1263}, {37.5, 1539}, {37.5, 1858}, {37.5, 2158},
     {37.5, 925}, {37.5, 1263}, {37.5, 1540}, {37.5, 1863}, {37.5, 2167},
     {56.25, 924}, {56.25, 1219}, {56.25, 1535}, {56.25, 1861}, {56.25, 2168},
     {56.25, 918}, {56.25, 1247}, {56.25, 1543}, {56.25, 1868}, {56.25, 2158}}];
(*values of the independent variables at each data point, calculations to
 be performed numerically*)

y = N[{16.85, 20.23, 23.72, 26.34, 28.48, 15.01, 18.94, 21.19, 24.61, 26.62, 15.41,
     18.01, 21.39, 23.69, 25.51,
     14.82, 18.24, 20.57, 22.95, 25.01, 14.75, 17.82, 20.32, 22.44, 24.16,
     14.73, 17.9, 20.59, 23.06, 24.21, 13.48, 14.48, 18.88, 19.53, 21.84, 13.32,
     14.92, 18.51, 19.78, 21.61}];
(*values of dependent variable at each data point, calculations to
 be performed numerically*)


μβ = {1, 0.2, 8.24}; (*initial guess for the model's parameters*)

n = Length[y]; (*number of data points*)
p = Length[μβ]; (*number of model's parameters*)
er = .03; (*standard deviation in measurement, expressed as fraction of the
 value of the dependent variable
  at each data point*)
w = er^-2 DiagonalMatrix[y^-2]; (*weight of each data point, proportional to the
 inverse of the standard deviation
  squared *)
re = 10^-10; (*relative error between two the result of two consequent
 iterations used as the convergence
 criteria*)
```

Out[15]= a

```
      βi= μβ; (*initial guess for β*)
      Do[a=1;
      (*main loop for parmater estimation based on Maximum Likelihood
      using Box-Kanemasu Method *)
      xi =Table[df[t[[i]],βi],{i,1,n}];
      (*creates xi which is the function df calculated at t and βi*)

ηi=Table[f[t[[i]],βi],{i,1,n}];
(*creates ηi which is the function f calculated at t and βi*)
pi= nverse[ et recision[xi^T.w.xi,20]];
(* ets the arithmetic precision to prevent errors due to an
ill-conditioned matrix*)
fi=xi^T.w.(y-ηi);
(*used in calculating the next guess for β*)
 or[l=1,l≤7,l++,
(*loop to prevent oscillation and non-convergence*)
βip1 = βi+a pi.fi; (*guess i+1 for β*)
ηip1=Table[f[t[[i]],βip1],{i,1,n}];
(*next guess for η which is the function f calculated at t and βip1*)
si=(y-ηi).w.(y-ηi);
(*cost function of the ML method at ηi*)
s0=si;
sa=(y-ηip1).w.(y-ηip1);
(*cost function of the ML method at ηip1*)
 f[sa>s0,a=a/2,Break[]];
(*condition to end the loop*)
];
βip1=βi+a pi.fi;  (*guess i+1 for β*)
ηip1=ηip1=Table[f[t[[i]],βip1],{i,1,n}];
(*next guess for η which is the function f calculated at t and βip1*)
sip1=(y-ηip1).w.(y-ηip1);
(*cost function of the ML method at ηip1*)
βi=βip1; (*changes the current guess for β to βip1, can be
used as the initial guess in the next iteration*)
ηi=ηip1; (*changes the current value for η to ηip1, to be
used for calculation of R-squared*)
 f[Abs[(si-sip1)]<re, (*convergence criteria to end the main loop*)
 rint[""]; (*cosmetic output*)
 rint["!!! rogram  nded  uccessfuly!!!"];
(*printed if the loop converges successfully*)
 rint["Number of iterations: ", ];
(*printed number of itereations of the main loop*)
Break[] (*ends the main loop*)
];
```

```
,{ ,1,50}];
(*maximum number of iterations for the main loop, used to
prevent an infinite loop*)
 rint["β: ",βi//Matrix orm];
(*prints β vector, which is the estimation for model's parameters*)
cov=N[pi,4];
(*the covariance matrix for the estimated parameters*)
σ=(Diagonal[cov^.5]);
(*standard deviation of the estimated parameters*)
 rint["σ%: ",Abs[σ/βi]*100//Matrix orm];
(*prints the standard deviation of the estimated parameters
in percentage*)
 rint["Cov: ",cov//Matrix orm];
(*prints the covariance matrix for the estimated parameters*)
 rint[" = ",si];  (*prints the cost function for the ML method*)
 rint["R-squared: ",(1-((y-ηi).(y-ηi))/Norm[y]^2)];
(*prints the R- qaured*)
```

```
!!!Program Ended Successfuly!!!

Number of iterations: 6

β:  ( 0.0188701 )
    (  0.22547  )
    (  7.18711  )

σ%: ( 10.3525 )
    ( 12.6088 )
    ( 4.23961 )

Cov: (  3.816×10^-6   0.00005386  -0.00002167 )
     (  0.00005386    0.0008082    0.001711   )
     ( -0.00002167    0.001711     0.09285    )

S= 284.607

R-squared: 0.992677
```